EURASIAN JOURNAL OF CHEMISTRY

EURASIAN JOURNAL OF CHEMISTRY

2024

Volume 29 No. 1 (113)

Founded in 1996

Published 4 times a year

CONTENTS

PREFACE

ORGANIC CHEMISTRY

PHYSICAL AND ANALYTICAL CHEMISTRY

CHEMICAL TECHNOLOGY

RETRACTION NOTE

PREFACE

ABOUT NEW JOURNAL WEBSITE

Dear Colleagues,

We are pleased to present new website https://ejc.buketov.edu.kz/ of the *Eurasian Journal of Chemistry*. Since February 2024, submission of manuscripts and publication of articles in the *Eurasian Journal of Chemistry* takes place on the new website. The archive of journal issues before 2023 can be found on the old website https://chemistry-vestnik.ksu.kz/archive.

In 2023, our journal was rebranded and the journal title was changed from *Bulletin of the Karaganda University. Chemistry Series* on the *Eurasian Journal of Chemistry*, so our new website is located on a new domain, which corresponds to the new name of the journal.

Our new website is based on the OJS international publishing platform, which is used worldwide to automate the publishing process of Open Access scholarly journals. Before submitting, Authors should Login to the site or Register. The article is submitted through the Online Article Submission System. Authors are advised to read the Author Guidelines and adhere to the Ethical Standards before submitting, Authors can use Template for the Article and Template for the Supplementary Materials to prepare submission.

The Editorial Board of the Eurasian Journal of Chemistry hopes that the relocation to a new website will improve the journal's interaction with Authors, Reviewers, Readers and other interested parties, and will also contribute to the further journal development and promotion at the international level.

Editorial Board
Eurasian Journal of Chemistry

ORGANIC CHEMISTRY

Daria M. Turgunalieva[1, 2] iD, Ivan V. Kulakov[1, 2*] iD

[1]Center for Nature-Inspired Engineering, University of Tyumen, Tyumen, Russia;
[2]Higher School of Natural Science, University of Tyumen, Tyumen, Russia
(*Corresponding author's e-mail: i.v.kulakov@utmn.ru)

New Synthesis of 2-Aminopyrimidines
by Amination of Biginelli Reaction Products — Oxadiazocines

Previously, we synthesized methanobenzo[g][1,3,5]oxadiazocines and methanonaphtho[2,3-g][1,3,5]oxadiazocines via the Biginelli reaction using thiourea with acetoacetic ester or acetylacetone and salicylaldehyde or 2-hydroxy-1-naphthaldehyde under acidic catalysis and microwave irradiation. These compounds were then subjected to alkylation reaction with ethyl bromide in the presence of potassium carbonate in dimethylformamide. Under these mild reaction conditions, possible thione-thiol tautomerism of the oxadiazocines, as well as their structural analogs of cyclic thioureas, predominantly yielded in S-alkylation products with minor amounts of N-alkylation products. Further nucleophilic substitution reactions of S-ethyl-methanobenzo[g][1,3,5]oxadiazocines and S-ethyl-methanonaphtho[2,3-g][1,3,5]oxadiazocines revealed that alongside nucleophilic substitution by morpholine, elimination of phenol or naphthol occurred, followed by aromatization of the dihydropyrimidinone ring into an aromatic pyrimidine ring, resulting in the formation of 2-morpholinyl-substituted pyrimidines. Only a few examples and multi-step syntheses for obtaining such 2-amino-substituted pyrimidines are presented in the literature. Therefore, our newly discovered method for obtaining widely demanded derivatives of 2-aminopyrimidines is presented both relevant and promising.

Keywords: 2-aminopyrimidines, Biginelli reaction, oxadiazocines, methanonaphtho[2,3-g][1,3,5]oxadiazocine, methanobenzo[g][1,3,5]oxadiazocine, thione-thiol tautomerism, alkylation, morpholine, amination.

Introduction

Many natural and synthetic biomolecules exhibit their properties due to the presence of the pyrimidine ring. This ring is a crucial structural component in substances essential for maintaining vital functions in living organisms, including vitamins, coenzymes, and uric acid. The aminopyrimidine ring is a vital building block of the nucleotide bases found in DNA and RNA, which are crucial for the proper functioning of living cells. This emphasizes the immense importance of these compounds in nature. Derivatives of 2-amino-pyrimidines have a wide range of biological activities, making them a subject of great interest in organic synthesis for many years. Consequently, there is a significant interest in exploring innovative synthetic methods for their preparation [1–3].

Pyrimidine heterocycles find their main application in medicinal chemistry, primarily attributed to their potential as inhibitors of nucleic acid synthesis in infected cells or as carriers for delivering pharmacophoric groups to specific biological sites. Examples of such drugs include anticancer drugs such as Abemaciclib [4] and Imatinib [5]. 2-Aminopyrimidines are known for their diverse spectrum of activities, including anticancer [6], antibacterial [7–9], antifungal [10], antiviral [11], antitubercular and antimalarial [12], antidiabetic [13], anxiolytic [14] and anti-neurodegenerative [15] activities (Fig. 1).
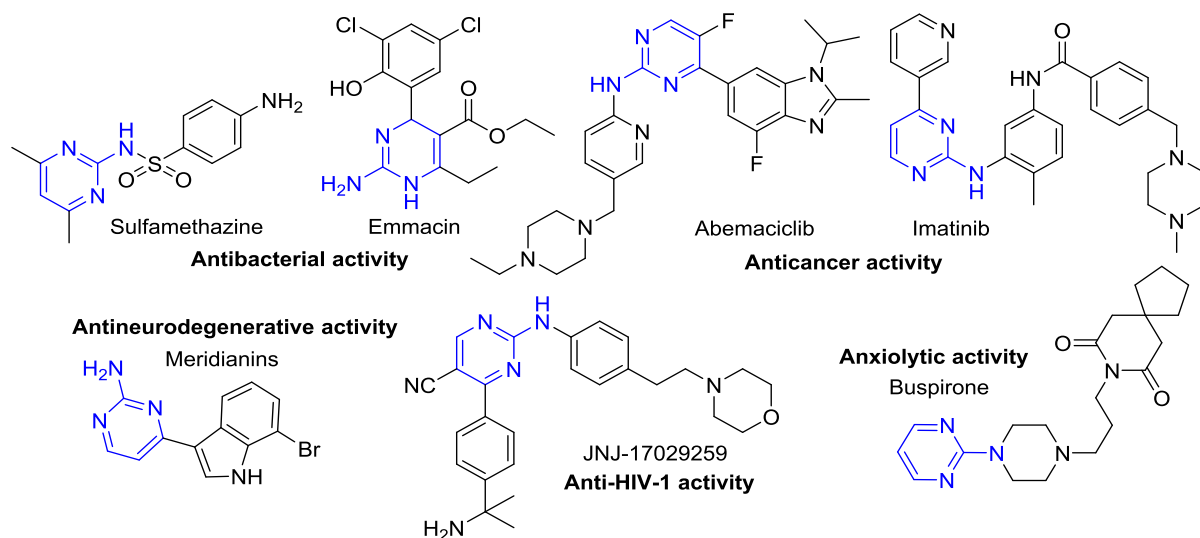
Figure 1. 2-Aminopyrimidine derivatives and their biological activity

Two primary methods are commonly used in the synthesis of substituted pyrimidines [16]. The first approach involves the condensation of fragments containing the desired substituents to construct the heterocyclic ring. The second approach involves introducing an amino group into the pyrimidine ring by substitution at position 2. However, the latter approach is less efficient and often results in low yields of the desired products, particularly in reactions with aryl amines where a large excess of the nucleophile is required. The pyrimidine ring can be synthesized via various condensation reactions involving different fragments in the overall process (Fig. 2).
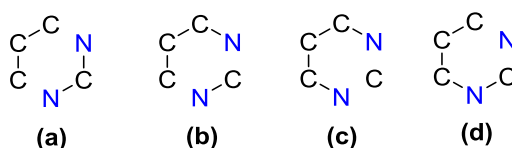
Figure 2. Variants of the condensation of the reagents to form the pyrimidine ring

Based on the literature data presented above, it is obvious to conclude that the 2-aminopyrimidine fragment is the most significant part responsible for the biological activity of its derivatives. This statement remains valid not only for substituted 2-aminopyrimidines but also for derivatives with condensed rings, including pteridines, pyridopyrimidines, imidazopyrimidines, purines, etc.

Experimental

Materials

^{1}H and ^{13}C NMR spectra were recorded on a Bruker DRX400 (400 and 100 MHz, respectively), Bruker AVANCE 500 (500 and 125 MHz, respectively) and Magritek spinsolve 80 carbon ultra (81 and 20 MHz, respectively) instruments. Residual solvent signals of DMSO-d_6 and CDCl$_3$ (2.49 and 39.9 ppm for ^{1}H and ^{13}C nuclei in DMSO-d_6; 7.25 and 77.0 ppm for ^{1}H and ^{13}C nuclei in CDCl$_3$) were used as the internal standards.

Chromato-mass spectrometric studies were carried out on a Trace GC Ultra chromatograph equipped with a DSQ II mass-selective detector in the electron ionization mode (70 eV) on a Thermo TR-5 MS quartz capillary column, 15 m long, 0.25 mm inner diameter, with a film thickness of the stationary phase of 0.25 μm. The splitless input mode was used. The carrier gas discharge was 20 ml/min. The carrier gas (helium) flow rate was 1 ml/min. Evaporator temperature 200 °C, transition chamber temperature 200 °C, ion source temperature 200 °C. The temperature of the column thermostat was changed according to the program: from 15 (5 min delay) to 220 °C at a rate of 20 °C per minute, to 290° at a rate of 15° per minute. The total analysis time was 30 min. The volume of the injected sample was 1 μl. The chromatograms were recorded in TIC mode. The range of mass scanning was 30–450 amu.

The progress of the reaction and the purity of the products were monitored by TLC on Sorbfil plates and visualized using iodine vapor or UV light.

The physicochemical and spectral characteristics of compounds **1a-c** were in agreement with literature data [22, 23].

Synthesis and Spectral Analysis of Synthesized Compounds

Ethyl 5-methyl-3-thioxo-2,3,4,5-tetrahydro-1*H*-1,5-methanonaphtho[1,2-*g*][1,3,5]oxadiazocine-13-carboxylate (1a) [23]. A mixture of 2-hydroxy-1-naphthaldehyde 1.72 g (10 mmol), thiourea 0.76 g (10 mmol) and acetoacetic ester 2.55 mL (20 mmol) in 15 mL of 2-propanol with 0.3 mL of trifluoroacetic acid catalyst was heated under MW irradiation for 5 seconds at 1 minute intervals. The total reaction time was 10 minutes. The precipitated solid was washed with water and 0.1 M NaOH solution. The solution was then decanted and the oil obtained was triturated with ice. The residue was purified by recrystallization from 2-propanol and chloroform. Yield: 1.300 g (38 %), white crystals, mp 290–291 °C.

^{1}H NMR spectrum (400 MHz, DMSO-d_6), δ, ppm: 1.27 (t, 3H, J = 7.1, OCH$_2$$\underline{CH_3}$); 1.86 (s, 3H, CH$_3$); 3.38 (br.s, 1H, H-13); 4.17-4.23 (m, 2H, OCH$_2$); 5.19 (dd, 1H, J = 5.5, 2.8, H-1); 7.08 (d, 1H, J = 8.7, H-7); 7.42 (t, 1H, J = 7.1, H-10), 7.58 (t, 1H, J = 7.1, H-11); 7.83 (d, 1H, J = 9.2, H-8); 7.87 (d, 1H, J = 7.8, H-9); 8.15 (d, 1H, J = 8.7, H-12); 9.13 (s, 1H, NH-4); 9.49 (d, 1H, J = 4.6, NH-2).

^{13}C NMR spectrum (100 MHz, DMSO), δ, ppm: 14.0 (CH$_2$CH$_3$); 23.1 (CH$_3$); 42.5 (C-1); 44.3(C-13); 60.8 (OCH$_2$); 81.4 (C-5); 115.2 (C-12b); 118.0 (C-7); 121.9 (C-12); 123.9 (C-10); 127.1 (C-11); 128.3 (C-9); 128.6 (C-8a); 130.1 (C-8); 130.6 (C-12a); 148.2 (C-6a); 167.9 (C=O); 176.5 (C=S).

Ethyl 2-methyl-4-thioxo-3,4,5,6-tetrahydro-2*H*-2,6-methanobenzo[*g*][1,3,5]oxadiazocine-11-carboxylate (1b) [22]. A mixture of 2-hydroxybenzaldehyde 1.04 mL (10 mmol), thiourea 0.76 g (10 mmol) and acetoacetic ester 2.55 mL (20 mmol) in 15 mL of 2-propanol with 0.3 mL of trifluoroacetic acid catalyst was refluxed at 60–70 °C for 12 hours. The precipitated yellow solid was washed with water and 0.1 M NaOH solution. The residue was purified by recrystallization from 2-propanol. Yield: 1.081 g (37 %), white crystals, mp 218–220 °C.

^{1}H NMR spectrum (400 MHz, DMSO-d_6), δ, ppm: 1.22 (t, 3H, J=7.1 Hz, OCH$_2$$\underline{CH_3}$); 1.77 (s, 3H, 2-CH$_3$); 4.14 (dk, 2H, J = 7.1, 3.2 Hz, O$\underline{CH_2}$CH$_3$); 4.58 (dd, 1H, J = 5.0, 2.7 Hz, 6-CH); 6.82 (d, 1H, J = 8.2 Hz, H-10); 6.93 (td, 1H, J = 7.6, J = 0.9, H-9); 7.17-7.23 (m, 2H, H-7,8); 9.12 (br. s, 2H, 2NH).

1-(2-Methyl-4-thioxo-3,4,5,6-tetrahydro-2*H*-2,6-methanobenzo[*g*][1,3,5]oxadiazocin-11-yl)ethan-1-one (1c) [22]. A mixture of 2-hydroxybenzaldehyde 1.04 mL (10 mmol), thiourea 0.76 g (10 mmol) and acetylacetone 2.05 mL (20 mmol) in 15 mL of 2-propanol with 0.3 mL of trifluoroacetic acid catalyst was refluxed at 60–70°C for 12 hours. The precipitated dark pink solid was washed with water and 0.1 M NaOH solution. The residue was purified by recrystallization from 2-propanol. Yield: 1.336 g (51 %), white crystals, mp 228–229 °C.

^{1}H NMR spectrum (400 MHz, DMSO-d_6), δ, ppm: 1.68 (s, 3H, 2-CH$_3$); 2.27 (s, 3H, COCH$_3$); 3.42 (br. s, 1H, 11-CH); 4.74 (dd, 1H, J = 5.2, J = 2.4, 6-CH); 6.82 (d, 1H, J = 8.0, H-10); 6.93 (td, 1H, J = 7.4, J = 1.0, H-9); 7.19–7.23 (m, 2H, H-7,8); 8.99 (d, 1H, J = 4.9, 5-NH); 9.04 (s, 1H, 3-NH).

Ethyl 4-(ethylthio)-2-methyl-5,6-dihydro-2*H*-2,6-methanonaphtho[2,3-*g*][1,3,5]oxadiazocine-13-carboxylate (3a). A mixture of 0.342 g (1 mmol) of **1a** with 0.276 g (2 mmol) of potassium carbonate in 3 mL of DMF was stirred at room temperature for 16 hours and 0.112 mL (1.5 mmol) of ethyl bromide was added dropwise. The mixture was then poured into water (100–200 ml) and a saturated aqueous salt solution (NaCl) was added. The residue was filtered, dried and recrystallized from 2-propanol. Yield: 0.333 g (90 %), white crystals, mp 139–142 °C.

^{1}H NMR spectrum (400 MHz, CDCl$_3$), δ ppm: 1.08 (t, 3H, J = 7.3 Hz, SCH$_2$$\underline{CH_3}$); 1.32 (t, 3H, J = 7.0 Hz, OCH$_2$$\underline{CH_3}$); 1.90 (s, 3H, CH$_3$); 2.78–2.91 (m, 2H, SCH$_2$); 3.04 (br.s, 1H, H-13); 4.16-4.30 (m, 2H, OCH$_2$); 5.44 (s, 1H, NH); 5.63 (d, 1H, J = 2.4 Hz, H-1); 7.03 (d, 1H, J = 9.2 Hz, H-7); 7.36 (t, 1H, J = 7.6 Hz, H-10); 7.54 (t, 1H, J = 7.6 Hz, H-11); 7.66 (d, 1H, J = 9.2 Hz, H-8); 7.75 (d, 1H, J = 7.9 Hz, H-9); 8.28 (1H, d, J = 8.5 Hz, H-12).

^{13}C NMR spectrum (101 MHz, CDCl$_3$), δ ppm: 14.1, 14.4, 23.8, 25.2, 43.6, 50.9, 61.0, 81.3, 117.1, 118.1, 122.8, 123.7, 126.8, 128.0, 129.1, 129.2, 131.9, 147.9, 155.9, 169.2.

Ethyl 4-(ethylthio)-2-methyl-5,6-dihydro-2*H*-2,6-methanobenzo[*g*][1,3,5]oxadiazocine-11-carboxylate (3b) obtained by analogy to **3a** from 0.292 g (1 mmol) of **1b**, 0.276 g (2 mmol) potassium carbonate and 0.112 mL (1.5 mmol) of ethyl bromide in DMF. Yield: 0.272 g (90 %), light grey crystals, mp 156–159 °C.

^{1}H NMR spectrum (400 MHz, DMSO-d$_6$), δ ppm: 1.09 (t, 3H, J = 7.3 Hz, SC<u>H$_2$CH$_3$</u>); 1.30 (t, 3H, J = 7.0 Hz, OCH$_2$<u>CH$_3$</u>); 1.91 (s, 3H, CH$_3$); 2.71–2.87 (m, 2H, SCH$_2$); 3.05 (s, 1H, H-11); 4.10-4.24 (m, 2H, OCH$_2$); 5.52 (s, 1H, NH); 5.59 (d, 1H, J = 2.4 Hz, H-1); 6.74 (1H, d, J = 7.8 Hz, H-10); 6.88 (t, 1H, J = 7.2 Hz, H-9); 7.10 (t, 1H, J = 7.1 Hz, H-8); 7.21 (d, 1H, J = 6.9 Hz, H-7).

1-(4-(Ethylthio)-2-methyl-5,6-dihydro-2*H*-2,6-methanobenzo[g][1,3,5]oxadiazocin-11-yl)ethan-1-one (3c) obtained by analogy to **3a** from 0.262 g (1 mmol) of **1c**, 0.276 g (2 mmol) potassium carbonate and 0.112 mL (1.5 mmol) of ethyl bromide in DMF. Yield: 0.261 g (90 %), white crystals, mp 166–169 °C.

^{1}H NMR spectrum (400 MHz, DMSO-d$_6$), δ ppm: 1.03 (t, 3H, J = 7.0 Hz, SC<u>H$_2$CH$_3$</u>); 1.63 (s, 3H, CH$_3$); 2.19 (s, 3H, COCH$_3$); 2.67-2.74 (m, 2H, SCH$_2$); 3.24 (s, 1H, H-11); 5.04 (d, 1H, J = 1.2 Hz, H-6); 6.77 (d, 1H, J = 7.9 Hz, H-10); 6.85 (t, 1H, J = 7.3 Hz, H-9); 7.12 (t, 1H, J = 7.0 Hz, H-8); 7.23 (d, 1H, J = 6.7 Hz, H-7); 8.14 (s, 1H, NH).

^{13}C NMR spectrum (101 MHz, DMSO-d$_6$), δ ppm: 14.8 (CH$_2$<u>CH$_3$</u>), 22.6 (SCH$_2$), 23.5 (CH$_3$), 28.8 (CO<u>CH$_3$</u>), 49.2 (C-11), 52.6 (C-6), 81.7 (C-2), 116.3 (C-10), 120.2 (C-8), 125.5 (C-6a), 128.4 (C-9), 129.3 (C-7), 150.9 (C-10a), 154.7 (C-4), 204.2 (C=O).

Ethyl 4-(2-ethoxyphenyl)-1,2,3,4-tetrahydro-6-methyl-2-thioxo-5-pyrimidinecarboxylate (4). A mixture of 0.292 g (1 mmol) of **1b** with 0.276 g (2 mmol) of potassium carbonate in 3 mL of DMF was stirred at room temperature and after 2 hours 0.112 mL (1.5 mmol) of ethyl bromide was added dropwise. Then the mixture was poured into water (100–200 ml) and a saturated aqueous salt solution (NaCl) was added. The residue was filtered, dried and recrystallized from 2-propanol. Yield: 0.224 g (70 %), light yellow powder, mp 147–150 °C.

^{1}H NMR spectrum (400 MHz, CDCl$_3$), δ ppm: 1.08 (t, 3H, J = 7.0 Hz, OCH$_2$<u>CH$_3$</u>); 1.46 (t, 3H, J = 7.0 Hz, OCH$_2$<u>CH$_3$</u>); 2.40 (s 3H, CH$_3$); 4.01-4.17 (m, 4H, 2 O<u>CH$_2$CH$_3$</u>); 5.73 (d, 1H, J = 2.4 Hz, H-6); 6.84–6.87 (m, 2H, H-3',4' Ar); 7.01 (dd, 1H, J = 7.6, 1.5 Hz, H-6' Ar); 7.23 (td, 1H, J = 7.6, 1.8 Hz, H-5' Ar); 7.29 (br. s, 1H, 3-NH); 8.10 (br.s, 1H, 1-NH). ^{13}C NMR spectrum (101 MHz, CDCl$_3$), δ ppm: 14.0, 14.9, 18.2, 51.3, 60.2, 63.6, 100.0, 111.5, 120.4, 127.2, 128.5, 129.5, 144.2, 156.2, 165.4, 174.5. MS (EI) *m/z* (I$_{rel}$, %): [M]$^+$ 320.03 (100), 291.03 (59), 275.07 (16), 247.02 (63), 244.97 (78), 198.99 (39), 170.99 (31), 152.89 (13).

Ethyl 4-methyl-2-morpholinopyrimidine-5-carboxylate (5a) [17]. Method A. A mixture of 0.370 g (1 mmol) **3a** with 0.870 g (10 mmol) of morpholine was heated for 8 hours. The solvent was then evaporated under vacuum and the residue was triturated with water. The precipitate was filtered, dried and recrystallized from 2-propanol. Yield: 0.045 g (18%), grey powder, mp 87–93 °C.

Method B. A mixture of 0.320 g (1 mmol) **3b** with 0.870 g (10 mmol) of morpholine was heated at 150 °C for 8 hours. The solvent was then evaporated under vacuum and the residue was triturated with water. The precipitate was filtered, dried and recrystallized from 2-propanol. Yield: 0.045 g (18 %), grey crystals, mp 90–93 °C.

^{1}H NMR spectrum (400 MHz, CDCl$_3$), δ ppm: 1.37 (t, 3H, J = 7.3 Hz, OCH$_2$<u>CH$_3$</u>); 2.65 (s, 3H, CH$_3$); 3.76 (br.t, 4H, J = 4.6 Hz, N(CH$_2$)$_2$); 3.92 (br. t, 4H, J = 4.9 Hz, O(CH$_2$)$_2$); 4.32 (q, 2H, J = 6.9 Hz, OCH$_2$); 8.82 (s, 1H, H-6). ^{13}C NMR spectrum (101 MHz, CDCl$_3$) δ ppm 14.3 (OCH$_2$<u>CH$_3$</u>), 25.0 (CH$_3$), 44.1 (N(CH$_2$)$_2$), 60.4 (OCH$_2$), 66.8 (O(CH$_2$)$_2$), 111.9, 160.8 (C-6), 161.1, 165.5, 170.2 (C=O). MS (EI) *m/z* (I$_{rel}$, %): [M]$^+$ 221.12 (76), 206.04 (34), 190.10 (100), 176.07 (37), 164.09 (44), 148.06 (40), 136.08 (46), 93.07 (13).

1-(4-Methyl-2-morpholinopyrimidin-5-yl)ethan-1-one (5c) obtained by analogy to **5a** from 0.290 g (1 mmol) of **3c** with 0.870 g (10 mmol) of morpholine. Yield: 0.033 g (15 %), yellowish brown oil.

MS (EI) *m/z* (I$_{rel}$, %): [M]$^+$ 251.10 (69), 236.05 (17), 220.06 (100), 206.04 (59), 194.06 (44), 177.97 (17), 166.05 (56), 148.01 (10), 138.00 (16), 93.04 (9).

Results and Discussion

It is well known that salicylaldehyde and other derivatives of 2-hydroxybenzaldehyde behave differently from simple aromatic aldehydes in many reactions due to the presence of two reactive centres, the electrophilic carbonyl carbon atom and the nucleophilic hydroxy group. The synthesis of 3-acetylcoumarin is just one example of how this attribute is frequently used in the creation of various heterocyclic compounds [18, 19].

The articles [20–23] revealed that when salicylaldehyde, urea (or thiourea) and specific dicarbonyl compounds were subjected to the Biginelli reaction in the presence of trifluoroacetic (or hydrochloric) acid

catalysts, the expected cyclization products of 4-aryl-3,4-dihydropyrimidin-2-ones (or 2-thiones) were not formed. Instead, the reaction resulted in the formation of derivatives of 3,4,5,6-tetrahydro-2H-2,6-methano[1,3,5]-benzo[g]oxadiazocines, chemical and biological properties of which were minimally studied. Therefore, this group of compounds is of great practical interest as they have the potential to be valuable candidates for extensive biological screening and can serve as starting materials for the synthesis of various biologically active molecules.

The starting materials for the Biginelli reaction, 2,6-methanobenzo- and 1,5-methanonaphtho-[1,3,5]oxadiazocines, were synthesized according to the Scheme 1:

R_1 = OEt (a,b), CH_3 (c); R_2 = (a), (b,c)
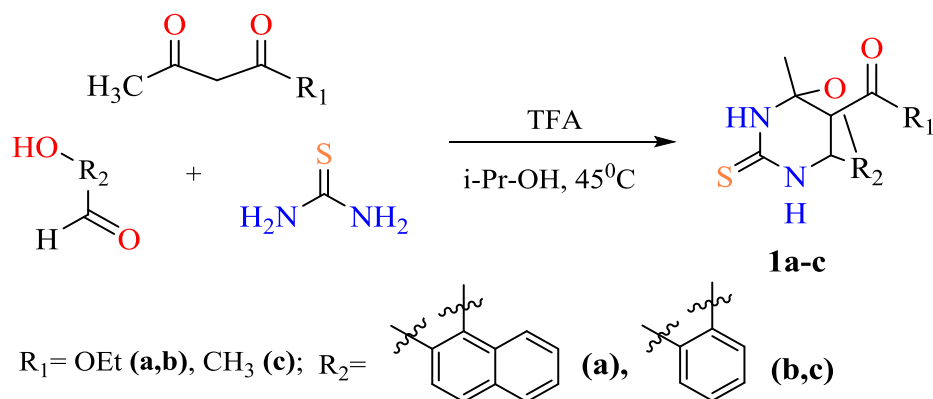
Scheme 1. Formation of 2,6- methanobenzo- and 1,5- methanonaphtho[1,3,5]oxadiazocine derivatives using One-pot Biginelli Reaction

The literature provides only a limited number of examples on alkylation reactions involving structural analogues of benzoxodiazocines — pyrimidinethiones. It has been reported [24] that alkylation of 3,4-dihydropyrimidine-2-thione-5-carboxylic acid derivatives in methanol leads to the formation of 2-alkylthio derivatives and subsequent alkylation yields in 2,3-dialkyl derivatives as the primary products. The authors [25] investigated the alkylation of 3,4-dihydropyrimidine(1H)-2-thione 2 not only under standard conditions (methanol in the presence of N-methylmorpholine), but also in the system of acetonitrile — concentrated solution of KOH, which is also used for the alkylation of 3,4-dihydropyrimidine(1H)-2-thiones [26] (Scheme 2).
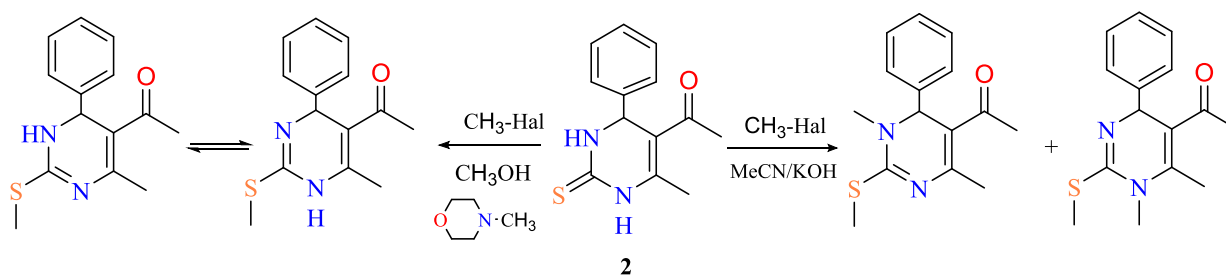
Scheme 2. Alkylation reaction of 2 in methanol with N-methylmorpholine

Upon treatment of alkyl halides in methanol with N-methylmorpholine, it undergoes S-alkylation reaction, while in the system of acetonitrile and aqueous KOH solution, a mixture of S(2), N(1)- and S(2), N(3)-alkylation products is formed. The composition of the tautomeric mixture of S-monoalkyl derivatives has been characterized, along with the regioselectivity of the dialkylation reaction.

Since the derivatives of diazocines 1a-c contain a cyclic thiourea fragment capable of thion-thiol tautomerism, the alkylation reaction was carried out with ethyl bromide in DMF in the presence of potassium carbonate. As expected, due to the stronger nucleophilic properties of the thiol group compared to the nitrogen atom, S-alkylation products of compounds 1a-c were obtained, as shown in Scheme 2, yielding in compounds 3a-c.
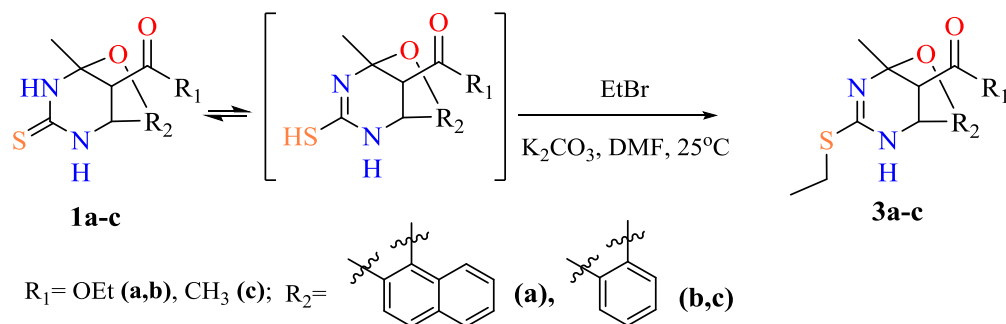
Scheme 3. Alkylation reaction of 2,6- methanobenzo- and 1,5- methanonaphtho[1,3,5]oxadiazocine derivatives

The structure of the alkylated derivatives **3a-c** was confirmed by ^{1}H and ^{13}C NMR spectroscopy. The presence of S-ethyl-2,6-methanobenzoxadiazocines **3c** was confirmed by the detection of specific spectroscopic signals, including a doublet of quartets of the methylene protons at 2.67-2.74 ppm, a triplet of methyl protons at 1.03 ppm originating from the S-ethyl group, and a singlet corresponding to the NH proton at 8.14 ppm. It is noteworthy that in the spectrum of the reaction mixture of compound **3c**, signals corresponding to the protons of the N-ethyl group were observed at 3.7–3.8 ppm. However, these signals exhibited significantly lower intensity compared to the S-isomer, indicating a lower degree of alkylation at the nitrogen atom. The approximate ratio of the alkylation products was estimated based on the signal intensities as 9:1 in favor of the S-ethyl derivative over the N-ethyl derivative.

Remarkable results were obtained in the alkylation of ethyl 2-methyl-4-thioxo-3,4,5,6-tetrahydro-2H-2,6-methanobenzo[g][1,3,5]oxadiazocine-11-carboxylate **1b** with ethyl bromide when it was added 2 hours after the dissolution of the starting compound **1b** in DMF. Upon treatment of the reaction mixture, a white crystalline compound was isolated from the predominant oily mass in a yield of about 10 %. This compound was easily purified by recrystallization. Analysis of the ^{1}H NMR spectrum revealed several important observations. Firstly, the methylene protons of both the S- and N-ethyl isomers, which were present in compound **3c** at 2.7 and 3.7 ppm respectively, were not observed. Secondly, the broad singlet corresponding to the H-11 proton in the original compound **1b** was not detected. Thirdly, the methyl group protons, previously observed as a singlet at 1.77 ppm in compound **1b**, experienced a significant shift to a weaker region at 2.40 ppm. Similarly, the H-6 proton transformed from a doublet of doublets at 4.48 ppm (due to interactions with the methylene and N-H protons) in compound **1b** to a clear doublet at 5.73 ppm. In addition, a quartet system in the range of 4.01–4.13 ppm, characteristic of the OSN2 groups, i.e., the methylene protons of the ethoxy moiety, was observed. Examination of the spectral data obtained indicated that the alkylation process in DMF resulted in the conversion of benzoxadiazocine **1b** to its structural isomer, the 3,4-dihydropyrimidine analogue **4**. This compound was subsequently alkylated with ethyl bromide to yield the corresponding ethyl 4-(2-ethoxyphenyl)-1,2,3,4-tetrahydro-6-methyl-2-thioxo-5-pyrimidinecarboxylate **4**.

The above conclusions regarding the proposed structure of compound **4** were fully supported by the analysis of the ^{13}C NMR spectrum. Previous studies cited in reference [27] have demonstrated comparable structural isomerizations of benzo[g]oxadiazocines in solutions of DMF or DMSO. These isomerizations were based on ^{1}H NMR spectra recorded in DMSO-d$_6$, which showed the structural transformation of the initial nitrobenzo[g]oxadiazocines into their respective hydroxyphenyl 3,4-dihydropyrimidinethiones.
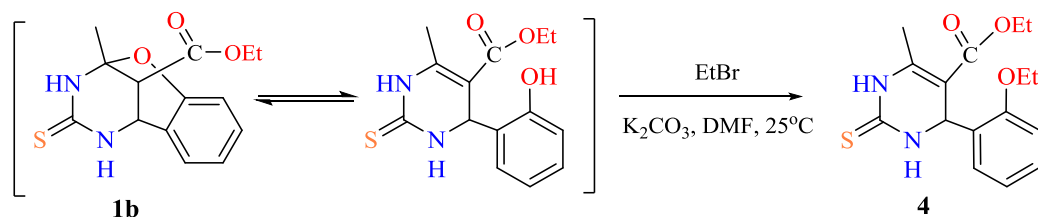
Scheme 4. Structural isomerization of benzoxadiazocine **1b** into 3,4-dihydropyrimidine analogue **4**

From the data obtained it can be concluded that even slight variations in the conditions of alkylation reaction for oxadiazocines, due to its potential thione-thiol tautomerism in the basic medium (DMF + K_2CO_3) and the opening of the oxazine ring, can lead to the formation of various products, including S-, N-, and O-alkylation.

In order to obtain 2-amino substituted benzo[g]oxadiazocine derivatives, the structural analogs of 2-aminopyrimidines, nucleophilic substitution reactions with S-ethyl-1,5-methanonaphthoxadiazocine **3a** and S-ethyl-1,3-benzoxadiazocines **3b** and **3c** in the excess of morpholine were carried out.

R₁= OEt **(a,b)**, CH₃ **(c)**; R₂=   **(a),**   **(b,c)**
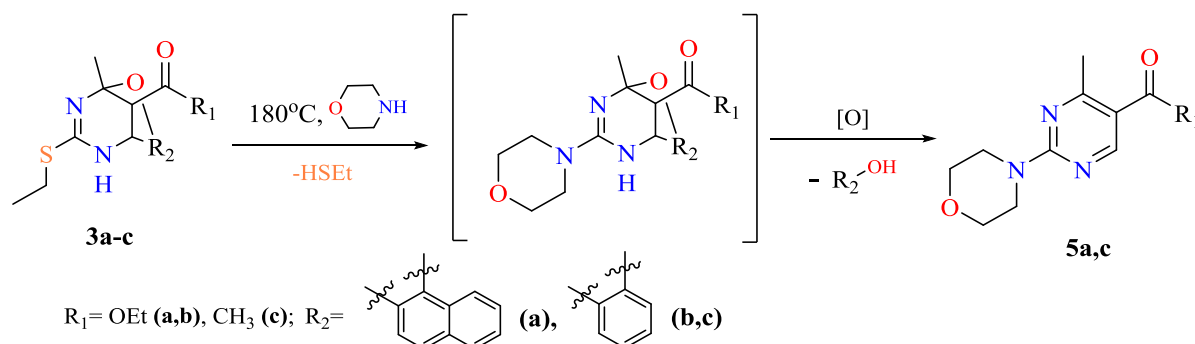
Scheme 5. Formation of 2-aminopyrimidine derivatives using amination reaction
with morpholine

NMR spectroscopic analysis of the reaction products indicated that, in addition to nucleophilic substitution by morpholine, elimination of the corresponding naphthol or phenol occurred. This elimination was followed by aromatization of the pyrimidine ring, ultimately leading to the formation of 2-morpholinyl-substituted pyrimidines **5a** and **5c**. The observed low reaction yields could be attributed to the partial tarring of the reaction mixture during the nucleophilic substitution reaction performed at an elevated temperature of 150 °C. It is worth noting that only a limited number of examples and rather complex, multi-step methods for obtaining similar 2-amino-substituted pyrimidines are reported in the literature [28, 29].

Conclusions

Thus, the study conducted using methanobenzo[g][1,3,5]oxadiazocine and methanonaphtho[2,3-g]-[1,3,5]oxadiazocine as model compounds has demonstrated their ability to undergo alkylation with ethyl bromide under relatively mild reaction conditions, resulting in the formation of S-ethyl derivatives. However, even minor modifications in the alkylation reaction conditions of oxadiazocines, such as the timing of ethyl bromide addition, the potential for thione-thiol tautomerism in the basic medium and the opening of the oxazine ring, lead to the formation of diverse products, including S-, N-, and O-alkylation.

These S-ethyl derivatives of oxadiazocines exhibit enhanced lipophilicity of the oxadiazocine core and possess good cell permeability, making them highly suitable for bioscreening applications. In addition, under the influence of a secondary amine — morpholine, the obtained S-ethyl derivatives of oxadiazocines undergo nucleophilic substitution of the ethylthiol group. During the substitution process, phenol (or naphthol) is eliminated and the dihydropyrimidine core undergoes oxidative aromatization. As a result, 2-amino-substituted pyrimidines are formed. This methodology offers a valuable approach to synthesizing a range of functional derivatives of 2-aminopyrimidines, which are typically challenging to access.

Funding

Author Information*

*The authors' names are presented in the following order: First Name, Middle Name and Last Name

Daria Maratovna Turgunalieva — Postgraduate Student, Higher School of Natural Science, University of Tyumen, 15a Perekopskaya St., 625003, Tyumen, Russia; *e-mail: d.m.turgunalieva@utmn.ru;* https://orcid.org/0009-0004-6299-9881

Ivan Vyacheslavovich Kulakov (*corresponding author*) — Doctor of Chemical Sciences, Associated Professor, Higher School of Natural Science, University of Tyumen, 15a Perekopskaya St., 625003, Tyumen, Russia; *i.v.kulakov@utmn.ru;* https://orcid.org/0000-0001-5772-2096

Author Contributions

The manuscript was written through contributions of all authors. All authors have given approval to the final version of the manuscript. CRediT: **Daria Maratovna Turgunalieva** investigation, formal analysis, data curation and writing — original draft preparation; **Ivan Vyacheslavovich Kulakov** conceptualization, methodology, validation, writing — review and editing and supervision.

Conflicts of Interest

The authors declare no conflict of interest.

References

1 Baskar, N., & A. Bunce, R. (2024). Recent Advances in Pyrimidine-Based Drugs. *Pharmaceuticals, 17*(1), 104. https://doi.org/10.3390/ph17010104

2 Harpel, Z., Chang, W-.J., Circelli, J., Chen, R., Chang, I., Rivera, J., Wu, S., & Wei, R. (2023). Effects of six pyrimidine analogs on the growth of Tetrahymena thermophila and their implications in pyrimi-dine metabolism. PLoS ONE, 18(9): e0284309. https://doi.org/10.1371/journal.pone.0284309

3 S. Laitonjam, W., & Moirangthem, N. (2023). Construction of Biologically Active Five- and Six-Membered Fused Ring Pyrimidine Derivatives from 1,3-Diarylthiobarbituric Acids (DTBA). IntechOpen. https://doi.org/10.5772/intechopen.108842

4 Abemaciclib (Brand Names: Verzenio, Approved). Available online: https://go.drugbank.com/drugs/DB12001 (accessed on 05.01.2024).

5 Imatinib (Brand Names: Gleevec, Glivec; Approved). Available online: https://go.drugbank.com/drugs/DB00619 (accessed on 05.01.2024).

6 Iqbal, S., Shaikh, N.N., Khan, K.M., Kiran, S., Naz, S., Ul-Haq, Z., Perveen, S., & Choudhary, M.I. (2022). Synthesis of 2-Aminopyrimidine Derivatives and Their Evaluation as β-Glucuronidase Inhibi-tors: In Vitro and In Silico Studies. *Molecules*, *27*, 7786. https://doi.org/10.3390/molecules27227786

7 Sulfamethazine (Approved, Vet approved). Available online: https://go.drugbank.com/drugs/DB01582 (accessed on 05.01.2024).

8 Wyatt, E.E., Galloway, W.R., Thomas, G.L., Welch, M., Loiseleur, O., Plowright, A.T., & Spring, D.R. (2008). Identification of an anti-MRSA dihydrofolate reductase inhibitor from a diversity-oriented synthesis. *Chem. Commun. (Camb.)*, *40*, 4962–4964. https://doi.org/10.1039/b812901k

9 Boyer, Z.W., Kessler, H., Brosman, H., Ruud, K.J., Falkowski, A.F., Viollet, C., Bourne, C.R., & O'Reilly, M.C. (2022). Synthesis and Characterization of Functionalized Amino Dihydropyrimidines Toward the Analysis of their Antibacterial Structure–Activity Relationships and Mechanism of Action. *ACS Omega, 42*(7), 37907–37916. https://doi.org/10.1021/acsomega.2c05071

10 Sulfadiazine (Approved, Vet approved). Available online: https://go.drugbank.com/drugs/DB00359 (accessed on 05.01.2024).

11 Makki, M.S.I., Abdel-Rahman R.M., & Khan K.A. (2014). Fluorine Substituted 1,2,4-Triazinones as Potential Anti-HIV-1 and CDK2 Inhibitors. *Journal of Chemistry, 12*(3), 430573:14. https://doi.org/10.1155/2014/430573

12 Yadav, R.R., Khan, S.I., Singh, S., Khan, I.A., Vishwakarma, R.A., & Bharate, S.B. (2015). Synthesis, antimalarial and antitubercular activities of meridianin derivatives. *Eur. J. Med. Chem., 98*, 160-169. https://doi.org/10.1016/j.ejmech.2015.05.020

13 Lobeglitazone (Experimental). Available online: https://go.drugbank.com/drugs/DB09198 (accessed on 05.01.2024).

14 Buspirone (Brand Names: Buspar, Approved). Available online: https://go.drugbank.com/drugs/DB00490 (accessed on 05.01.2024).

15 Llorach-Pares, L., Nonell-Canals, A., Sanchez-Martinez, M., & Avila, C. (2017) Computer-Aided Drug Design Applied to Marine Drug Discovery: Meridianins as Alzheimer's Disease Therapeutic Agents. *Mar. Drugs, 15*(12), 366. https://doi.org/10.3390/md15120366

16 Koroleva, E.V., Gusak, K.N., & Ignatovich, Zh.V. (2010). *Russ. Chem. Rev. 79*, 655. https://doi.org/10.1070/RC2010v079n08ABEH004116

17 Porcheddu, A., Giacomelli, G., De Luca, L., & Ruda, A.M. (2004). A "catch and release" strategy for the parallel synthesis of 2,4,5-trisubstituted pyrimidines. *J. Comb. Chem.*, *6*(1), 105-11. https://doi.org/10.1021/cc034024o

18 Kumar, N., Bhatnagar, A., & Dudhe, R. (2017). Synthesis of 3-(4,5-dihydro-1-phenyl-5-substituted phenyl-1H-pyrazol-3-yl)-2H-chromen -2-one derivatives and evaluation of their anticancer activity. *Arabian Journal of Chemistry*, *10*(2), S2443–S2452. https://doi.org/10.1016/j.arabjc.2013.09.008

19 Turgunalieva, D.M., Dilbaryan, D.S., Vasilchenko, A.S., Nurkenov, O.A., Fazylov, S.D., Karipova, G.Zh., Seilkhanov, T.M., & Kulakov, I.V. (2022) Synthesis and Antibacterial Activity of Hydrazones of Isonicotinic and Salicylic Acids Based on Acetyl

Derivatives of Coumarin and Benzo[g][1,3,5]Oxadiazocine. *Bulletin of the University of Karaganda – Chemistry*, *108*(4), 25–34. https://doi.org/10.31489/2022Ch4/4-22-2

20 Rajeev, R., & Shan, A.C. (2010) Formation of an oxygen-bridged pyrimidine ring system in the Bigi-nelli reaction. *ChemInform.*, *25*(52). https://doi.org/10.1002/chin.199452195

21 Kurbanova, M.M. (2010). Bicyclic compounds obtained by the Biginelli reaction. *Russ. J. Org. Chem., 46*, 599–601. https://doi.org/10.1134/S1070428010040305

22 Kulakov, I.V., Talipov, S.A., Shulgau, Z.T., & Seilkhanov, T.M. (2014). Synthesis, structure, and antiradical activity of new methano[1,3]thiazolo[2,3-*d*][1,3,5]benzoxadiazocine derivatives. *Chem. Heterocycl. Compd.*, 50*, 1477. https://doi.org/10.1007/s10593-014-1613-1

23 Kulakov, I.V., Ogurtsova, D.N., Seilkhanov, T.M., Gatilov, Y.V., & Fisyuk A.S. (2018). Synthesis, Structure, and Some Transformations of Novel 1,5-methanonaphtho[1,2-g][1,3,5]oxadiazocine Derivatives. *Journal of Heterocyclic Chemistry*, *55*(4), 923–928. https://doi.org/10.1002/jhet.3119.

24 Kappe, C.O. (1993). 100 Years of the Biginelli dihydropyrimidine synthesis. *Tetrahedron*, *49*(32), 6937–6963. https://doi.org/10.1016/S0040-4020(01)87971-0

25 Kolosov, M.A., Orlov, V.D., & Vasil'eva, Yu.M. (2006). Alkilirovanie proizvodnyh 5-Acetil-4-fenil-3,4-digidropirimidin-(1*H*)-2-tiona (The alkylation of 5-acetyl-4-phenyl-3,4-dihydropyrimidine-(1*H*)-2-thione derivatives). *Vestnik Kharkovskogo Natsionalnogo Universiteta. Khimiia*, *14*(37), 69–73. [in Russian]

26 Kolosov, M.A., & Orlov, V.D. (2005). 3-N-Acylation of 5-Ethoxycarbonyl-6-methyl-4-phenyl-3,4-dihydropyrimidin-2-one. *Chem Heterocycl Compd.,* 41, 260–261. https://doi.org/10.1007/s10593-005-0139-y

27 Sedova, V.F., Krivopalov, V.P., Gatilov, Yu. V., & Shkurko, O.P. (2014). Synthesis and intramolecular conversion of substi-tuted 2-methyl-11-nitro-5,6-dihydro-2H-2,6-methanobenzo[g][1,3,5]oxadiazocin-4(3*H*)-ones in different solvents. *Russian Chemical Bulletin*, *63*(6), 1378–1385. https://doi.org/10.1007/s11172-014-0606-7

28 Arya, V.P., David, J., Grewal, R.S., Marathe, S.B., & Patil, S.D. (1977). Psychoactive agents. Part VI. Synthesis and central nervous system effects of some 2-substituted 5-acetyl-4-methylpyrimidine derivatives. *Ind. Journal of Chem., 15B*(12), 1129–32. https://doi.org/10.1002/chin.197823222

29 Potapov, A.Y., Falaleev, A.V., & Shikhaliev, K.S. (2014) Preparation and synthetic scope of 3-(4-methyl-2-R-pyrimidin-5-yl)-3-oxopropionic esters. *Russ. Chem. Bull., 63*, 2198–2200. https://doi.org/10.1007/s11172-014-0720-6

Lyazat K. Salkeyeva[1] (iD), Leonid M. Pevzner[2] (iD), Pavel Vojtíšek[3] (iD), Yelena V. Minayeva[1*] (iD)

[1]*Department of Organic Chemistry and Polymers, Karaganda Buketov University, Karaganda, Kazakhstan;*
[2]*Department of Organic Chemistry, Saint-Petersburg State Technological Institute (Technical University), St. Petersburg, Russia;*
[3]*Department of Chemistry, Faculty of Science, Jan Evangelista Purkyně University in Ústí nad Labem,*
Ústí nad Labem, Czech Republic
(**Corresponding author's e-mail: yelenaminayeva@yandex.ru*)

On the Bromination of Diethyl 3,5-dimethyl-1H-pyrrole-2,4-dicarboxylate: the True Structure of the Halbig's Product

Pyrrole and its derivatives have attracted the attention of researchers as promising objects of practical importance in various areas of human life. Focusing on Knorr pyrrole as the most readily available pyrrole derivative, our objective was to obtain its bromo derivatives, containing an allyl bromine atom followed by phosphorylation reactions. The reaction involving bromination was carried out with 2 mol of N-bromosuccinimide per 1 mol of Knorr pyrrole **1** in carbon tetrachloride. This reaction was initiated with azobis(isobutyronitrile) and carried out at a boiling point. In acetic acid, the bromination reaction was carried out at a temperature of 38–45°C with a molar ratio of Knorr pyrrole to bromine of 1:4 and another reaction was carried out at 40–50°C with a molar ratio of Knorr pyrrole to bromine of 1:5. The bromination reaction was also performed in chloroform at 27–30°C in the presence of catalytic amounts of aluminum chloride. The same crystalline product was obtained in all cases. X-ray diffraction analysis revealed that the single crystal structure is diethyl 5-(dibromomethyl)-3-methyl-2-oxo-2,3-dihydro-1H-pyrrole-3,4-dicarboxylate **5** with two bromine atoms. This composition is identical to that of the Halbig product. It was found that the bromination of Knorr pyrrole **1** occurs stepwise with excess N-bromosuccinimide and bromine, resulting in the unsaturated lactam **5**, commonly known as Halbig's product. The true structure of product **5** was determined.

Keywords: Knorr pyrrole, α-methylpyrroles, bromination, the Halbig's product, bromo derivatives, Diethyl 3,5-dimethyl-1H-pyrrole-2,4-dicarboxylate, phosphorylation, reaction mechanism.

Introduction

Pyrrole and its derivatives remain a significant focus of researchers due to their role in providing new bioactive compounds. Some of them are crucial in various life processes [1]. Many pyrrole derivatives have shown diverse biological activities [2–12]. Knorr pyrrole, also known as diethyl 3,5-dimethyl-1H-pyrrole-2,4-dicarboxylate, is among the most commonly available pyrrole derivatives. There are additional studies regarding the phosphorylation of pyrrole and Knorr pyrrole [13]. The bromination reactions of derivatives of pyrrole followed by phosphorylation are unquestionably fascinating in the field of pyrrole chemistry [14].

The side-chain bromination of α-methylpyrroles has been well-known [15, 16]. At a pyrrole: bromine molar ratio of 1.06:1, the bromination reaction of Knorr pyrrole with molecular bromine in acetic acid, at 45 °C, produced 2-bromomethyl-4-methylpyrrole-3,5-dicarboxylic acid diethyl ester **2** in 42 % yield [15–20]. Likewise, using N-bromosuccinimide in carbon tetrachloride, in the presence of benzoyl peroxide at reflux, resulted in the same product in 47% yield [21]. The reaction scheme is displayed in Figure 1.
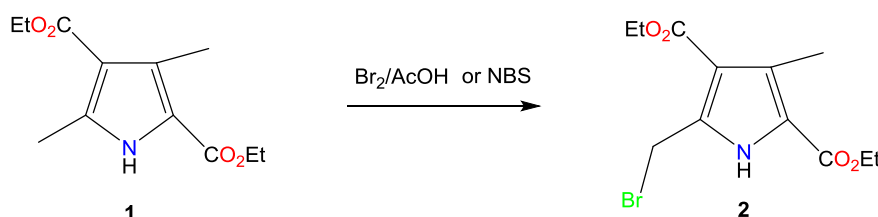
Figure 1. The formation of 2-bromomethyl-4-methylpyrrole-3,5-dicarboxylic acid diethyl ester **2**

Simultaneously, Halbig P. and Walach B. [17] observed the extraction of a crystalized substance upon cooling the reaction mixture of Knorr pyrrole with excess of bromine in acetic acid at 45–50 °C. After multiple washes with acetic acid, a compound with a melting point of 130-131 °C and a composition of $C_{12}H_{15}Br_2NO_5$ was obtained.

Treibs A. and Bader H. [21] obtained a compound with identical properties by brominating Knorr pyrrole in a blend of acetic acid and petroleum ether (1:1). Once the reaction mixture had been evaporated and the substance obtained had been recrystallized from dilute acetic acid and then from ethanol, a vibration band at 2.92 μ ($CHCl_3$) was detected in the compound's IR spectrum [21]. Following the reaction of α-unsubstituted pyrrole carboxylic acid esters with bromine, structure **3** was assigned to this substance [17], which was not disputed subsequently. The substance was referred to as the Halbig's product in the literature (Fig. 2).
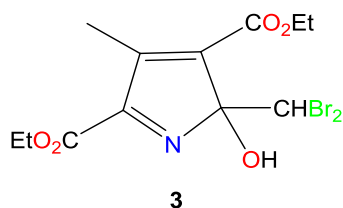
Figure 2. The structural formula of the Halbig's product [17, 21]

Later, Angelini et al. [19] conducted a ^{1}H NMR spectroscopic study on the crude bromination products. The study revealed the formation of α-dibromomethyl derivatives as byproducts. These byproducts were not observed in detectable amounts when the molar ratio of Br_2 to pyrrole was ≤0.5. However, they were the only reaction product formed when the molar ratio of Br_2 to pyrrole was ≥2 and the reaction was allowed to go to completion. α-Dibromomethylpyrroles were obtained as red oils that are sensitive to moisture. They were characterized by a singlet (1H) at approximately δ 6.5 ppm ($CHBr_2$) in the NMR spectrum. Additionally, they were converted into the corresponding aldehydes.

The aim of this study was to investigate the potential of obtaining 3,5-bis(bromomethyl) derivative **4** (Fig. 3) via the bromination of Knorr pyrrole as a starting compound for subsequent phosphorylation reactions.
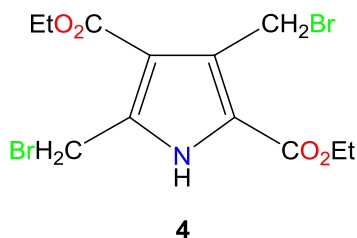
Figure 3. Structural formula of diethyl 3,5-bis(bromomethyl)-1H-pyrrole-2,4-dicarboxylate **4**

Experimental

Material and Instrumentation

All chemicals were of analytical grade and procured from Sigma-Aldrich suppliers without the need for further purification. Reactions underwent monitoring via thin layer chromatography (TLC) on F 254 silica gel coated plates from Merck. Bruker 400 and 600 MHz spectrometers were used to record the ^{1}H and ^{13}C NMR spectra in $CDCl_3$ along with TMS functioning as the internal standard. Mass spectra were taken using a Shimadzu mass spectrometer. IR spectra were taken with a Thermo Scientific Nicolet 6700 FTIR spectrometer (Madison, WI, USA). The melting point was determined using a Buchi Melting point M-560 instrument.

Diffraction experiments for **1** and **5** were performed on a Bruker D8 VENTURE Kappa Duo PHOTON100 by IμS micro-focus sealed tube either with MoKα (λ= 0.71073) radiation at a temperature of 120(2) K for **5,** or CuKα (λ = 1.54178) for **1** at a temperature of 150(2) K.

The structures were solved by direct methods [22] and refined by the full matrix F^2-based least squares method [23]. Hydrogen atoms on carbon were fixed into idealized positions (riding model) and assigned temperature factors either $H_{iso}(H) = 1.2\ U_{eq}$ (pivot atom) or $H_{iso}(H) = 1.5\ U_{eq}$ (pivot atom) for methyl moiety, the hydrogen atoms in –N-H moiety were found on difference Fourier maps and refined under rigid body assumption with assigned temperature factors $H_{iso}(H) = 1.2\ U_{eq}$ (pivot atom).

Synthesis Section

General procedure for bromination of 2,4-dimethyl-3,5-diethoxycarbonylpyrrole with NBS:

3.1 g (0.013 mol) of Knorr pyrrole, 5.02 g (0.028 mol) of NBS, 0.23 g of AIBN as an initiator and 70 ml of CCl_4 were added into a three-neck flask equipped with a mechanical stirrer, a thermometer and a reflux condenser. The reaction mixture was heated until boiling occurs at around 60 °C, due to the activation of the initiator. The reaction mixture was heated and stirred at a temperature of 77-78 °C for a duration of 3 hours. Upon completion of the reaction (with monitoring via TLC), the succinimide formed was removed by decantation from the still hot mixture. The residue was then left alone for 24 hours before the solvent was distilled off using a rotary evaporator. The remaining residue gradually crystallized over time. To obtain the final product, the crystallized residue was dissolved in benzene whilst being heated and subsequently precipitated using hexane. The overall yield of the product was 63 %.

Bromination of 2,4-dimethyl-3,5-diethoxycarbonylpyrrole with bromine in acetic acid:

3g (0.012 mol) of Knorr pyrrole dissolved in 7.8ml of CH_3COOH was brominated with 7.2 g (0.045 mol) of bromine in 1.2 ml of glacial acetic acid. The temperature during bromination was maintained at 38–45 °C. The starting pyrrole instantly dissolved when bromine in acetic acid was added and a slight exo-effect was observed. The reaction mixture was kept at a temperature of 38–45 °C for 4 hours and after that it was left overnight. The reaction mixture was diluted using chloroform, extracted with cold water twice, and then twice with a saturated solution of sodium carbonate, followed by water, then with a saturated solution of sodium sulfite, and again with water. When treated with sodium sulfite, the solution lost its colour. The extract was dried over sodium sulfate for two hours, and then chloroform was distilled off. The remaining substance was crystallized from hexane with a product yield 33 %.

Bromination of 2,4-dimethyl-3,5-diethoxycarbonylpyrrole with bromine in acetic acid under low heat:

3 g (0.012 mol) of 2,4-dimethyl-3,5-dicarboethoxypyrrole were heated gently in 45 ml of glacial acetic acid. Then, 9.6 g (0.06 mol) of bromine were added at 40–50 °C.The reaction mixture was kept at a temperature of 40–50 °C for 4 hours. The reaction mass did not form crystals when left to stand for 24 hours. The reaction mixture was then cooled to 0 °C, and after thawing at room temperature, a small amount of the precipitated crystals were dissolved. The reaction mixture was poured onto ice and transferred to a separatory funnel. Chloroform was used for extraction, which was carried out thrice. This was then extracted twice with ice water followed by a one-time extraction with a saturated solution of sodium sulfite. Further, it was washed once with water and left to dry over sodium sulfate for 20 hours in a dark place. The yield of the crude product was 30 %. The oily residue was crystallised in hexane, then dissolved in benzene. The crystals precipitated from the solvent mixture and were subsequently recrystallised from benzene.

Bromination of 2,4-dimethyl-3,5-diethoxycarbonylpyrrole in the presence of AlCl₃ as a catalyst:

3 g (0.012 mol) of 2,4-dimethyl-3,5-dicarboethoxypyrrole were placed in a three-necked flask, followed by the addition of 30 ml of chloroform and 0.25 grams of $AlCl_3$ as a catalyst. The mixture was stirred vigorously, and a slight exothermic effect of +6 °C (21–27 °C) was observed. Subsequently, a solution of bromine in chloroform (25 ml of chloroform and 7.2 g (0.045 mol) of bromine) was prepared. The bromine solution was slowly added dropwise, leading to discoloration, and an exothermic effect of +3 °C (27–30 °C) was observed. After the addition of bromine, the temperature of the reaction mixture decreased to 26-27 °C before stabilizing at 25 °C. The mixture was stirred for 4-5 hours before being poured onto ice and extracted with chloroform. The extracted mixture was then washed sequentially with cold water, sodium sulfite and water, and sodium carbonate. Following this, it was dried with calcium chloride and the chloroform extract was filtered off from the calcium chloride before being distilled off. The oily residue was crystallized and the resulting product had a yield of 30 %. After recrystallisation from a mixture of benzene and hexane, the product was found to be soluble in benzene, methanol, chloroform, ethyl acetate, and acetone but had poor solubility in hexane.

Diethyl 5-(dibromomethyl)-3-methyl-2-oxo-2,3-dihydro-1H-pyrrole-3,4-dicarboxylate (5):

IR spectrum, ν, cm^{-1}: 3057 (N-H), 1711 (COOR), 1752 C=O, 1625 (C=C), 675 (C-Br). ^{1}H NMR (400 MHz, CDCl$_3$): δ = 7.89 (s, 1H), 7.57 (d, J = 7.9 Hz, 1H), 7.26 (d, J = 8.1 Hz, 1H), 7.15–7.09 (m, 1H), 7.04–6.98 (m, 1H), 6.88 (d, J = 2.1 Hz, 1H), 4.45 (t, J = 7.4 Hz, 1H), 3.54 (t, J = 6.6 Hz, 2H), 2.25–2.17 (m, 2H), 1.63–1.54 (m, 2H), 1.48–1.37 (m, 2H) ppm; ^{13}C NMR (100 MHz, CDCl$_3$): δ = 136.61, 127.10, 121.71, 121.57, 120.13, 119.58, 118.98, 111.20, 62.91, 62.78, 35.61, 32.80, 24.46 ppm; HRMS (ESI): m/z calcd for [C$_{13}$H$_{16}$NO]$^+$ ([M+H]$^+$) 202.2686, found 202.2651.

Results and Discussion

In light of the findings presented in [13, 14] concerning the phosphorylation of dibrominated Knorr pyrrole, an extensive search was conducted to acquire precise methods for obtaining dibromo derivative **4**. Unfortunately, no viable approaches were discovered in the literature, with the exception of the synthesis procedure for **2** [15, 16]. Consequently, we proceeded to evaluate the subsequent protocols:

– The reaction of two mols of N-bromosuccinimide per one mol of Knorr pyrrole in refluxing carbon tetrachloride with traces of azobis (isobutyronitrile) for initiation.

– The reaction of Knorr pyrrole with excess of bromine (ratio from 1:4 to 1:5) in acetic acid at 40–50 °C.

– The reaction of Knorr pyrrole and excess of bromine in chloroform at 27–30°C in the presence of catalytic amounts of aluminum chloride.

The identical workup was utilised in both previous instances: extracting the reaction mixture in chloroform, washing with an aqueous sodium bicarbonate solution, reducing discoloured bromine residuals with an aqueous sodium sulfite solution, drying the organic phase with sodium sulfite, and recrystallising the solute from benzene or a benzene-hexane mixture. After removing the formed succinimide by filtration, the resulting filtrate was evaporated before reprecipitating the crystal mass with the addition of hexane to a hot solution in benzene.

All three methods for bromination referred to above were partly optimised (refer to Experimental section), but they only produced maximum yields of about 30–60%. To make matters worse, the resulting product was not compound **4**. In each instance, the same crystalline product with a melting point of 132-133 °C was produced.

The ^{1}H NMR spectrum in deuterochloroform displays a singlet at 1.66 ppm (3H), a singlet at 7.58 ppm (1H) and a broad singlet at 8.40 ppm (1H, NH), along with two ethyl group signals from ester radicals. Upon comparison with the Knorr pyrrole spectrum, one methyl group signal vanishes, while the other group's signal shifts by 0.9 ppm to a stronger field. In this instance, it appears that the signal belongs to the region typical of methyl groups attached to the sp^3-hybridized carbon atom. The signal of the ethyl radical from one of the ester groups bears the same structure as that of Knorr pyrrole. However, both methyl and methylene protons resonate in a somewhat stronger field. On the other hand, the signal from the methylene protons of the second ester group is divided into four quartets with coupling constants of 7.2 Hz at 4.14, 4.17, 4.20, and 4.24 ppm. The signals have an intensity ratio of 1:3:3:1, showing that the oxymethylene group is in a complicated steric situation. It is clear that four stable conformers produce distinguishable signals.

Comparison of the ^{13}C NMR spectra of Knorr pyrrole and the resulting product indicates that the carbonyl group signal in the β-position of the pyrrole ring and in one of the carbonyl groups in the product are similar (161.79 and 161.69 ppm, respectively). Conversely, the second carbonyl group signal in the product shifts to 174.88 ppm, falling in the ester group region characterized by the sp^3-hybridized carbon atom. A correlation between the proton and carbon signals of the methyl group (δ 1.66 ppm, δC 18.70 ppm), the carbonyl group, and the carbon nucleus at 26.39 ppm was established. Additionally, there is a correlation between the proton signal of this methyl group and the carbon nucleus signal at 109.25 ppm, where the latter lacks protons. Finally, a correlation has been observed between the protons of the methyl group and the carbon nucleus at 150.24 ppm.

The proton signal at 7.58 ppm corresponds with the signals of the carbon nuclei at 57.87 ppm, 167.00 ppm, and 150.24 ppm. Assuming we accept the assignment of the signals of the dibromomethyl group [19], it becomes evident that this structural fragment is situated at a double bond. Furthermore, analysis of the ^{1}H and ^{13}C NMR spectra of Knorr pyrrole and the resulting product shows that the NH group is preserved during bromination. However, the heteroaromatic system of the pyrrole is disrupted, leaving only a singular C=C double bond in the molecule.

Furthermore, we grew a crystal suitable for X-ray analysis, which revealed the crystal's structure to be of **5** with two bromine atoms. The crystal was found to be identical in composition to Halbig's product (Fig. 4).
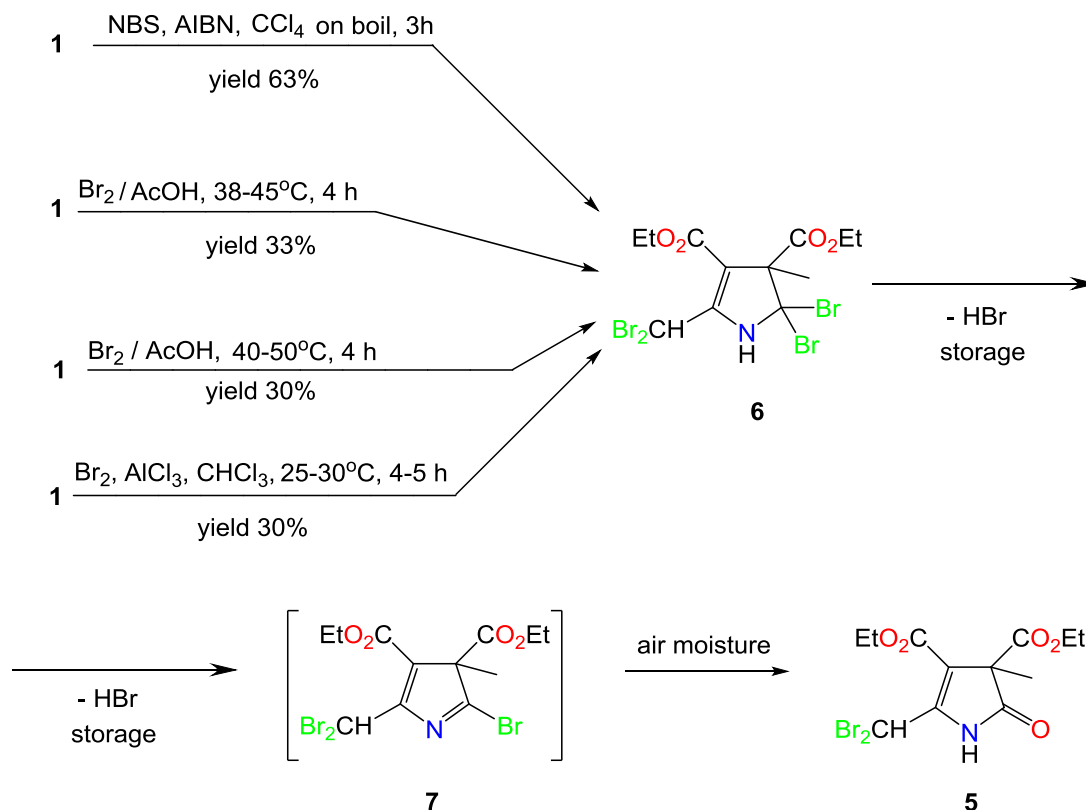
Figure 4. General synthesis scheme of diethyl 5-(dibromomethyl)-3-methyl-2-oxo-
2,3-dihydro-1H-pyrrole-3,4-dicarboxylate (**5**)

The crystal structure of compound **5** consists of neutral molecules. Two of them are always connected by two intermolecular hydrogen bonds. The first is between the nitrogen atom N1 and oxygen atom O5 of the neighboring molecule, and the second one is between O5 and N1 of the same neighboring molecule, forming centrosymmetric pairs. The distance N1 … O5 is 2.811(2) Å and the angle at the H atom is 176.9°. The values of the distances between the bonds in the ring are expected. The shortest one is 1.352(2) Å formally corresponds to the double bond C2–C3, the single bonds C3–C4 and C4–C5 (1.518(1) Å and 1.539(2) Å, respectively) are the longest ones.

The bond distances N1–C2 and N1–C5 are in the expected range. The geometry of dibromomethyl group (C6–Br1 = 1.943(1) Å, C6–Br2 = 1.942(1) Å and the angle at C6 is 109.05(4)° and again the normal range.

However, the order of the substituents on the pyrrole ring is very interesting. Starting from the atom N1, we found dibromo-substituent at C1, ester substituent at C2, another ester substituent together with a methyl group at C3 and O= substituent at C5 (Fig. 5). So, the ester groups are located on adjacent atoms C3, C4. But we started from compound **1,** where the ester substituents are localized on positions 3 and 5 starting from nitrogen atom N1. The structure is shown in Figure 6.

The crystal structure of compound **1** consists of neutral planar molecules. They are connected in endless chains by one medium strong H-bond. Each molecule participates in two identical (due to symmetry) H-bonds. The N1 atom acts as a hydrogen donor and the O1oxygen atom as a hydrogen acceptor. The distance of N1 … O1 is 2.898(x) Å and the angle at the H-atom is 158.0°. Values of the bond distances in the ring are in the range 1.34–1.42 Å. This is the range typical of aromatic pyrroles. Substitution pattern is methyl at C1, ester group at C3, methyl at C4 and ester group at C5 (Fig. 6).
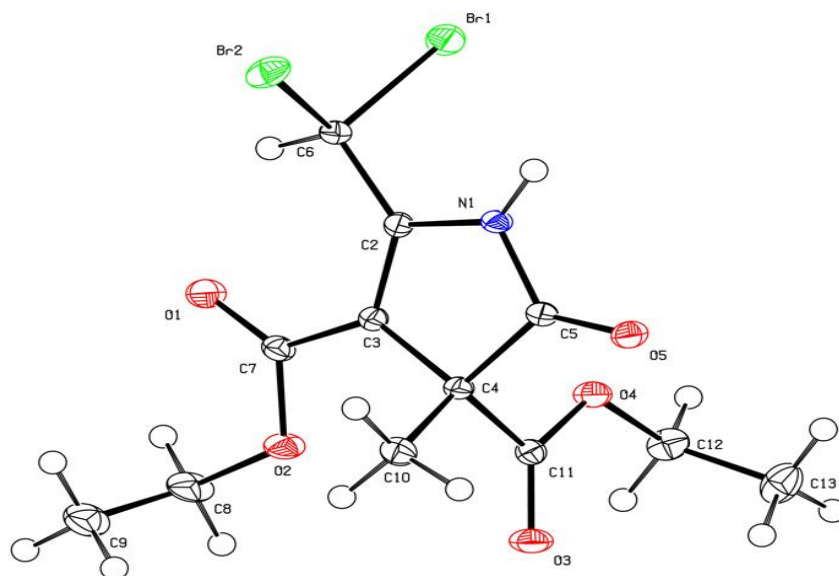
The default probability in Ortep is 60 %

Figure 5.Crystal structural of diethyl 5-(dibromomethyl)-3-methyl-2-oxo-
2,3-dihydro-1H-pyrrole-3,4-dicarboxylate (**5**)
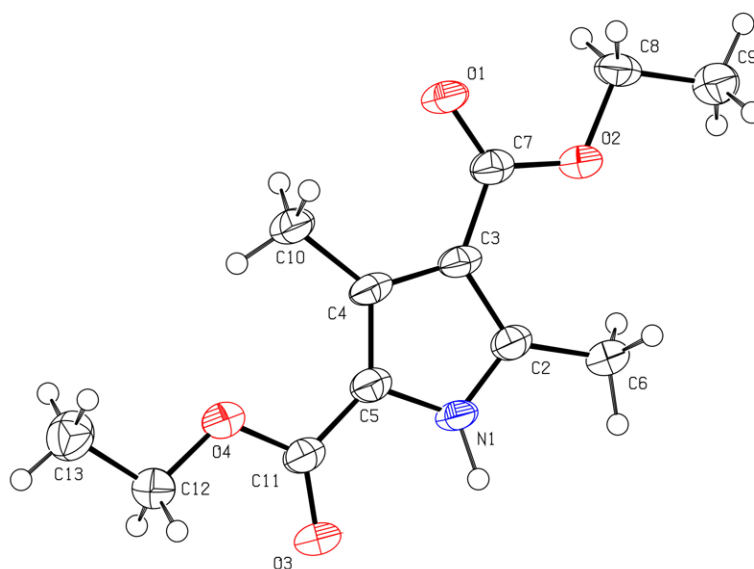
The default probability in Ortep is 60 %

Figure 6. Crystal structural of 2,4-dimethyl-3,5-diethoxycarbonylpyrrole

The basic crystallographic data, measurement and refinement details for compounds **5** and **1** are presented in Table.

T a b l e

Crystallographic data and details of refinements for compounds 5 and 1

Compound	5	1
CCDC no.	2239489	2239477
Empirical formula	$C_{12}H_{15}Br_2NO_5$	$C_{12}H_{17}NO_4$
Formula mass, g mol^{-1}	413.07	239.26
Crystal system	Triclinic	orthorhombic
Space group	P-1 (no. 2)	Fdd2 (no. 43)
a, Å	6.0558(4)	28.4442(15)

Compound	5	1
b, Å	10.1493(5)	38.959(2)
c, Å	12.8464(8)	4.4053(3)
α, deg	81.251(2)	90
β, deg	76.753(2)	90
γ, deg	81.216(2)	90
Z	2	16
V, Å^3	753.89(8)	4881.8(5)
Temperature, K	120(2)	150(2)
$D_{(calcd)}$, g cm^{-3}	1.820	1.302
μ(Mo-Ka), mm^{-1}	5.393	---
μ(Cu-Ka), mm^{-1}	---	0.812
$F(000)$	408	2048
θ_{min}-θ_{max}, deg	2.46 – 30.00	3.85 – 72.28
Reflections collected	20153	16538
No. of unique data	4362	2419
R_{int}	0.0253	0.1214
Obs.refl.ns [$I > 2\sigma(I)$]	4069	1876
Parameters refined	184	158
$R1$, $wR2$ (all data)$^{a, b}$	0.0201;0.0437	0.0835; 0.1657
Residuals, e Å^{-3}	-0.517; 0.684	-0.215; 0.187

$^a w = 1/[\sigma2(Fo2)+(0.0559P)2]$,

$^b w = 1/[\sigma2(Fo2) + (0.0623P)2 + 0.2235P]$, where $P = (Fo2 + 2Fc2)/3$.

The X-ray structural analysis data were deposited in the form of CIF files at the Cambridge Crystallographic Data Center (deposit CCDC no.2239489 for compound **5** and no. 2239477 for compound **1**).

Thus, the above information enables us to present the following sequence of reactions. Bromide **2** reacts with an excess of bromine or bromosuccinimide to form dibromomethyl derivative **8**. Based on the given principles, the improved version is: subsequently, the bromine cation attacks position 2 of the pyrrole ring of the product, resulting in the formation of a σ-complex. During this attack or simultaneously, the ester group is transferred to position 3. Since the reaction with N-bromosuccinimide and bromine leads to the same outcome, we can conclude that:

a) the medium becomes polar enough to cause heterolytic cleavage of the N-Br bond with the formation of the bromine cation due to the presence of succinimide and the significant NH-acidity of the pyrrole derivatives in the reaction mixture;

or b) the process can take place viaboth ionic and radical pathways with the formation of the same endproduct.

In this instance, the final step involves stabilising the reorganised cation, resulting in compound **6**. The compound was obtained in every case when mild conditions were used to treat the reaction mixture. The NMR spectroscopic data accurately describes compound **6**'s structure. It is expected that product **6** will easily cleave hydrogen bromide and convert into tribromide **7**, which has a structure of a cyclic, unsaturated imidoyl bromide. Accordingly, it should react with compounds containing hydroxyl groups (including moisture in the air) to transition to unsaturated lactam **5**, of which the crystal was analyzed by XRD.

The methods for synthesising Halbig's product were discussed in detail previously. The data presented illustrates that the reaction was conducted at high temperatures, with the product washed using hydroxylcontaining substances before being recrystallised from them. Consequently, lactam **5** was the only feasible product under the given conditions. Figure 7 depicts the proposed transformation scheme and mechanism.
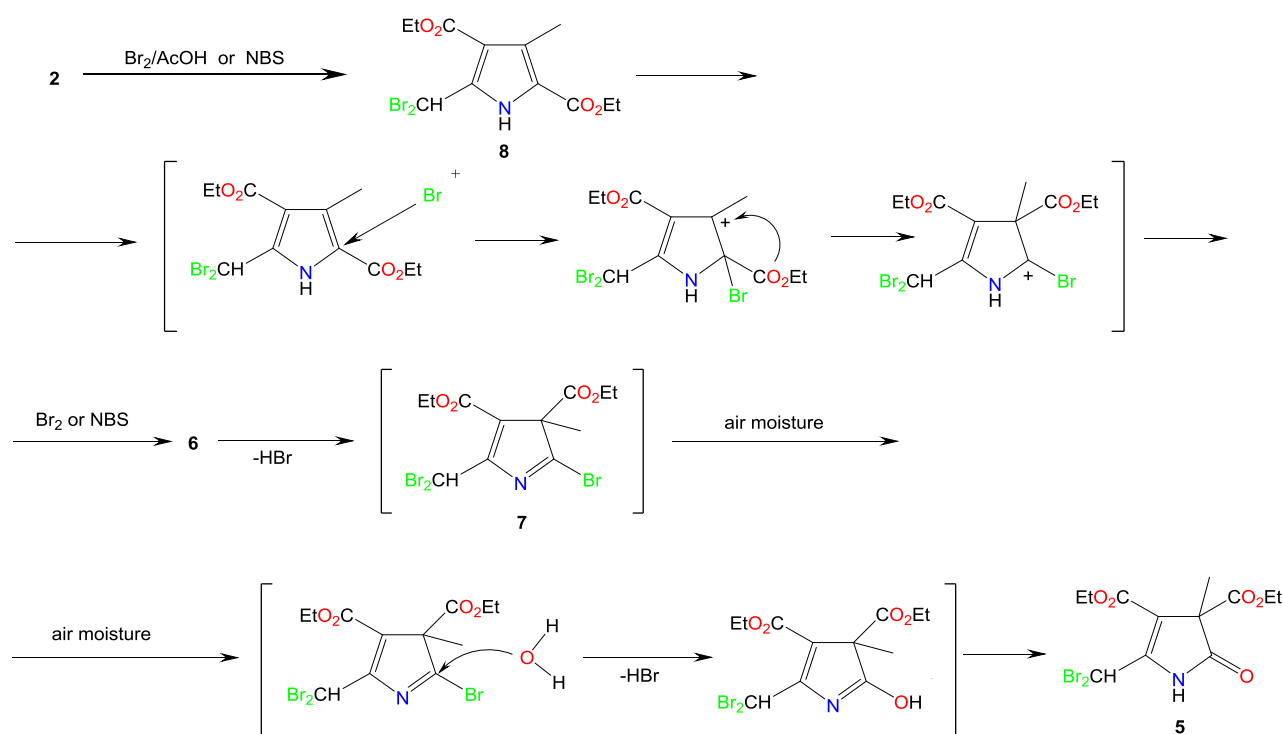
Figure 7. The transformations chain and the proposed mechanism of compound **5** formation

It was discovered that the bromination process of Knorr pyrrole follows a stepwise progression, when carried out with an excess of N-bromosuccinimide or bromine. The methyl group at position 5 is targeted first with the addition of two bromine atoms. Then, the ensuing attack of the bromine cation (or bromine radical) occurs at position 2 of the pyrrole ring, which causes the ester group to transfer to position 3 and disrupts aromaticity of the system. Finally, the integration of one more bromine atom into the molecule stabilises the structure, resulting in the formation of a 2,3-dihydropyrrole derivative. In the presence of bases and substances containing hydroxyl groups, the latter undergoes successive transformations into cyclic imidoyl bromide and ultimately unsaturated lactam **5**. This compound is known as Halbig's product and its true structure was established by our team.

Conclusions

In conclusion, the effort to produce a dibromo derivative of Knorr pyrrole where bromine atoms occupy both allyl positions was not successful, even with the outcomes presented in [13, 14]. The bromination reaction was carried out using 2 mol of N-bromosuccinimide per 1 mol of Knorr pyrrole **1** in carbon tetrachloride by boiling and initiating with azobis(isobutyronitrile), in acetic acid at 40–50 °C at a molar ratio of Knorr pyrrole **1**: bromine 1:5 and at a temperature of 38–45 °C at a molar ratio of Knorr pyrrole **1**: bromine 1:4 and in chloroform at 27–30 °C in the presence of catalytic amounts of aluminum chloride. While all three bromination methods were partially optimized, the yields obtained were limited to 30–63 %. In all instances, we obtained the same crystalline product with a melting point of 132-133 °C. We confirmed the compound's structure of diethyl 5-(dibromomethyl)-3-methyl-2-oxo-2,3-dihydro-1H-pyrrole-3,4-dicarboxylate **5**, with two bromine atoms, through our analysis of ^{1}H and ^{13}C NMR-spectroscopy, mass-spectrometry and X-ray diffraction. This compound is identical in composition to the Halbig's product. These findings demonstrate the lack of systematic research on the β-bromomethylpyrroles' preparation.

Author Information*

———————————————————————————————————————
*The authors' names are presented in the following order: First Name, Middle Name and Last Name

Lyazat Karishovna Salkeyeva — Doctor of Chemical Sciences, Professor, Department of Organic Chemistry and Polymers, Karaganda Buketov University, Universitetskaya str., 28, 100024, Karaganda, Kazakhstan; e-mail: lsalkeeva@mail.ru; https://orcid.org/0000-0003-4207-916X

Leonid Markovich Pevzner — Candidate of Chemical Sciences, Senior Researcher, Department of Organic Chemistry, Saint Petersburg State Technological Institute (Technical University), Moskovsky prospect, 26, 190013, Saint Petersburg, Russian Federation; e-mail: pevzner_lm@list.ru; https://orcid.org/0000-0002-1678-2524

Pavel Vojtíšek — Associate Professor RNDr., CSc. Jan Evangelista Purkyně University in Ústí nad Labem, Department of Chemistry, Faculty of Science, Pasteurova 3632/15, Ústí nad Labem, 400 96, Czech Republic; e-mail: pavojt@natur.cuni.cz; https://orcid.org/0000-0002-4685-9238

Yelena Viktorovna Minayeva (*corresponding author*) — Candidate of Chemical Sciences, Associate Professor, Department of Organic Chemistry and Polymers, Karaganda Buketov University, 100024, Karaganda, Kazakhstan; e-mail: yelenaminayeva@yandex.ru; https://orcid.org/0000-0001-9382-5965

Author Contributions

The manuscript was written through contributions of all authors. All authors have given approval to the final version of the manuscript. CRediT: **Lyazat Karishovna Salkeyeva** conceptualization, methodology, data curation, writing-review & editing, supervision; **Leonid Markovich Pevzner** resources, investigation,methodology, data curation, formal analysis, visualization, validation, writing-original draft; **Pavel Vojtíšek** investigation, resources, data curation, formal analysis, writing-original draft; **Yelena Viktorovna Minayeva** investigation, validation, writing-original draft, writing-review & editing.

Conflicts of Interest

The authors declare no conflict of interest.

References

1 Ivan, B.-C., Barbuceanu, S.-F., Hotnog, C.M., Anghel, A.I., Ancuceanu, R.V., Mihaila, M.A., Brasoveanu, L.I., Shova, S., Draghici, C., Olaru, O.T., Nitulescu, G.M., Dinu, M., & Dumitrascu, F. (2022). New Pyrrole Derivatives as Promising Biological Agents: Design, Synthesis, Characterization. In *Silico, and Cytotoxicity Evaluation.Int. J. Mol. Sci.,* 23, 8854. https://doi.org/10.3390/ijms23168854

2 Jeelan Basha, N., Basavarajaiah, S.M., & Shyamsunder, K. (2022). Therapeutic potential of pyrrole and pyrrolidine analogs: An update. *Mol. Divers.*, 1–23. https://doi.org/10.1007/s11030-022-10387-8

3 Mateev, E., Georgieva, M., & Zlatkov, A. (2022). Pyrrole as an Important Scaffold of Anticancer Drugs: Recent Advances. *J. Pharm. Pharm. Sci.*, *25*, 24–40. https://doi.org/10.18433/jpps32417

4 Azad, I., Jafri, A., Khan, T., Akhter, Y., Arshad, M., Hassan, F., Ahmad, N., Khan, A.R., & Nasibullah, M. (2019). Evaluation of pyrrole-2,3-dicarboxylate derivatives: Synthesis, DFT analysis, molecular docking, virtual screening and in vitro anti-hepatic cancer study. *J. Mol. Struct.*, *1176*, 314–334. https://doi.org/10.1016/j.molstruc.2018.08.049

5 Imperatore, C., Scuotto, M., Valadan, M., Rivieccio, E., Saide, A., Russo, A., Altucci, C., Menna, M., Ramunno, A., Mayol, L.,Russo G., & Varra M. Photo-control of cancer cell growth by benzodiazo N-substituted pyrrole derivatives. *J. Photochem. Photobiol. A Chem.* (2019), *377*, 109–118. https://doi.org/10.1016/j.jphotochem.2019.03.042

6 Rashmi, K.C., Harsha Raj, M., Paul, M., Girish, K.S., Salimath, B.P., & Aparna, H.S. (2019). A new pyrrole based small molecule from Tinosporacordifoliainduces apoptosis in MDA-MB-231 breast cancer cells via ROS mediated mitochondrial damage and restoration of p53 activity. *Chem.-Biol. Interact.*, *299*, 120–130. https://doi.org/10.1016/j.cbi.2018.12.005

7 Khalilpour, A., & Asghari, S. (2018). Synthesis, characterization and evaluation of cytotoxic and antioxidant activities of dihydropyrimidone substituted pyrrole derivatives. *Med. Chem. Res.*, *27*, 15–22. https://doi.org/10.1007/s00044-017-2041-4

8 Sowmya, P.V., Poojary, B., Kumar, V., Vishwanatha, U., & Shetty, P. (2017). Fluorinated pyrrole incorporated 2-thiazolyl hydrazone motifs: A new class of antimicrobial and anti tuberculosis agents. *Arch. Pharmacal Res.*, 1–21. https://doi.org/10.1007s12272-017-0967-1

9 Jung, E.K., Leung, E., & Barker, D. (2016). Synthesis and biological activity of pyrrole analogues of combretastatin A-4. *Bioorganic Med. Chem. Lett.*, *26*, 3001–3005. https://doi.org/10.1016/j.bmcl.2016.05.026

10 Carvalho, R.C.C., Martins, W.A., Silva, T.P., Kaiser, C.R., Bastos, M.M., Pinheiro, L.C.S., Krettli, A.U., &Boechat, N. (2016). New pentasubstituted pyrrole hybrid atorvastatin-quinoline derivatives with antiplasmodial activity. *Bioorg. Med. Chem. Lett.*, *26*, 1881–1884. https://doi.org/10.1016/j.bmcl.2016.03.027

11 Sarg, M.T., Koraa, M.M., Bayoumi, A.H., & Gilil, S.M.A.E. (2015). Synthesis of Pyrroles and Condensed Pyrroles as Anti-Inflammatory Agents with Multiple Activities and Their Molecular Docking Study. *Open J. Med. Chem.*, *05*, 49–96. https://doi.org/10.4236/ojmc.2015.54005

12 Battilocchio, C., Poce, G., Alfonso, S., Porretta, G.C., Consalvi, S., Sautebin, L., Pace, S., Rossi, A., Ghelardini, C., Di Cesare Mannelli, L.D.C., Schenone, S.,Giordani, A., Francesco, L.D., Patrignani, P., & Biava, M. (2013). A class of pyrrole deriva-

tives endowed with analgesic/anti-inflammatory activity. *Bioorganic Med. Chem.*, *21*, 3695–3701. https://doi.org/10.1016/j.bmc.2013.04.031

13 Gurevich, P.A., & Yaroshevskaya, V.A. (2000). Phosphorus-containing Derivatives of Indole and Pyrrole. (Review). *Chem. Heterocycl. Compd.*, *36*, 1361–1401. https://doi.org/10.1023/A:1017562111215

14 Gurevich, P.A., Moskva, V.V., & Kiselev, V.V. (1993). Uspekhi nauki i tekhnolohii. Orhanicheskaia khimiia [Advances of Science and Technology. Organic Chemistry]. VINITI, Moscow, *30*, 3[in Russian].

15 Fischer, H., & Scheyer, H. (1923). Einwirkung von Brom auf substituierte Pyrrole und Synthese in α-Stellung bromierter Dipyrrylmethen-Farbstoffe. *Justus Liebigs Annalen der Chemie*, *434*(1), 237–251.

16 Fischer, H., & Ort, G. (1937). Chemistry of Pyrrole [Russian translation]. *ONTI, Leningrad*, 122.

17 Halbig, P., & Walach, B. (1927). *Justus Liebigs Annalen der Chemie*, *457*, 245.

18 Kutscher, W., & Klamerth, O. (1950). *Hoppe-Seyler'sZeitschrift fur Physiologische Chemie*, *286*, 191.

19 Angelini, G., Giancaspro, C., Illuminati, G., & Sleiter, G. (1980). Electrophilic heteroaromatic reactions. 3[1]. The α-side-chain bromination of some polysubstitutedα-methylpyrroles in the dark. Evidence for the formation of intermediate σ adducts.*J. Org. Chem.*, 45, 10, 1786–1790. https://doi.org/10.1021/jo01298a009

20 Byun, Y., & Lightner, D.A. (1991). Synthesis and properties of a bilirubin analog with propionic acid groups replaced by carboxyl. *Journal of Heterocyclic Chemistry, 28*(7), 1683–1692. Portico. https://doi.org/10.1002/jhet.5570280707

21 Treibs, A., & Bader, H. (1959)**.** *Justus Liebigs Annalen der Chemie*, *627*, 182.

22 Sheldrick, G.M. (2014). SHELXT-2014. Program for Crystal Structure Solution from Diffraction Data. *University of Göttingen: Göttingen.*

23 Sheldrick, G. M. (2015). Crystal structure refinement with SHELXL. *Acta Crystallographica Section C: Structural Chemistry*, *71*(1), 3–8. https://doi.org/10.1107/S2053229614024218

Arshyn Zhengis[1, 2] (iD), Yenglik Amrenova[1] (iD), Arailym Yergesheva[1] (iD),
Dana Kanzhigitova[2] (iD), Gulim Imekova[1] (iD), Zhexenbek Toktarbay[3] (iD),
Olzat Toktarbaiuly[1] (iD), Munziya Abutalip[1*] (iD), Nurxat Nuraje[1] (iD)

¹National Laboratory Astana, Nazarbayev University, Astana, Kazakhstan;
²Al-Farabi Kazakh National University, Almaty, Kazakhstan;
³Laboratory of Engineering Profile, Satbayev University, Almaty, Kazakhstan
(*Corresponding author's e-mail: munziya.abutalip@nu.edu.kz)

Structural Studies and Applications of Sulfobetaine-Based Polybetaines at Interfaces

The main goals of this research endeavor are to enhance the hydrophilic properties and water permeability of a nanofiltration membrane. This is achieved by incorporating a Zeolitic imidazolate framework (ZIF-8) layer that has been stabilized utilizing a redox-grafted methacrylate hydrogel. The decision to use polyacrylonitrile (PAN) as the substrate material was motivated by its intrinsic hydrophilic properties, which contribute to its ability to resist fouling and promote water permeability. The shift of the surface from hydrophilic to superhydrophilic was confirmed using physicochemical evaluations, including scanning electron microscopy (SEM) and contact angle measurements. Hydrolyzed Polyacrylonitrile Zeolitic imidazolate framework grafted (HPANZifG) membrane exhibited a remarkably high-water flux of 82.3 L/m² Bar hour, which is an achievement of notable significance. This study makes a valuable contribution to the advancement of nanofiltration technology by proposing potential solutions to the challenges faced in the field of water purification and treatment.

Keywords: Sulfobetaine, Zwitterionic polymer, membrane modification, nanofiltration, Metal-Organic Framework (MOF), ZIF-8 layer, redox grafting, water flux, polyacrylonitrile (PAN).

Introduction

Water is an essential requirement for the sustenance of both human societies and ecological systems that exist within the confines of the planet Earth. The fraction of freshwater within the Earth's total water resources is estimated to be around 2.5 %. This percentage has undergone a decline due to several factors, including contamination and the impacts of climate change [1, 2]. According to recent research conducted by the World Health Organization (WHO), a considerable segment of the global population, comprising more than 1.6 billion individuals, confronts the issue of insufficient access to water sources that adhere to the necessary safety criteria [3–6]. It is anticipated that by the year 2025, almost 50 % of the global population would inhabit areas that are confronted with substantial water scarcity issues [7].

Currently, there are three viable strategies that show potential in enhancing clean water resources and effectively addressing the issue of water scarcity. The first approach involves facilitating the reuse of water obtained from wastewater and other sources of degraded water. The second approach entails extracting freshwater from seawater through the process of desalination. Lastly, the third approach involves the collection of moisture from the atmosphere [8].

At present, the issue has become an urgent matter for scientists to solve worldwide. The current technology used includes thermal, chemical, and membrane. Among them, the membrane technology is the most popular for desalination of water. Membrane technology is divided in two: reverse osmosis and electrodialysis.

Electrodialysis method is economical, operational at room temperature and continuous process. Nevertheless, the disadvantages include the removal of colloidal impurities, and the consumption of a huge amount of electricity. On the contrary, the reverse osmosis semipermeable membrane is a robust technology, easily eliminating colloidal and suspended impurities. A sustainable water supply system is feasible with this type of method due to its cost-effectiveness. The membrane-based advanced technologies could potentially offer a sustainable technical solution to global resource shortages. However, the establishment of sustainable mem-

brane technologies with energy-efficient, eco-benign and scalable separation in comparison with conventional processes is still challenging [9].

Zwitterions are molecular entities characterized by an equal number of positive and negative charges that are connected by covalent bonds. These molecules possess remarkable resistance to fouling, which can be attributed to their significant level of hydration. Numerous studies have utilized the characteristic of zwitterionic groups to improve resistance against fouling [10, 11]. This has been achieved through two main approaches: altering the surface chemistry of the membrane to incorporate zwitterionic moieties [12–15], or applying zwitterionic hydrogels as coatings on the membranes. Zwitterions exhibit a high degree of polarity, hence inducing microphase separation in many copolymer systems containing zwitterionic moieties [16, 17].

Polymers possess favorable characteristics in terms of their ability to create membranes and their cost-effectiveness as resources [18]. Various efficient techniques, including non-solvent induced phase separation (NIPS), interfacial polymerization, and solution coating, have been widely adopted for the fabrication of polymer membranes, which currently hold a prominent position in the membrane market [19]. However, in typical cases, dynamic polymer chains are commonly interwoven and densely packed, leading to limited available spaces with varying diameters. These features not only increase the difficulty to mass movement over the membrane, but also decrease the precision of separation. Consequently, the implementation of nanofluidics transport in traditional polymer membranes has been limited. In recent studies, it has been discovered that the incorporation of twisted monomers [20] and crystalline porous organic frameworks [21] can significantly improve the structural stiffness and microporosity of polymer membranes. Metal-organic frameworks (MOFs) are a novel class of porous crystalline materials that combine organic and inorganic components. These materials possess a large surface area and can be tailored to have specific pore structures. They have been extensively employed in the production of separation membranes using different techniques such as physical blending, direct/secondary growth, layer-by-layer assembly, and contra-diffusion methods [22]. While MOF-based membranes do demonstrate enhanced water penetration, the formation of continuous nanochannels in the membrane without intercrystallite cracks remains a significant challenge. Furthermore, it should be noted that the water permeability of these membranes is currently subpar when compared to state-of-the-art nanofluidic membranes. Additionally, the synthetic process for these membranes is somewhat complex. Hence, the development of efficient polymeric nanofluidic membranes continues to be a complex and unresolved task in the field of advanced molecular separation [23].

The main goal of this research was to establish a chemical method for stabilizing a ZIF-8 layer on an ultrafiltration membrane using a redox-grafted methacrylate hydrogel. This approach aimed to enhance the water flux and hydrophilicity of the membrane. The selection of the polyacrylonitrile (PAN) membrane as the porous support was based on its hydrophilic properties, which contribute to improved antifouling effects and water permeability. The confirmation of the chemical structure of the membrane was achieved by the utilization of attenuated total reflectance-Fourier transform infrared (ATR-FTIR) spectroscopy. The membranes were subjected to physicochemical evaluation using scanning electron microscopy (SEM) and contact angle measurements. The membrane's performance in terms of pure water permeance was assessed in order to showcase the effectiveness of the synthesized membrane in water treatment applications.

Experimental

Materials

Polyacrylonitrile (PAN) powder with a weight-average molecular weight (Mw) of 150 000 g/mol was purchased from Sigma-Aldrich, Polyvinyl pyrrolidone (PVP) 29 000 g/mol, [2 (Methacryloyloxy)ethyl] dimethyl-(3-sulfopropyl) ammonium hydroxide (SBMA, ~95%), N,N'-methylenebisacrylamide (MBA, ~99 %), zinc nitrate hexahydrate (~99 %), N,N-Dimethylformamide (DMF,~99.8%), 1-vinylimidazole (1-VIM ~99 %).

Fabrication of the membranes

Figure 1 illustrates the schematic preparation of the zwitterionic PAN membrane. To enhance membrane porosity, we introduced PVP as a pore-forming agent, guided by previous studies [24]. PVP, recognized for its CH_2, C–O, and C–N functional groups, serves as an effective pore-forming agent, increasing the number of pores per unit surface area without altering their size or distribution, as documented in the literature [25]. For the preparation of a homogeneous casting solution, 11 wt. % PAN powder and 5 wt % PVP were dissolved in DMF. This polymer ratio of PAN to PVP was meticulously selected to pursue optimal

membrane properties, capitalizing on the unique advantages associated with PVP in membrane synthesis. The mixture was dropped onto a clean glass plate and then was cast with a knife (150 μm). The liquid PAN membrane was solidified in a pure water bath. The hydrolyzed membrane (PAN-COOH) was prepared by immersing the pure PAN membrane samples in a NaOH solution (2 mol/L) at 60 °C for 1.5 hours. It was then extensively washed with distilled water until pH neutrality. The hydrolyzed membrane is referred to here as the HPAN.

The synthesis of ZIF-8 nanoparticles within the HPAN membrane.

The HPAN membrane was incubated in an aqueous solution of $Zn(NO_3)_2 \cdot 6H_2O$ (1.25 g in 50 mL) for 12 hours with shaking. The $Zn(NO_3)_2 \cdot 6H_2O$ aqueous solution was discarded, the membrane was washed with distilled water for 15 seconds, treated with an aqueous solution of 1-VIM (2.75 g in 50 mL) for 1 hour with shaking, then gently washed three times with 50% aqueous methanol. The HPAN membrane with in situ-grown ZIF-8 nanoparticles is referred to as the HPANZif membrane.

Redox-initiated graft polymerization on the membrane

The membrane was initially treated with an aqueous solution of 1.0 M SBMA (40 mL) containing 5 wt% MBA (as a crosslinker) and shaken for 10 minutes before adding 0.2 M $K_2S_2O_8$ aqueous solutions (10 mL) in sequence and shaking for 40 minutes. The reaction was stopped by removing the reaction mixture and washing the membrane thoroughly with distilled water. The HPANZif membrane corresponds to the HPANZif-Grafted membrane.
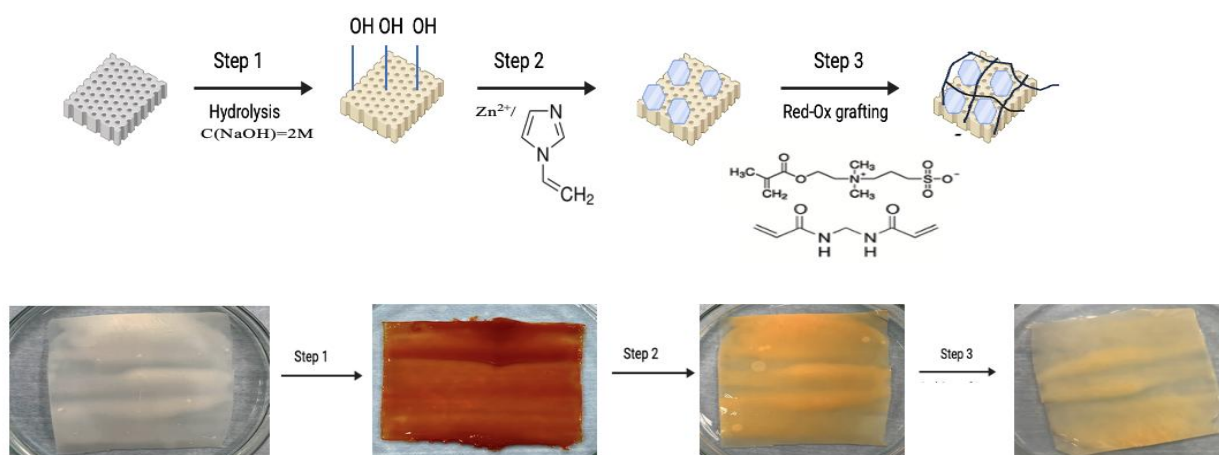
Figure 1. Preparation of HPANZif-grafted membrane

Characterization

Fourier transform infrared spectroscopic investigation was carried out using the Nicolet iS10 FT-IR spectrometer. In the FTIR analysis of polymers, a small amount of the sample was placed at the center of the ATR plate's diamond crystal. Gentle pressure was applied to ensure contact. A background spectrum was recorded for reference. The FTIR spectrum was recorded using a calibrated instrument. The ATR plate was cleaned to prevent contamination. These steps ensured accurate polymer characterization.

Scanning electron microscopy ZEISS, Crossbeam 540 was used to observe the surface and cross-section structure. In SEM analysis of membranes, a 10 nm gold coating is applied using a high-vacuum coater for enhanced conductivity and sample detail preservation. A 15 kV electron beam was used for all the membrane samples.

Automatic Sputter Coater Q150T was employed to coat the surfaces of the samples. The water contact angle (WCA) of membrane was evaluated by a water contact angle instrument Dataphysics OCA 15Pro. To ascertain contact angle values, a 5μL droplet volume was utilized, and contact angle measurements were conducted immediately after the droplet was dispensed onto the membrane surface.

All membrane samples were dried overnight before characterization.

Water Flux in Membrane Systems

The membranes' pure water flux was evaluated at 1 bar using dead- end stirred cell filtration experiments. After achieving a steady flow with at least 30 minutes of filtration, the pure water flux of each membrane was calculated using Equation (1):

$$\text{Pure water flux} = \frac{V}{A \times P \times t}, \tag{1}$$

where V is the volume of permeate water (L), A is the effective membrane area, and t is the time length (h). For each membrane, at least three readings were collected.

Results and Discussion

The central objective of this research project was to develop a specialized membrane that had been modified with the zwitterionic ZIF-8. This tailored membrane was envisioned to exhibit significantly enhanced water permeability, exceptional resistance to salt, and an outstanding ability to effectively remove salt during the treatment of seawater. The goal was to address the critical need for more efficient and robust membranes in the fields of desalination and seawater treatment, ensuring a sustainable and reliable source of freshwater in regions with limited access to clean water resources.

Figure 2 shows the FTIR spectra of the changed membranes, which are presented in comparison to the pristine PAN membrane. The FTIR spectrum of the pristine PAN membrane had peaks at 1451 cm^{-1} and 2243 cm^{-1}, corresponding to the C–N stretching of the –C≡N group. Hydrolysis of the PAN membrane (HPAN membrane) resulted in prominent peaks at (3369 cm^{-1}) corresponded to the O–H moieties of carboxyl groups on the membrane surface. The appearance of the peak confirmed partial hydrolysis of the PAN membrane. In situ growth of ZIF-8 nanoparticles on the HPAN membrane provided HPANZif membrane, which showed peaks characteristic of ZIF-8 nanoparticles (652cm^{-1}), corresponding to the stretching vibrations of the ZnO bond in octahedral coordination, the bending vibration of the imidazole ring, the bending vibration of the –CH$_2$ (757 cm^{-1} group in 1-vinyllimidazole respectively. The appearance of these peaks confirmed the presence of ZIF-8 nanoparticles on the membrane surface. Grafting poly (methacrylate) hydrogel on HPAN membrane provided HPANZifG membrane with peaks at 1043 cm^{-1} (sulfonate S=O stretch), 3188 cm^{-1}, 1563 cm^{-1} (CO–NH) stretching vibration of the amide group, corresponding to the stretching vibration of N–H in the amide groups of poly(MBA-co-SBMA). The appearance of these peaks confirmed the presence of grafted methacrylate hydrogel on the membrane surface. The FITR spectrum of the HPANZifG membrane had peaks characteristic of the ZIF-8 nanoparticles (observed in the FTIR spectrum of the HPANZif membrane) and from grafted methacrylate hydrogel, confirming modification of the membranes with the ZIF-8 nanoparticles and grafted hydrogel. These various groups on the surface of the membranes affect the surface properties of the membranes.
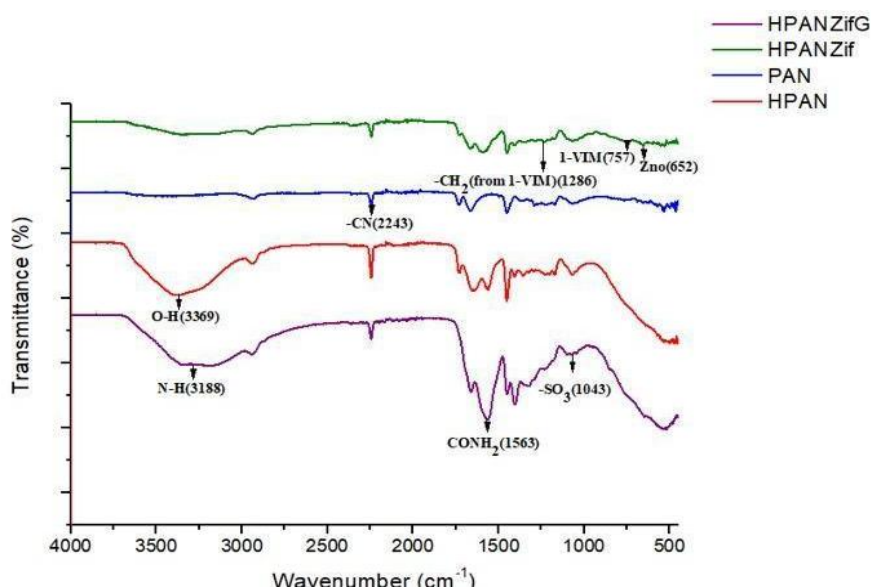

Figure 2. FTIR spectra of prepared membranes.
The presence of characteristic functional groups on the membranes confirmed the modifications

Morphological Analysis of the Membranes

SEM was used to examine the morphology of the produced membranes. The formed membrane's cross-sectional morphology, as shown in Figure 3 consists of a skin layer and a porous sublayer, which result from the instantaneous phase separation of the PAN casting solution during manufacture. It should be noted that the surface grafting of PSBMA chains had no influence on the cross-sectional morphology of the membranes. Figure 3 depicts the surface structures of the membranes PAN (surface: 300 nm, cross-section: 1 μm), HPAN (surface: 300nm, cross-section: 1μm), HPANZif (surface: 1μm, cross-section: 3μm), and HPANZifG (surface: 300nm, cross-section: 1μm). Micropores form on the PAN membrane surface, whereas new, larger holes form on the PAN-COOH membrane due to pore formation during C≡N hydrolysis.
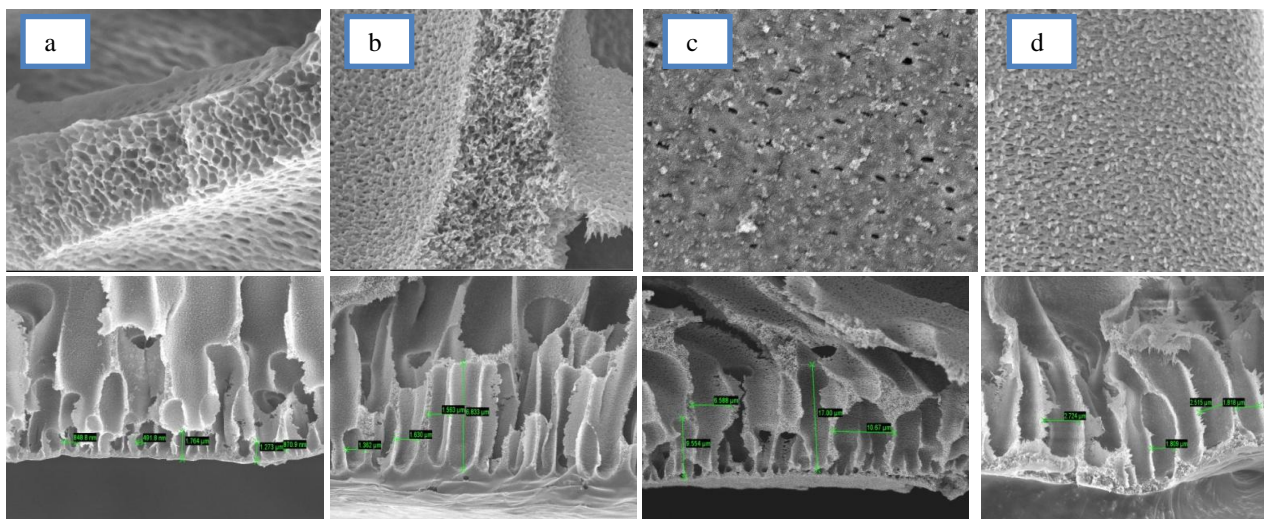
a — PAN (surface: 300 nm, cross-section: 1 μm); *b* — HPAN (surface: 300 nm, cross-section: 1 μm);
c — HPANZif (surface: 1 μm, cross-section: 3 μm), *d* — HPANZifG (surface: 300 nm, cross-section: 1 μm)

Figure 3. Surface and Cross-Section SEM Images of Zwitterion Modified PAN Membranes

The cross-sectional images of these membranes provide unambiguous visual evidence of the sizes of the continuous water channels, which displayed an average size.

The channels in the unaltered PAN membrane had a diameter of 736 nm, which is a commonly observed dimension for pristine PAN membranes.

Upon undergoing hydrolysis to generate HPAN, the resulting cross-sectional image had a diameter measuring 1,525 μm. The observed increased dimensions are commonly observed in hydrolyzed polyacrylonitrile (PAN) membranes.

The HPANZif membrane, which integrates a Metal-Organic Framework (MOF), exhibited a significant augmentation in channel diameter, reaching a value of 8,629 μm. The significant rise can be attributed mostly to the organized crystal channels present in the MOF substance. These channels provide a clearly defined route for water molecules, hence substantially improving water permeability.

The cross-sectional image of the HPANZifG membrane reveals a significant augmentation in the diameter of water channels as compared to the unmodified PAN membrane. Nevertheless, the precise numerical value for this diameter is not included in the available data. However, it is evident that the incorporation of zwitterions greatly enhances the permeability of water channels, resulting in a membrane that exhibits increased hydrophilicity and facilitates efficient water transportation.

In conclusion, the cross-sectional photographs of the membranes revealed the dimensions of their uninterrupted water channels, and it is worth mentioning that all of the membranes had sizes falling within the average spectrum. The provided information highlights the conventional or customary channel dimensions for each of the individual alterations, which might be significant when assessing their efficacy in diverse applications such as desalination and filtration.

Surface Wettability of the Membranes

The surface wettability of the prepared membranes was characterized based on the dynamic contact angles in pure water. Figure 4 presents a collection of contact angle data that offer a comprehensive analysis of

the surface properties shown by PAN, HPAN, HPANZif, and HPANZifG membranes. The initial contact angles provide insight into the wettability of the membranes. The PAN membrane demonstrates an initial contact angle of approximately 60°±2°, indicating a surface that is moderately hydrophilic and promotes the wetting and spreading of water droplets. In contrast, the HPAN, HPANZif, and HPANZifG materials exhibit lower initial contact angles, precisely measuring at 35°±1.5°, 30°±0.8°, and 15.5°±1.1°, respectively. These values indicate a noticeable tendency towards the development of hydrophilic surfaces that facilitate the rapid spreading of water droplets.
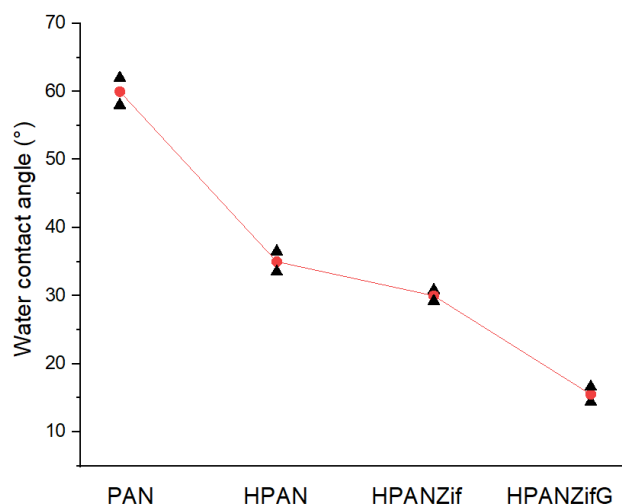
Figure 4. The water contact angles of PAN membranes supplemented by zwitterion

The observed decrease in contact angle across the membranes suggests a significant transition from hydrophilic to super hydrophilic surfaces, which can be attributed to the integration of extremely hydrophilic functional groups. Significantly, in the instance of HPANZif, the incorporation of MOFs results in the formation of crystalline structures with continuous water channels. This introduces a well-organized and porous framework that effectively boosts the membrane's hydrophilic properties. The presence of hydrophilic functional groups, in conjunction with other factors, leads to the observation of remarkably low initial contact angles. This further strengthens the hyper hydrophilic characteristics exhibited by these surfaces.

The utilization of zwitterionic functional groups and MOF structures to improve surface wettability has significant ramifications in various scientific and industrial applications. This is particularly important in situations where efficient water transport and strong interactions with material surfaces are crucial.

The differences in pure water flux among PAN, HPAN, HPANZif, and HPANZifG membranes, as shown in Figure 5, are significant. These values represent the average pure water permeances, with respective measurements of 60.32, 65.89, 76.05, and 82.3 L/h·bar·m^2.
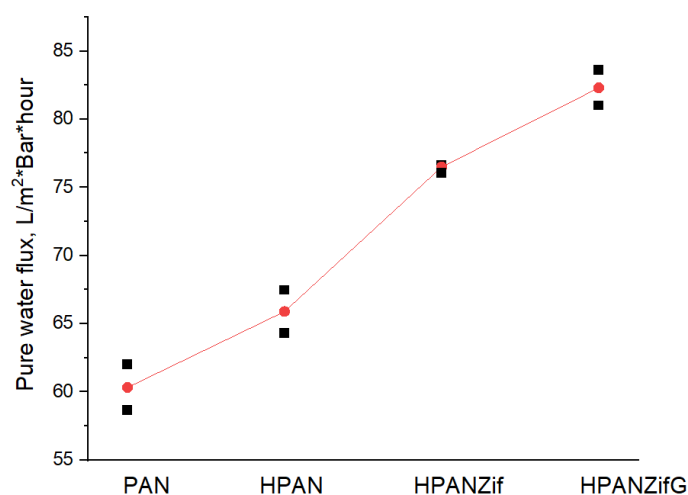
Figure 5. Pure water permeance of the prepared membranes

The HPANZifG material exhibits the maximum water flux due to the presence of uninterrupted water channels and the grafting of zwitterions. The alterations made facilitate an atmosphere that is favorable for efficient water transportation, leading to the notable increase in water permeance reported in HPANZifG.

In summary, there exists a positive correlation between a decrease in water contact angle and an increase in water flux. The aforementioned relationship highlights the correlation between reduced contact angles and the improved wettability and efficiency of water transport on surfaces.

Conclusions

In conclusion, the present study effectively accomplished its main objective of augmenting the hydrophilic properties and water permeability of the nanofiltration membrane. The incorporation of a ZIF-8 layer that has been stabilized using a redox-grafted methacrylate hydrogel, specifically in the HPANZifG membrane, led to a noteworthy water permeance of 82.3 L/m^2 Bar hour. The selection of polyacrylonitrile (PAN) as the substrate material, renowned for its hydrophilic capabilities, had a significant role in enhancing water permeability and mitigating fouling tendencies.

The alteration of the membrane's surface from hydrophobic to super hydrophilic was established through comprehensive physicochemical tests. The aforementioned results establish the synthesized membrane as a highly viable option for water treatment purposes, as it demonstrates commendable efficacy in water transportation and exhibits notable resistance against fouling. This study introduces novel prospects in the field of nanofiltration technology, which holds considerable ramifications for the advancement of water purification and treatment.

Funding

Author Information*

_____

*The authors' names are presented in the following order: First Name, Middle Name and Last Name

Arshyn Zhengis — 2nd year PhD Student, Al-Farabi Kazakh National University, Al-Farabi Ave., 71, 050040, Almaty, Kazakhstan; e-mail: arshyn.zhengis@nu.edu.kz; https://orcid.org/0000-0001-8770-4147

Yenglik Amrenova — Research Assistant, National Laboratory Astana, Nazarbayev University, Kabanbay batyr Ave., 53, 010000, Astana, Kazakhstan; e-mail: yenglik.amrenova@nu.edu.kz; https://orcid.org/0009-0005-1684-1845

Arailym Yergesheva — Research Assistant, National Laboratory Astana, Nazarbayev University, Kabanbay batyr Ave., 53, 010000, Astana, Kazakhstan; e-mail: arailym.yergesheva@nu.edu.kz; https://orcid.org/0009-0003-0055-7298

Dana Kanzhigitova — PhD Candidate, Al-Farabi Kazakh National University, Al-Farabi Ave., 71, 050040, Almaty, Kazakhstan; e-mail: dana.kanzhigitova@nu.edu.kz; https://orcid.org/0000-0003-3445-584X

Gulim Imekova — Research Assistant, National Laboratory Astana, Nazarbayev University, Kabanbay batyr Ave., 53, 010000, Astana, Kazakhstan; e-mail: gulim.imekova@nu.edu.kz; https://orcid.org/0000-0003-4774-6646

Zhexenbek Toktarbay — PhD, National Laboratory Astana, Nazarbayev University, Kabanbay batyr Ave., 53, 010000, Astana, Kazakhstan; e-mail: zhexenbek.toktarbay@gmail.com; https://orcid.org/0000-0003-4131-0905

Olzat Toktarbaiuly — PhD in Phyical Sciences, Researcher, National Laboratory Astana, Nazarbayev University, Kabanbay batyr avenue, 53, 010000, Astana, Kazakhstan; e-mail: olzat.toktarbaiuly@nu.edu.kz; https://orcid.org/0000-0003-4594-3435

Munziya Abutalip — PhD, National Laboratory Astana, Nazarbayev University, Astana, Kabanbay batyr Ave., 53, 010000, Astana, Kazakhstan; e-mail: munziya.abutalip@nu.edu.kz; https://orcid.org/0000-0003-2200-8479

Nurxat Nuraje — Professor, National Laboratory Astana, Nazarbayev University, Kabanbay batyr Ave., 53, 010000, Astana, Kazakhstan; e-mail: nurxat.nuraje@nu.edu.kz; https://orcid.org/0000-0003-4751-2719

Author Contributions

The manuscript was written through contributions of all authors. All authors have given approval to the final version of the manuscript. CRediT: **Arshyn Zhengis** and **Yenglik Amrenova** conceptualization, data curation, investigation, methodology, validation, visualization, writing-original draft, writing-review & editing; **Arailym Yergesheva, Dana Kanzhigitova,** and **Gulim Imekova** formal analysis, visualization; data curation, formal analysis; **Zhexenbek Toktarbay** and **Olzat Toktarbaiuly** conceptualization, data curation; **Munziya Abutalip** and **Nurxat Nuraje** funding acquisition, resources, supervision, validation, writing-review & editing.

Acknowledgments

Conflicts of Interest

The authors declare no conflict of interest.

References

1   Chen, L., Si, Y., Guo, Z., & Liu, W. (2017). Superhydrophobic sand: a hope for desert water storage and transportation projects. *Journal of Materials Chemistry A*, 5(14), 6416–6423. http://dx.doi.org/10.1039/C7TA00962C

2   Zhang, C., Long, X., Tang, X., Lekomtsev, A., & Korobov, G. Y. (2021). Implementation of water treatment processes to optimize the water saving in chemically enhanced oil recovery and hydraulic fracturing methods. *Energy Reports*, 7, 1720–1727. https://doi.org/10.1016/j.egyr.2021.03.027

3   Chen, W., Wang, W., Luong, D.X., Li, J.T., Granja, V., Advincula, P.A., ... & Tour, J.M. (2022). Robust superhydrophobic surfaces via the sand-in method. *ACS Applied Materials & Interfaces*, 14(30), 35053–35063. https://doi.org/10.1021/acsami.2c05076

4   Austad, T. (2013). Water-based EOR in carbonates and sandstones: new chemical understanding of the EOR potential using "smart water". In *Enhanced oil recovery Field case studies* (pp. 301–335). Gulf Professional Publishing. https://doi.org/10.1016/B978-0-12-386545-8.00013-0

5   Fakhru'l-Razi, A., Pendashteh, A., Abdullah, L. C., Biak, D. R. A., Madaeni, S. S., & Abidin, Z. Z. (2009). Review of technologies for oil and gas produced water treatment. *Journal of hazardous materials*, 170(2-3), 530–551. https://doi.org/10.1016/j.jhazmat.2009.05.044

6   Liu, S., Cai, T., Shen, X., Huang, E., Wang, Z., & Sun, Q. (2019). Superhydrophobic sand with multifunctionalities by TiO_2-incorporated mussel-inspired polydopamine. *Ceramics International*, 45(17), 21263–21269. https://doi.org/10.1016/j.ceramint.2019.07.108

7   Wang, H., Wang, D.T., Zhang, X.Y., & Zhang, Z.Z. (2021). Modified PDMS with inserted hydrophilic particles for water harvesting. *Composites Science and Technology*, 213, 108954. https://doi.org/10.1016/j.compscitech.2021.108954

8   Tajmiri, M., & Ehsani, M. R. (2017). Water Saving by using Nanoparticles in Heavy Oil Reservoir through Thermal EOR Method: Special Pertaining to ZnO & CuO. *Ambient Sci*, 4, 7–12. https://dx.doi.org/10.21276/ambi.2017.04.1.ga02

9   Nueraji, M., Toktarbay, Z., Ardakkyzy, A., Sridhar, D., Algadi, H., Xu, B. B., ... & Guo, Z. (2023). Mechanically-robust electrospun nanocomposite fiber membranes for oil and water separation. *Environmental Research*, 220, 115212. https://doi.org/10.1016/j.envres.2023.115212

10   Zhao, X., Abutalip, M., Afroz, K., & Nuraje, N. (2018). Hydrophobically modified polycarboxybetaine: From living radical polymerization to self-assembly. *Langmuir*, 35(5), 1606–1612. https://doi.org/10.1021/acs.langmuir.8b03561

11   Abutalip, M., Mahmood, A., Rakhmetullayeva, R., Shakhvorostov, A., Dauletov, Y., Kudaibergenov, S., & Nuraje, N. (2019). Reversible Addition? Fragmentation Chain-Transfer Polymerization of Amphiphilic Polycarboxybetaines and Their Molecular Interactions. *Langmuir*, 35(25), 8389–8397. https://doi.org/10.1021/acs.langmuir.9b01347

12   Mollahosseini, A., Abdelrasoul, A., & Shoker, A. (2020). Latest advances in zwitterionic structures modified dialysis membranes. *Materials Today Chemistry*, 15, 100227. https://doi.org/10.1016/j.mtchem.2019.100227

13   Wu, B., Wang, N., Lei, J.H., Shen, Y., & An, Q.F. (2022). Intensification of mass transfer for zwitterionic amine monomers in interfacial polymerization to fabricate monovalent salt/antibiotics separation membrane. *Journal of Membrane Science*, 643, 120050. https://doi.org/10.1016/j.memsci.2021.120050

14   Deng, L., Li, S., Qin, Y., Zhang, L., Chen, H., Chang, Z., & Hu, Y. (2021). Fabrication of antifouling thin-film composite nanofiltration membrane via surface grafting of polyethyleneimine followed by zwitterionic modification. *Journal of Membrane Science*, 619, 118564. https://doi.org/10.1016/j.memsci.2020.118564

15 Lounder, S.J., & Asatekin, A. (2021). Zwitterionic ion-selective membranes with tunable subnanometer pores and excellent fouling resistance. *Chemistry of Materials*, *33*(12), 4408–4416. https://doi.org/10.1021/acs.chemmater.1c00374

16 Lau, S.K., & Yong, W.F. (2021). Recent progress of zwitterionic materials as antifouling membranes for ultrafiltration, nanofiltration, and reverse osmosis. *ACS Applied Polymer Materials*, *3*(9), 4390–4412. https://doi.org/10.1021/acsapm.1c00779

17 Zhang, Y., Song, Q., Liang, X., Wang, J., Jiang, Y., & Liu, J. (2020). High-flux, high-selectivity loose nanofiltration membrane mixed with zwitterionic functionalized silica for dye/salt separation. *Applied Surface Science*, *515*, 146005. https://doi.org/10.1016/j.apsusc.2020.14600

18 Pejman, M., Dadashi Firouzjaei, M., Aghapour Aktij, S., Das, P., Zolghadr, E., Jafarian, H., ... & Tiraferri, A. (2020). In situ Ag-MOF growth on pre-grafted zwitterions imparts outstanding antifouling properties to forward osmosis membranes. *ACS applied materials & interfaces*, *12*(32), 36287–36300. https://doi.org/10.1021/acsami.0c12141

19 Wu, W., Hong, X., Fan, J., Wei, Y., & Wang, H. (2023). Research progress on the substrate for metal–organic framework (MOF) membrane growth for separation. *Chinese Journal of Chemical Engineering*, *56*, 299–313. https://doi.org/10.1016/j.cjche.2022.08.008

20 Li, S., Han, W., An, Q. F., Yong, K. T., & Yin, M. J. (2023). Defect Engineering of MOF-Based Membrane for Gas Separation. *Advanced Functional Materials*, 2303447. https://doi.org/10.1002/adfm.202303447

21 Chen, C., Fei, L., Wang, B., Xu, J., Li, B., Shen, L., & Lin, H. (2023). MOF-Based Photocatalytic Membrane for Water Purification: A Review. *Small*, 2305066. https://doi.org/10.1002/smll.202305066

22 Cao, Z., Zhang, H., Song, B., Xiong, D., Tao, S., Deng, W., ... & Ji, X. (2023). Angstrom-Level Ionic Sieve 2D-MOF Membrane for High Power Aqueous Zinc Anode. *Advanced Functional Materials*, 2300339. https://doi.org/10.1002/adfm.202300339

23 Xu, Y., Zhao, X., Chang, R., Qu, H., Xu, J., & Ma, J. (2022). Designing heterogeneous MOF-on-MOF membrane with hierarchical pores for effective water treatment. *Journal of Membrane Science*, *658*, 120737. https://doi.org/10.1016/j.memsci.2022.120737

24 Gouthaman, A., Azarudeen, R. S., Gnanaprakasam, A., Sivakumar, V. M., & Thirumarimurugan, M. (2018). Polymeric nanocomposites for the removal of Acid red 52 dye from aqueous solutions: Synthesis, characterization, kinetic and isotherm studies. *Ecotoxicology and environmental safety*, *160*, 42–51. https://doi.org/10.1016/j

25 Modi, A., Jiang, Z., & Kasher, R. (2022). Hydrostable ZIF-8 layer on polyacrylonitrile membrane for efficient treatment of oilfield produced water. *Chemical Engineering Journal*, *434*, 133513. https://doi.org/10.1016/j.cej.2021.133513

Article

UDC 541.64

https://doi.org/10.31489/2959-0663/1-24-6

Nazgul A. Yessentayeva* ⓘ, Aldana R. Galiyeva ⓘ, Arailym T. Daribay ⓘ, Daniyar T. Sadyrbekov ⓘ, Tolkyn S. Zhumagalieva ⓘ, Dias T. Marsel ⓘ

Karaganda Buketov University, Karaganda, Kazakhstan
(*Corresponding author's e-mail: naz.yessentayeva92@gmail.com)

Synthesis and Optimization of Bovine Serum Albumin Nanoparticles Immobilized with Antituberculosis Drugs

This study involved the synthesis of bovine serum albumin (BSA) nanoparticles immobilized with the antituberculosis drugs isoniazid (INH) and rifampicin (RIF) by the desolvation method. The primary objective was to explore the impact of varying concentrations of albumin, urea, cysteine, rifampicin, and isoniazid on the average size of nanoparticles, polydispersity, and the encapsulation efficiency of drugs. The study's outcomes affirm that alterations in the concentrations of these components influence nanoparticles' parameters, highlighting their key role in optimizing the encapsulation process and enhancing the efficacy of tuberculosis drug delivery. The nanoparticles obtaned as a result of optimization demonstrated an optimal size of 231.2±1.2 nm with a polydispersity of 0.061±0.08. Encapsulation efficiency was 89% for rifampicin and 38.5% for isoniazid. The investigation of drug release kinetics from the polymer matrix revealed a gradual release pattern. Evaluation of the obtained nanoparticles by Fourier-transform infrared spectroscopy (FTIR), thermogravimetric analysis (TGA), and differential scanning calorimetry (DSC) confirmed the successful incorporation of drugs into the polymer matrix. These findings highlight the potential of BSA nanoparticles as effective carriers for tuberculosis treatment, with implications for refining drug delivery strategies.

Keywords: nanoparticles, bovine serum albumin, rifampicin, isoniazid, desolvation, hydrophilic drugs, hydrophobic drugs, anti-tuberculosis drugs.

Introduction

Addressing tuberculosis remains a considerable medical hindrance, considering its persistent threat to human health, especially in regions with a high incidence of the disease. Millions of people are diagnosed with tuberculosis annually, and the development of effective treatment methods remains a pressing task [1]. However, successful tuberculosis treatment requires precise dosing and prolonged use of medications, often accompanied by side effects and low treatment adherence. In this regard, innovative strategies for delivering antituberculosis drugs have become a priority. Furthermore, the increasing resistance of microorganisms to existing antituberculosis medications emphasizes the urgent need to explore new approaches to combat the infection [2–4].

Overcoming resistance to antituberculosis drugs is a critically important task in the fight against tuberculosis, especially when there is multidrug-resistant (MDR) and extensively drug-resistant (XDR) strains. One of the methods that can help to overcome resistance to antituberculosis drugs is the use of drug combinations, as well as the use of nanoparticles as carriers for antituberculosis drugs. This approach has the potential to enhance their effectiveness and facilitate penetration into Mycobacterium tuberculosis [5, 6].

Taking this into account, bovine serum albumin (BSA) can be identified as a promising material for the synthesis of nanoparticles serving as drug carriers. Bovine serum albumin, a protein extracted from bovine serum, possesses a significant potential for creating nanoparticles that can act as carriers for antituberculosis drugs [7]. The immobilization of antituberculosis drugs such as rifampicin and isoniazid into nanoparticles based on bovine serum albumin represents a prospective approach to enhance the delivery and effectiveness of medications in tuberculosis treatment. Rifampicin and isoniazid (Fig. 1) are widely used in combination for tuberculosis treatment. Their combination can increase efficacy and reduce the probability of drug resistance development among disease-causing agents. Immobilizing both drugs into nanoparticles based on albumin can provide a synergistic effect and optimize treatment [8, 9].

Isoniazid   *Rifampicin*
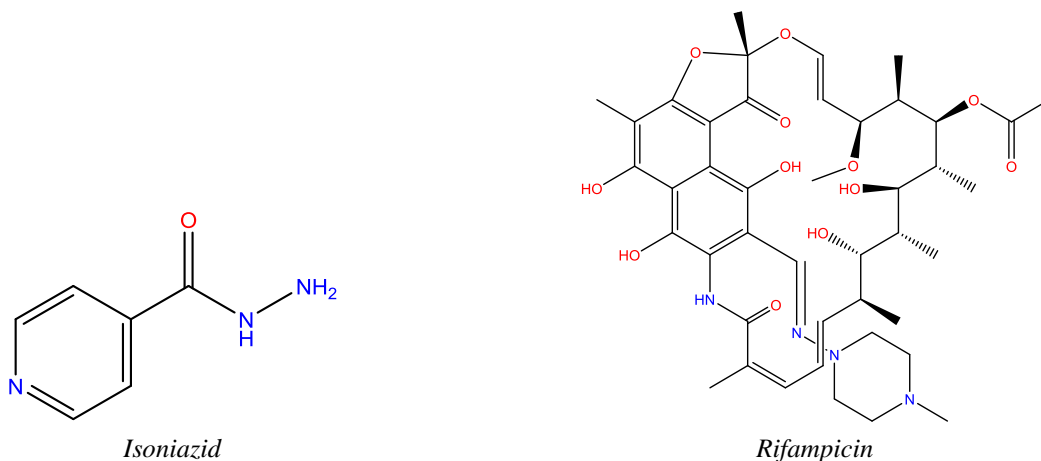
Figure 1. Chemical Structure of antituberculosis drugs

The aim of this study is the creation and optimization of nanoparticles based on bovine serum albumin (BSA), immobilized with rifampicin (RIF) and isoniazid (INH). Thus, in this work, we investigated for the first time the influence of technological parameters on the characteristics of particles (average size, polydispersity) of BSA nanoparticles loaded with rifampicin and isoniazid (BSA-RIF-INH NPs), as well as on the production efficiency (binding efficiency and yield). Furthermore, the physicochemical characteristics of the obtained nanoparticles and the in vitro drug release profile from the polymer matrix were examined.

Experimental

Materials

Bovine serum albumin (lyophilized powder, 98 %) (BSA) was purchased from Sigma Aldrich, Urea (99.5 %) was obtained from ChemPriborSPb (St. Petersburg, Russia), L-cysteine (98.5 %) and Isoniazid (99 %) (INH) was acquired from Sigma Aldrich, Ethanol was received from DosFarm (Almaty, Kazakhstan), Rifampicin (Sigma Aldrich), Potassium dihydrophosphate and sodium hydrophosphate were used to prepare a phosphate-buffered saline solution.

Preparation of INH and RIF loaded BSA NPs

BSA nanoparticles loaded with INH and RIF were prepared using a modified desolvation method, as described previously [6, 10]. In summary, aqueous solution of BSA with required concentration was prepared by dissolving BSA powder in 3 mL of distilled water (pH 7.4) on magnetic stirrer at 200 rpm. After that, 0.5 mL of a urea solution was introduced into the BSA solution, and the mixture was then sonicated for 3 minutes. Because RIF exhibits minimal solubility in water, it was incorporated by dissolving it in a mixture of DMSO and water (volume concentration of DMSO was 20 %) along with INH. Subsequently, the resulting mixture was introduced into the original BSA-Urea solution. Then, ethanol was gradually incorporated into the solution at a rate of 1 mL/min, with continuous stirring (at 200 rpm, at room temperature), until achieving a turbid dispersion. This turbidity signified the formation of BSA nanoparticles containing INH and RIF. Finally, 3 mL of a L-cysteine solution was added. The stirring process persisted for a duration of two hours, after which the resultant nanoparticles were isolated through centrifugation (MiniSpin, Eppendorf, Hamburg, Germany) at 14 000 rpm for 30 minutes. This was followed by a two-step washing procedure using distilled water to clean the nanoparticles from residual ethanol and drugs not encapsulated within the BSA.

Particle size, polydispersity index of the BSA-RIF-INH NPs'

The size of the nanoparticles (diameter) and their distribution (polydispersity index) were assessed using dynamic light scattering (DLS) with a laser-based particle size detector (Malvern Zetasizer Nano S90, Malvern Instruments Ltd., Malvern, UK). Obtained colloidal suspension was diluted with distilled water and the average size and PDI measurement was carried out. The measurements were provided three times at 25 °C, and results were presented as an average value ± standard deviation.

Encapsulation efficiency and BSA-RIF-INH NPs' yield

After centrifugation and rinsing the nanoparticles the supernatant was collected and analyzed using high-performance liquid chromatography (HPLC) with a Shimadzu LC-20 Prominence instrument, with the aim of quantifing the mass of rifampicin and isoniazid that remained unencapsulated in BSA nanoparticles. The encapsulation efficiency and nanoparticles' yield were then determined using the formulas given below:

$$\text{Encapsulation efficiency}\,(\%) = \frac{\text{Total mass of drug} - \text{mass of free drug}}{\text{Total mass of drug}} \times 100\,\%$$

$$\text{Nanoparticles Yield}\,(\%) = \frac{\text{Total mass of NPs}}{\text{Total mass of INH} + \text{Total mass of RIF} + \text{Total mass of BSA}} \times 100\,\%$$

In vitro release of RIF and INH from polymer NPs

The release characteristic of rifampicin and isoniazid from BSA nanoparticles was studied in phosphate-buffered saline (PBS, pH 7.4). Briefly, 24 mg of RIF-INH-BSA NPs were dissolved in 14 mL PBS with pH 7.4 and were incubated at 37 °C under constant stirring (200 rpm). At certain intervals, which were equal to 15 min, 30 min, 1, 2, 4, 8 and 24 h, 1 mL of sample was collected and centrifuged, following HPLC analysis to identify the concentration of released drug. The amount of released RIF and INH was calculated using the following formula:

$$\text{Drug release}\,(\%) = \frac{\text{Mass of drug}\,(\text{INH or RIF})\,\text{released}}{\text{Mass of the total drug}\,(\text{INH or RIF})\,\text{in nanoparticles}} \times 100\,\%$$

Thermogravimetric analysis and differential scanning calorimetry

The thermal decomposition properties of BSA-RIF-INH nanoparticles were examined through thermogravimetric analysis and differential scanning calorimetry (LabSYS evo TGA/DTA/DSC, Setaram, France). The investigation was conducted employing a simultaneous approach involving thermogravimetry and differential scanning calorimetry. A quantity of 10 milligrams of the sample was employed for the analysis. The study was carried out in an open crucible, since the primary methodology was focused on thermal stability. In the differential scanning calorimetry area, the second crucible was intentionally left empty. The estimation was made under a nitrogen atmosphere with a flow rate of 30 mL/min, and the temperature was increased at a rate of 10 °C/min, covering a range from 30 °C to 600 °C.

Study of prepared nanoparticles by infrared spectroscopy

Infrared spectroscopy (FSM 1202, Infraspek Ltd., Russia) was used to identify the samples. The FTIR spectra were obtained by the KBr method, which involves creating a pellet by mixing 3 mg of the sample with 100 mg of KBr. The analyzed IR range extended from 4000 to 400 cm^{-1}.

Statistical Analysis

Experiments were carried out in triplicate, and the findings are presented as the mean values along with their respective standard deviations (SD). Statistical evaluations were carried out employing the Student's t-test through Statistica 12 (TIBCO Software Inc., Palo Alto, CA, USA). A significance threshold of 0.05 was employed to ascertain statistical significance.

Results and discussion

In previous studies, the possibility of obtaining stable BSA nanoparticles by the synergistic interaction of urea and L-cysteine with the protein, including the immobilization of isoniazid, has been demonstrated [6]. Within the scope of this research, the potential for obtaining BSA nanoparticles using biocompatible components and immobilizing antituberculosis drugs — isoniazid and rifampicin — will be explored. BSA nanoparticles were obtained sequentially using the desolvation method with urea and cysteine, and the immobilization of drugs was carried out using the encapsulation method. Schematic representation of preparation method of BSA-RIF-INH nanoparticles is presented in Figure 2.
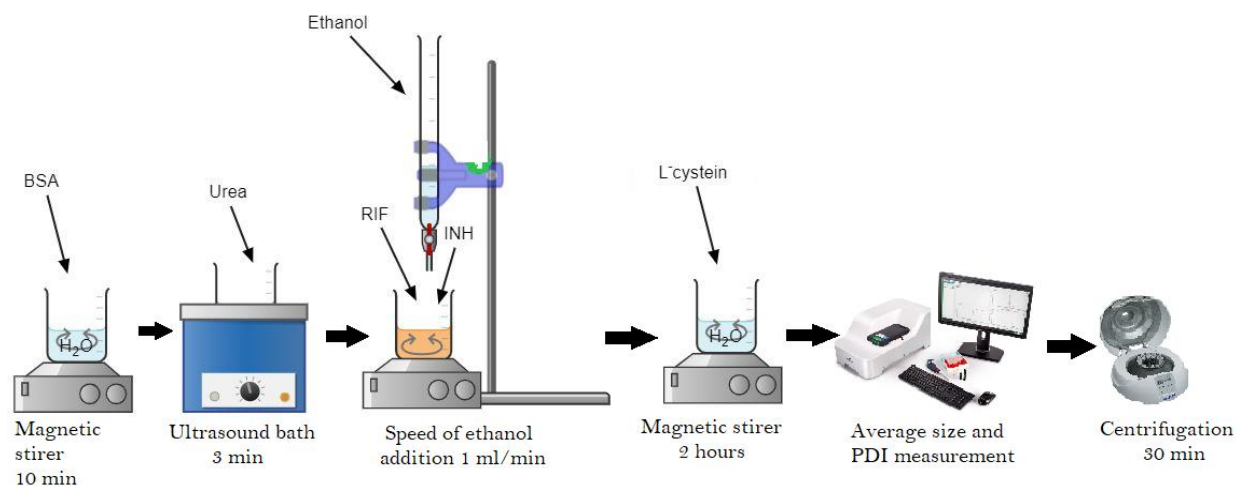
Figure 2. Schematic representation of preparation method of BSA-RIF-INH nanoparticles

Study the effect of urea and L-cysteine on NP characteristics

Urea is a chaotropic agent, aiding in the disruption of hydrophobic interactions within the protein, thereby enhancing its solubility [11]. The urea concentration affects such characteristics of nanoparticles as size, shape and dispersity. To investigate the effect of urea on nanoparticles' characteristics, the nanoparticles were synthesized under the following conditions (standard conditions): BSA concentration 60 mg/mL; L-cysteine concentration 1 mg/mL; pH 7.4; RIF and INH concentrations of 10 mg/mL each, respectively, with ethanol as the desolvating agent. The prepared nanoparticles were characterized using photon correlation spectroscopy (Fig. 3).
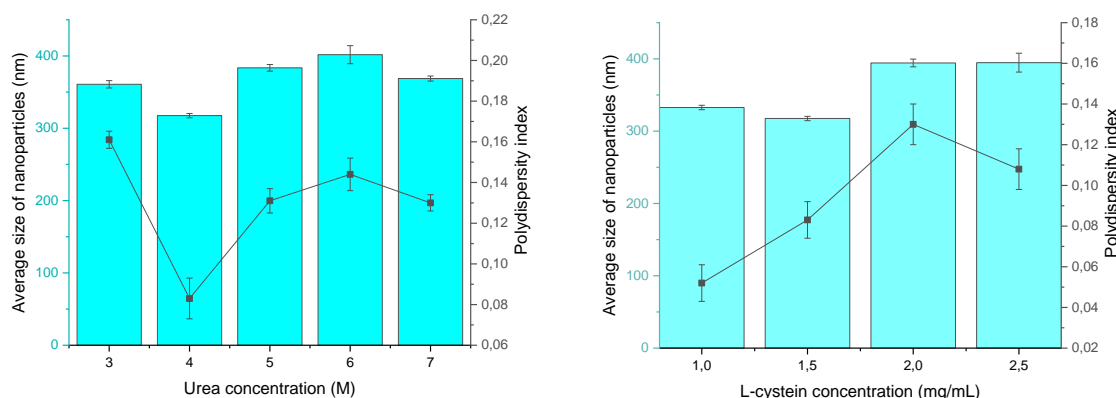
Figure 3. Influence of urea and L-cysteine on the average size and polydispersity of nanoparticles

The graph reveals a trend where the average nanoparticle size initially increases as the urea concentration rises from 4 M to 6 M. This phenomenon is likely associated with particle aggregation at higher urea concentrations. The smallest average nanoparticle size (317.5±3) and the lowest polydispersity (0.083±0.010) are achieved at a urea concentration of 4 M.

The use of L-cysteine in albumin nanoparticles for thiol-disulfide exchange represents an innovative method that can find applications in various fields, including medicine and biotechnology [7]. Cysteine contains a thiol functional group (-SH) capable of forming disulfide bonds (-S-S-) with other thiol molecules. This process can be used to control the delivery and release of drugs. The thiol groups of cysteine react with the disulfide bridges which present in the structure of albumin, ensuring a robust immobilization of drugs [7, 12]. Figure 3 illustrates the results of the impact of L-cysteine on the characteristics of BSA-RIF-INH nanoparticles.

With an increase in cysteine concentration from 1.5 to 2.5 mg/mL, the average size of nanoparticles increases from 317.47±3 nm to 394.7±13 nm. Additionally, the polydispersity index increases with the rise of the concentration of cysteine. The observed phenomenon might be attributed with the excess of L-cysteine,

which induces a reduction in the intermolecular S-S bridges that are formed. This, in turn, disrupts the evolving three-dimensional gel-like structure of albumin. As a consequence, larger particles may unfold, leading to an increase in both the formation of macrostructures and the values of the dispersion index [7].

Study the effect of albumin concentration on NP characteristics

Different concentrations of BSA (10, 20, 40, 60, and 80 mg/mL) were used during the nanoparticles' synthesis to investigate its influence on the characteristics of BSA nanoparticles and determine the optimal concentration of BSA. Table 1 illustrates the effect of polymer concentration on the size and encapsulation efficiency of nanoparticles loaded with RIF and INH at a urea concentration of 4 M and cysteine concentration of 1 mg/mL.

T a b l e 1

Effect of the BSA concentration on nanoparticle size, PDI, encapsulation efficiency and yield

BSA concentration (mg/mL)	Average size of nanoparticles (d, nm)	PDI	Encapsulation efficiency (%)		Yield (%)
			Rifampicin	Isoniazid	
20	164.5±0.9	0.098±0.021	67±4	43±3	17±3
40	194.2±2.1	0.122±0.019	67±2	37±2	15±4
60	214.8±1.7	0.139±0.016	70±4	50±3	36±4
80	339.5±1.1	0.159±0.013	69±2	44±3	31±2

The nanoparticle size increases from 164.5±0.9 to 339.5±1.1 nm, and the drug content percentage rises from 67±4 to 70±4 % for rifampicin and from 37±2 to 50±3 % for isoniazid as the albumin concentration increases from 10 to 80 mg/mL. The obtained results indicate that the polymer concentration predominantly influences the size and drug binding efficiency of the loaded nanoparticles. Polymer concentration is a key factor affecting the nanoparticle characteristics. Higher polymer concentration increases the average size and encapsulation efficiency, consistent with the findings of many other studies [13]. An increase in polymer concentration causes a rise in the viscosity of the dispersed phase, leading to the formation of larger droplets and a deceleration in the diffusion rate of BSA into the surrounding aqueous phase. Thus, the viscosity of the polymer solution significantly influences the nanoparticle size. A polymer concentration of 60 mg/mL provided the highest yield of nanoparticles — 36±4%.

Study the effect of anti-tuberculosis drugs concentration on the formation of nanoparticles (NPs)

Investigating the effect of drug concentration in the polymer matrix on the average size is a crucial aspect of drug carrier development. Rifampicin and isoniazid, serving as representative bioactive compounds, were immobilized into BSA nanoparticles. The immobilization process involved their incorporation in the synthesis of BSA nanoparticles, which were effectively formed using natural cross-linking agents like albumin, urea, and L-cysteine. The concentration of the drugs ranged from 2 to 10 mg/mL, and the outcomes are outlined in Table 2.

T a b l e 2

Effect of the concentration of rifampicin on nanoparticles' size, PDI, encapsulation efficiency and yield

Rifampicin concentration (mg/mL)	Average size of nanoparticles (d. nm)	PDI	Encapsulation efficiency of Rifampicin (%)	Yield (%)
2	106.3±1.1	0.380±0.008	86±3	3±2
4	161.7±0.9	0.173±0.014	88±5	13±4
6	254.3±1.5	0.110±0.044	92±5	41±5
8	381.6±1.4	0.240±0.009	91±2	55±2
10	317.5±3.1	0.083±0.010	81±2	51±3

The results presented in Table 2 indicate a significant influence of the drug concentration on the key characteristics of the system. The research results reveal that changes in rifampicin concentration lead to variations in the average particle size. Thus, with an increase in rifampicin concentration, the average particle size increases from 106.3±1.1 to 381.6±1.4 nm. The highest degree of binding was observed at a drug content of 6 mg/mL, reaching 92±5 %.

Table 3 presents the particle sizes and the degree of binding of nanoparticles loaded with anti-tuberculosis drugs prepared with different concentrations of isoniazid (2, 4, 6, 8, and 10 mg/mL).

As reflected in Table 3, increasing the concentration of isoniazid significantly affected the particle size and the encapsulation efficiency of the drug. As the concentration of isoniazid increases the average particle size decreased from 179.9±1.1 % to 161.7±0.9 nm. This trend confirms that the concentration of isoniazid directly influences the particle size, leading to their reduction in agreement with the results observed by Tazhbayev Y. and Galiyeva A. [10]. Moreover, the encapsulation efficiency of isoniazid increased with its concentration, reaching 40±5 % at a concentration of 10 mg/mL. These results highlight the importance of optimizing the isoniazid concentration to achieve the desired physicochemical characteristics of nanoparticles and ensure effective binding to the carrier.

T a b l e 3

Effect of the isoniazid concentration on nanoparticles' size, PDI, encapsulation efficiency and yield

Isoniazid concentration (mg/mL)	Average size of nanoparticles (d. nm)	PDI	Encapsulation efficiency of Isoniazid (%)	Yield (%)
2	179.9±1.1	0.125±0.010	32±4	14±4
4	175.3±1.4	0.139±0.007	30±2	12±5
6	172.2±1.6	0.197±0.008	39±2	8±1
8	164.5±0.8	0.152±0.016	39±3	12±4
10	161.7±0.9	0.173±0.014	40±5	13±3

The recommended strategy involves the production of particles with a size below 300 nm, as this offers favorable pharmacological traits, prolonged circulation kinetics, and a gradual release specifically in targeted regions. Throughout this investigation, a thorough exploration of the impact of reagent concentrations on BSA-RIF-INH NPs properties was conducted. Following optimization, the ideal parameters were identified: BSA — 60 mg/mL, urea — 4 M, L-cysteine — 1.5 mg/mL, isoniazid — 10 mg/mL, rifampicin — 6 mg/mL. BSA-RIF-INH NPs exhibited an average size of 231.2±1.2 nm with a polydispersity of 0.061±0.08 (Fig. 4). Successful completion of the encapsulation process was confirmed by obtaining noteworthy encapsulation efficiency (89 % for rifampicin and 38.5 % for isoniazid).
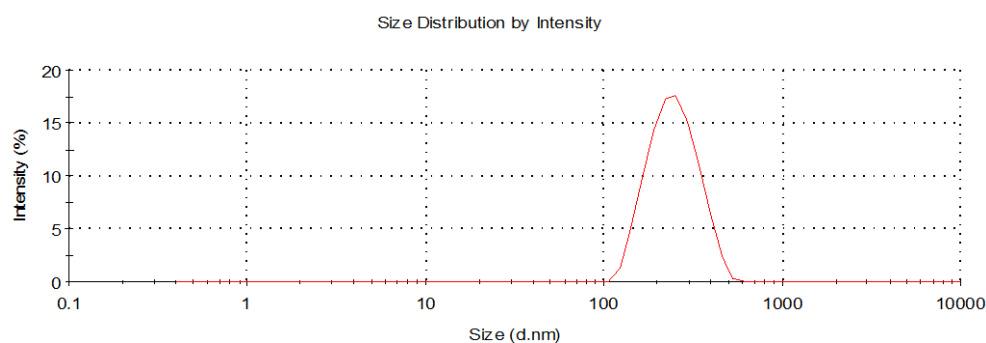
Figure 4. Particle size of optimized BSA-RIF-INH nanoparticles determined by photon correlation spectroscopy

To validate the encapsulation of the rifampicin and isoniazid into the BSA NPs, thermogravimetric analysis (TGA) and differential scanning calorimetry (DSC) were conducted. Thermograms of these drugs, BSA NPs and BSA-RIF-INH NPs are illustrated in Figure 5.

According to the graph, rifampicin, as polymorph I, remains thermally stable up to 230 °C. Its thermal decomposition process takes place in two stages [10, 15]. At the first stage, which occurs between 230–285 °C, there is a sharp mass loss of 22 %. Then during the second stage, in the interval 285–617 °C, the mass of RIF decreases more smoothly for 28 %. The distinct endothermic peak for isoniazid is detected at 175.6 °C, which corresponds to the melting point, since the mass of INH remains unchanged. The decomposition of this drug occurs between 257 °C and 445 °C, with a 75 % reduction in INH mass [10, 14]. Three endothermic peaks at 94.4, 245.8 and 390.7 °C are noted on the DSC curve for BSA NP. Considering that the albumin molecule has three different domains [6, 16], its thermal denaturation on the TGA curve presents three characteristic transitions, the mass loss at the end of all stages of decomposition equals to 82 %. Endo-

thermic peaks for BSA-RIF-INH NPs are detected at 92.9, 224 and 361.5 °C, which corresponds to the decrease of NPs' mass in the TGA curve; the mass loss is 44 %. Nevertheless, a noticeable displacement of peaks to lower temperature range is noticed in contrast to the curves of empty BSA NPs. This could be attributed to the influence of medications.
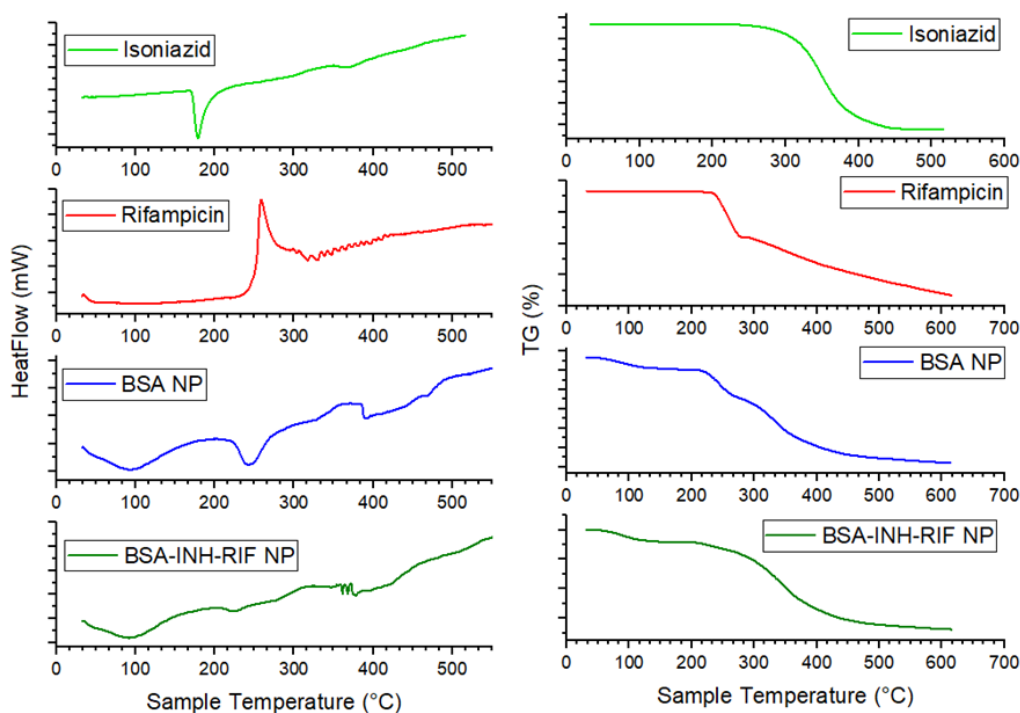
Figure 5. Differential scanning calorimetry and thermogravimetric analysis
of Rifampicin, Isoniazid, BSA NPs, BSA-INH-RIF NPs

FT-IR spectra were obtained for BSA nanoparticles, BSA-RIF-INH nanoparticles, rifampicin and isoniazid, as depicted in Figure 6. These spectra reveal distinct bands corresponding to specific wavenumbers, identifying characteristic features of the original albumin. Significantly, key peaks include 3418 cm^{-1} is indicative of the A-amide group linked to N–H, while the following prominent peak at 2824 cm^{-1} identifies the B-amide group associated with free ion. The peak at 1489 cm^{-1} represents Amide II, indicating C–N stretching and N–H bending vibrations. Amide I, linked to the C–O bond, is denoted by the peak at 1620 cm^{-1}, and the presence of CH$_2$ groups is evident at 1392 cm^{-1}. Additionally, the observation of amide III at around 1335 cm^{-1} is associated with –C–N– group stretching and N–H bending vibrations [6; 7].
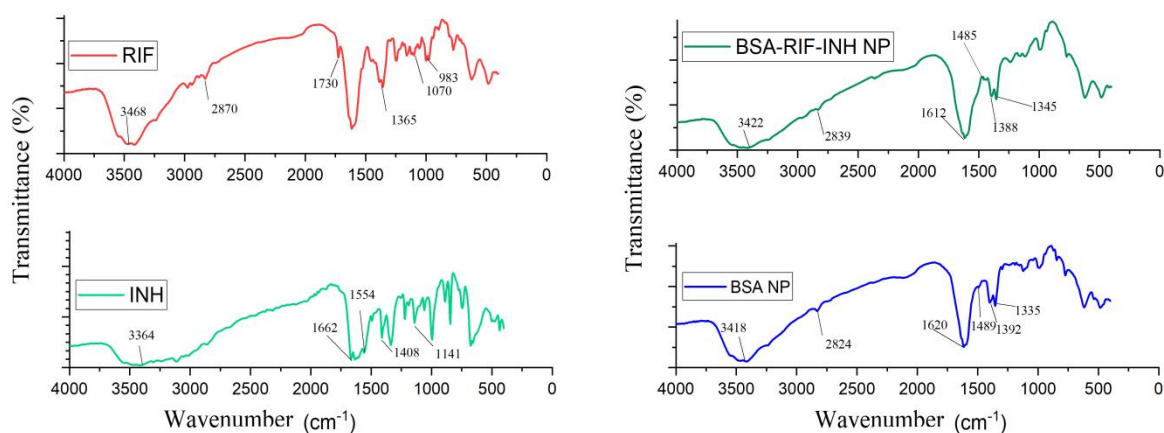
Figure 6. FT-IR spectra of the isoniazid, rifampicin, BSA NPs and BSA nanoparticles
immobilized with rifampicin and isoniazid

In case of rifampicin, significant absorption features are observable: a distinct peak at 983 cm^{-1} denotes ≡C-H, C-H bond, 1070 cm^{-1} is linked to –CH, CO, and C-H, the peak at 1365 cm^{-1} is associated with the CH$_2$ and C=C. The peak at 3468 cm^{-1} connected to NH stretching, 2870 cm^{-1} is linked to the C–H bond, and 1730 cm^{-1} is related to the C=O bond [10, 18, 19]. The FTIR spectrum of isoniazid exhibits clear peaks at different wavenumbers: 3364 cm^{-1} signifies the N-H bond, 1662 cm^{-1} (C=O) is associated with pyridine, 1554 cm^{-1} is related to the –C–N bond, and the peak at 1141 cm^{-1} corresponds to the –N–N amide group [6, 10, 17]. The FTIR spectrum associated with BSA-RIF-INH NPs closely resembled that of the BSA NPs. The absence of distinct peak characteristics for rifampicin and isoniazid in the FTIR spectra of final NPs, concealed by polymer bands, suggests successful embedding of the drugs within the nanoparticles [6, 18].

To validate the sustained effect of the synthesized nanoparticles, it is essential to explore the kinetics of drug release from complexes formed by loading rifampicin and isoniazid into polymers. The release of RIF and INH from produced nanoparticles was studied in phosphate buffer saline (PBS) with a pH of 7.4. The evaluation of RIF and INH release from the nanoparticles was quantified by measuring the concentration of the released drug, as determined using HPLC. The results of this analysis are visually depicted in Figure 7, providing a clear representation of the extent of drug release over time.
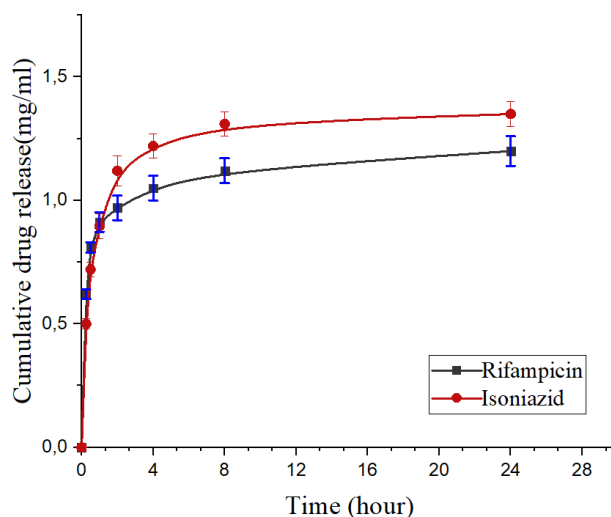
Figure 7. Investigation of INH and RIF release from the polymer matrix in phosphate-buffered saline

The graph illustrated in Figure 7 demonstrates a constant and persistent release of medicines from obtained nanoparticles throughout the entire investigation period of 24 hours. At the end of experiment period the concentrations of RIF and INH equaled to 1,2 and 1,35 mg/mL respectively. This highlights the considerable potential for the prolonged release of isoniazid and rifampicin from albumin nanoparticles. The investigation of release kinetics reveals a minor initial burst effect followed by an extended and gradual release of rifampicin and isoniazid. It could be attributed to the medicine adsorbed on the surface of the BSA-INH-RIF nanoparticles [6, 7], followed by a diffusion process through the polymer matrix of the nanoparticles, consistent with the findings reported by Mandhar, P. and Joshi, G. [20]. Such sustained release capabilities offer the advantage of preventing abrupt spikes in drug concentration in the bloodstream, ensuring therapeutic levels are maintained over an extended period. This highlights the potential of these particles as effective carriers for delivering isoniazid and rifampicin [14, 21, 22].

Conclusion

The effects of urea, L-cysteine, bovine serum albumin, isoniazid and rifampicin concentrations were carefully analyzed in this study. It was found that polymer and rifampicin concentrations had a significant effect on the key characteristics of the nanoparticles. The optimization process produced nanoparticles with desired parameters such as size (231.2±1.2 nm) and polydispersity (0.061±0.08). The degree of drug binding was 89 % for rifampicin and 38.5 % for isoniazid. The results suggest the possibility of sustained drug release both in vitro and in vivo, emphasizing the potential of bovine serum albumin nanoparticles as a promis-

ing carrier for anti-TB drugs. These findings provide important indications for future research and practical applications of this technology in the field of drug delivery.

Funding

Author Information*

———

*The authors' names are presented in the following order: First Name, Middle Name and Last Name

Nazgul Asylbekkyzy Yessentayeva (*corresponding author*) — 2nd year Doctoral Student, Department of Organic Chemistry and Polymers, Karaganda Buketov University, Universitetskaya street, 28, 100024, Karaganda, Kazakhstan.; e-mail: naz.yessentayeva92@gmail.com; https://orcid.org/0000-0003-4820-8460

Aldana Rymzhanovna Galiyeva — Engineer, Institute of Chemical Problems, Karaganda Buketov University, Universitetskaya street, 28, 100024, Karaganda, Kazakhstan; e-mail: aldana_karaganda@mail.ru; https://orcid.org/0000-0002-8551-6297

Arailym Turashkyzy Daribay — Master Student, Karaganda Buketov University, Universitetskaya street, 28, 100024, Karaganda, Kazakhstan; e-mail: arailymdaribay@gmail.com; https://orcid.org/0000-0001-5675-0351

Daniyar Tleuzhanovich Sadyrbekov — Candidate of Chemical Sciences, Researcher, laboratory of the engineering profile "Physical and chemical methods of research", Karaganda Buketov University, Universitetskaya street, 28, 100024, Karaganda, Kazakhstan; e-mail: acidbear@mail.ru; https://orcid.org/0000-0002-3047-9142

Tolkyn Sergaziyevna Zhumagaliyeva — Professor of the Department of Organic Chemistry and Polymers, Karaganda Buketov University, Universitetskaya street, 28, 100024, Karaganda, Kazakhstan; e-mail: zhumagalieva79@mail.ru; https://orcid.org/0000-0003-1765-752X

Dias Temirlanuly Marsel — Master Student, Karaganda Buketov University, Universitetskaya street, 28, 100024, Karaganda, Kazakhstan; e-mail: marsel.dias@bk.ru; https://orcid.org/0000-0002-1204-0814

Author Contributions

The manuscript was written through contributions of all authors. All authors have given approval to the final version of the manuscript. CRediT: **Aldana Rymzhanovna Galiyeva** conceptualization, data curation, methodology; writing — review and editing; **Nazgul Asylbekkyzy Yessentayeva** writing — original draft, writing-review and editing, investigation, data curation: **Tolkyn Sergaziyevna Zhumagaliyeva** data curation, writing — review and editing; **Arailym Turashkyzy Daribay** investigation, resources**; Daniyar Tleuzhanovich Sadyrbekov** investigation; **Dias Temirlanuly Marsel** investigation.

Conflicts of Interest

The authors declare no conflict of interest.

References

1   World Health Organization (2022). *Global Tuberculosis Report.* World Health Organization: Geneva, Switzerland. Licence: CC BY-NC-SA 3.0 IGO. https://www.who.int/teams/global-tuberculosis-programme/tb-reports/global-tuberculosis-report-2022

2   Scior, T., Morales, I.M., Eisele, S.J.G., Domeyer, D., & Laufer, S. (2022). Antitubercular Isoniazid and Drug Resistance of Mycobacterium tuberculosis — A Review. *Arch. Pharm.*, *335*, 511–525. https://doi.org/10.1002/ardp.200290005

3   Narmandakh, E., Tumenbayar, O., Borolzoi, T., Erkhembayar, B., Boldoo, T., Dambaa, N., & Chiang, C.Y. (2020). Genetic Mutations Associated with Isoniazid Resistance in Mycobacterium tuberculosis in Mongolia. *Antimicrobial Agents and Chemotherapy*, *64*(7), Article e00537-20. https://doi.org/10.1128/aac.00537-20

4   Arun, K.B., Madhavan, A., Abraham, B., Balaji, M., Sivakumar, K.C., Nisha, P., & Kumar, R.A. (2021). Acetylation of Isoniazid Is a Novel Mechanism of Isoniazid Resistance in Mycobacterium tuberculosis. *Antimicrobial Agents and Chemotherapy*, *65*(1), Article e00456-20. https://doi.org/10.1128/aac.00456-20

5   Rather, M.A., Amin, S., Maqbool, M., Bhat, Z.S., Gupta, P.N., & Ahmad, Z. (2016). Preparation and In Vitro Characterization of Albumin Nanoparticles Encapsulating an Anti-Tuberculosis Drug-Levofloxacin. *Adv. Sci. Eng. Med.*, *8*, 912–917. https://doi.org/10.1166/asem.2016.1922

6   Tazhbayev, Y., Galiyeva, A., Zhumagaliyeva, T., Burkeyev, M., & Karimova, B. (2021). Isoniazid-Loaded Albumin Nanoparticles: Taguchi Optimization Method. *Polymers*, *13*(21), Article 3808. https://doi.org/10.3390/polym13213808

7   Tazhbayev, Y., Mukashev, O., Burkeyev, M., & Lozinsky, V. I. (2020). Synthesis and Comparative Study of Nanoparticles Derived from Bovine and Human Serum Albumins. *Polymers*, *12*(6), Article 1301. https://doi.org/10.3390/polym12061301

8   Ge, Z.H., Ma, R., Xu, G.X., Chen, Z., Zhang, D.F., Wang, Q., Ma, W. (2018). Development and In Vitro Release of Isoniazid and Rifampicin-Loaded Bovine Serum Albumin Nanoparticles. *Medical Science Monitor*, *24*, 473–478. https://doi.org/10.12659/msm.905581

9   Somasundaram, S., Ram, A., & Sankaranarayanan, L. (2014). Isoniazid and Rifampicin as Therapeutic Regimen in the Current Era: A Review. *J. Tuberc. Res.*, *2*, 40–51. https://doi.org/10.4236/jtr.2014.21005

10   Galiyeva, A., Daribay, A., Zhumagaliyeva, T., Zhaparova, L., Sadyrbekov, D., & Tazhbayev, Y. (2023). Human Serum Albumin Nanoparticles: Synthesis, Optimization and Immobilization with Antituberculosis Drugs. *Polymers*, *15*(13), Article 2774. https://doi.org/10.3390/polym15132774

11   Tazhbayev, Y., Mukashev, O., Burkeev, M., & Kreuter, J. (2019). Hydroxyurea-Loaded Albumin Nanoparticles: Preparation, Characterization, and In Vitro Studies. *Pharmaceutics*, *11*(8), Article 410. https://doi.org/10.3390/pharmaceutics11080410

12   Lomis, N., Westfall, S., Farahdel, L., Malhotra, M., Shum-Tim, D., & Prakash, S. (2016). Human Serum Albumin Nanoparticles for Use in Cancer Drug Delivery: Process Optimization and In Vitro Characterization. *Nanomaterials*, *6*(6), Article 116. https://doi.org/10.3390/nano6060116

13   Chen, X.T., Lv, G.Y., Zhang, J., Tang, S.C., Yan, Y.G., Wu, Z.Y., & Wei, J. (2014). Preparation and properties of BSA-loaded microspheres based on multi-(amino acid) copolymer for protein delivery. *International Journal of Nanomedicine, 9*, 1957–1965. https://doi.org/10.2147/ijn.s57048

14   Galiyeva, A.R., Tazhbayev, Y.M., Zhumagaliyeva, T.S., Sadyrbekov, D.T., Shokenova, S.S., Kaikenov, D.A., & Karimova, B.N. (2022). Polylactide-co-glycolide nanoparticles immobilized with isoniazid: optimization using the experimental Taguchi method. *Bulletin of the University of Karaganda-Chemistry,* (105), 69–77. https://doi.org/10.31489/2022Ch1/69-77

15   Alves, R., Reis, T.V.D., da Silva, L.C.C., Storpírtis, S., Mercuri, L.P., & Matos, J.D. (2010). Thermal behavior and decomposition kinetics of rifampicin polymorphs under isothermal and non-isothermal conditions. *Brazilian Journal of Pharmaceutical Sciences*, *46*(2), 343–351. https://doi.org/10.1590/s1984-82502010000200022

16   Michnik, A., Michalik, K., Kluczewska, A., & Drzazga, Z. (2006). Comparative DSC study of human and bovine serum albumin. *Journal of Thermal Analysis and Calorimetry*, *84*(1), 113–117. https://doi.org/10.1007/s10973-005-7170-1

17   Gunasekaran, S., Sailatha, E., Seshadri, S., & Kumaresan, S. (2009). FTIR, FT Raman spectra and molecular structural confirmation of isoniazid. *Indian Journal of Pure & Applied Physics*, *47*(1), 12–18.

18   Sharma, A., Puri, V., Kumar, P., Singh, I., & Huanbutta, K. (2021). Development and Evaluation of Rifampicin Loaded Alginate-Gelatin Biocomposite Microfibers. *Polymers*, *13*(9), Article 1514. https://doi.org/10.3390/polym13091514

19   Ivashchenko, O., Tomila, T., Ulyanchich, N., Yarmola, T., & Uvarova, I. (2014). Fourier-Transform Infrared Spectroscopy of Antibiotic Loaded Ag-Free and Ag-Doped Hydroxyapatites. *Adv. Sci. Eng. Med.*, *6*, 193–202. https://doi.org/10.1166/asem.2014.1473

20   Mandhar, P. & Joshi, G. (2015). Development of Sustained Release Drug Delivery System: A Review. *Asian Pacific Journal of Health Sciences, 2*(1), 179–185. https://doi.org/10.21276/apjhs.2015.2.1.31

21   Loiko, O.P., Herk, A.M. van, Ali, S.I., Burkeev, M.Z., Tazhbayev, Y.M., & Zhaparova, L.Z. (2013). Controlled release of Capreomycin sulfate from pH responsive nanocapsules. *e-Polymers, 13*(1). https://doi.org/10.1515/epoly-2013-0118

22   Burkeev, M.Z., Zhaparova, L.Z., Tazhbaev, E.M., Zhumagalieva, T.S., Ali, S.I. & van Herk, A.M. (2013). In Vitro Studies of Capreomycin Sulfate Release from Polyethylcyanoacrylate Nanoparticles. *Pharmaceutical Chemistry Journal, 47*(3), 154–156. https://doi.org/10.1007/s11094-013-0916-3

PHYSICAL AND ANALYTICAL CHEMISTRY

Nataliya M. Karaush-Karmazin[1*] , Boris F. Minaev[1, 2*] ,
Valentina A. Minaeva[1] , Olexandr O. Panchenko[1] , Hans Ågren[2]

[1]Department of Chemistry and Nanomaterials Science, Bohdan Khmelnytsky National University, Cherkasy, Ukraine;
[2]Department of Physics and Astronomy, Uppsala University, Uppsala, Sweden
*(*Corresponding authors′ e-mail: karaush22@ukr.net; bfmin43@ukr.net)*

Hirshfeld Surfaces Analysis of Intermolecular Interaction
in the Series of Steroid Hormone Molecular Crystals

In this work Hirshfeld surface analysis is performed on the crystallographic-characterized crystal cells of the progesterone, 17α-hydroxyprogesterone, and testosterone hormones. The Hirshfeld surfaces are mapped for a detailed visualization of the electron density distribution around a molecule to understand the atomic-pair close contacts and interaction types within a crystal structure of the studied hormones. The intermolecular forces, including Van der Waals forces, hydrogen bonding, and C–H⋯π interactions, play essential roles in determining the supramolecular arrangement of all the three molecules in their crystals. These forces contribute to the cohesion, stability, and structural organization of the crystals, ultimately influencing their properties and behaviour in various applications. Two-dimensional fingerprint plots with detailed information about the contribution of each contact to the total Hirschfeld surface allowed to provide a visual representation of the relative importance (in %) of identified intermolecular O⋯H/H⋯O, C⋯H/H⋯C, H⋯H interactions within a crystal structure of the studied hormones in the context of "molecule-substance" relations.

Keywords: sex hormones; progesterone; 17α-hydroxyprogesterone; testosterone; intermolecular interactions; X-ray analysis; Hirshfeld surface analysis; fingerprints; hydrogen bonds.

Introduction

The most studied sex hormones, such as progesterone, 17α-hydroxyprogesterone, and testosterone ensure a stable development and functioning of the human body according to the male or female type. They play a crucial role in the maintenance of the male and female reproductive systems, as well as influencing various physiological processes throughout the human body. The delicate balance of these sex hormones is essential for the proper functioning and development of the human organism. Any level disruption or imbalance can result in various issues, affecting both reproductive and overall health. Hormonal regulation is a complex process involving feedback loops between the brain, gonads, and other endocrine glands. In a biochemical classification, progesterone, 17α-hydroxyprogesterone, and testosterone are steroids, as their structures are based on the cyclopentanoperhydrophenanthrene (sterane) cycle. The steroid nucleus, sterane, comprises three cyclohexane rings (A, B, and C) and one cyclopentane ring D (Fig. 1). This common structural motif imparts distinctive biochemical and physiological properties to the steroids and provide the lipophilicity that enables their traverse of cell membranes. This facilitates their interaction with intracellular receptors, initiating a cascade of events that ultimately modulate gene expression and influence various physiological processes. While these steroids share a common structural foundation, their specific functions and regulatory roles in the body are diverse. This specificity and diversity are determined to some extent by in-

termolecular contacts including local areas of van-der-Waals interactions and low-frequency vibration energy flow [1–4].

Progesterone, a C-21 steroid, plays a crucial role in the female reproductive system. It is the main hormone of pregnancy. The effect of progesterone is realized through its receptors where the C3-keto-group and a double bond between the C4 and C5 carbon atoms of cycle A are important features (Fig. 1) [1–5]. 17α-Hydroxyprogesterone, an intermediate in the synthesis of various steroid hormones, is particularly involved in the production of cortisol and androgens. It serves as a precursor in the biosynthetic pathways that lead to the formation of these important hormones. It differs from progesterone by the presence of an additional hydroxyl radical near the 17th carbon atom in the molecular skeleton (Fig. 1) [5].
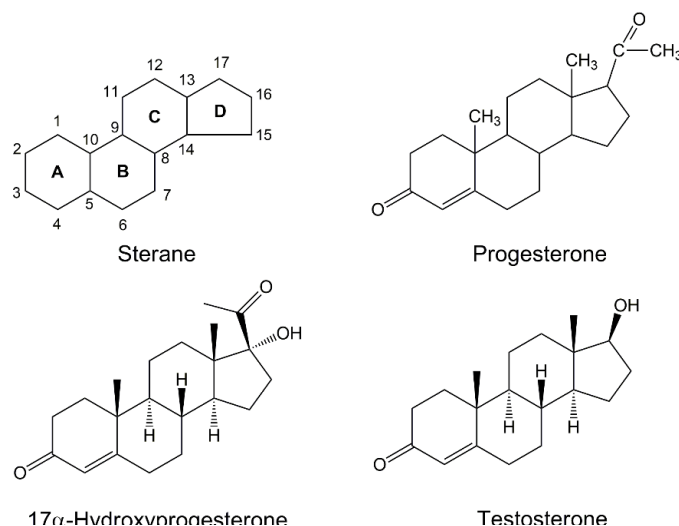
Figure 1. Chemical structures of sterane, progesterone, 17α-hydroxyprogesterone and testosterone

Testosterone, a C-19 steroid and the primary male sex hormone responsible for the development of male sexual characteristics [6–8]. This hormone is from the androstane class containing a ketone and a hydroxyl group at the C3 and C17 positions, respectively. An adult man's testosterone level is 7-8 times higher than that of an adult woman. Because the testosterone levels naturally decline as men age, the synthetic testosterone is sometimes used to counteract testosterone deficiency, and it is also used illegally to improve muscle mass and performance in athletes, a practice known as doping. The World Anti-Doping Agency (WADA) included it in the S1 Schedule of anabolic agents.

Analysis of the structure and spectral characteristics of hormones is important for gaining insights into the specificity of their interactions with corresponding receptors [4]. Quantum-chemical calculations of the geometry, electronic structure, and Raman spectrum of the progesterone molecule are presented in Ref. [9]. Intermolecular interactions are important for the formation of crystal packing, molecular recognition, and the formation of supramolecular structures [10]. Intermolecular interactions in crystals of progesterone, 17α-hydroxyprogesterone, and testosterone were investigated based on Kohn-Sham orbitals using Bader's topological theory [11]. To analyze the function of the electron density distribution, an additive scheme of breaking the crystal packing of hormones into six dimer pairs was used. Analysis of the electron density distribution function in progesterone, 17α-hydroxyprogesterone, and testosterone dimers revealed several hydrogen bonds O···H and non-valent bonds H···H, C···H, which stabilize the spatial structure of dimers. The total energy of all non-valent intermolecular bonds in the 17α-hydroxyprogesterone tetramer is equal to −19.78 kcal/mol, which significantly exceeds the energy of the crystal packing of progesterone (−9.67 kcal/mol) and testosterone (−10.62 kcal/mol) [12]. A drawback of the technique used in Ref. [9] is that it neglects the influence of neighbouring molecules on the electron density distribution in a particular dimer.

In this study, the analysis of intermolecular interactions in the crystal packings of progesterone, 17α-hydroxyprogesterone, and testosterone was carried out using the Hirshfeld surface method, which has been widely used in recent years as a means to quantify and visualize various types of intermolecular interactions in molecular crystals [13–17]. Analysis of the three-dimensional (3D) Hirschfeld surfaces and two-dimensional (2D) fingerprint plots provides details of the packing behaviour of molecular crystals and allow

us to determine the contribution of each type of non-valence links to the overall Hirschfeld surface of all intermolecular interactions in the crystal cell of the corresponding hormone.

Computational Details

Hirschfeld surface (HS) analysis was performed using CIF files of the X-ray structures of progesterone, 17α-hydroxyprogesterone, and testosterone. The studied hormones have an orthorhombic crystal packing and belong to the $P2_12_12_1$ symmetry space group [18–21]. Crystal packing parameters for the studied hormones were taken from crystallographic data deposited in the Cambridge Crystallographic Data Centre with the corresponding CCDC deposition numbers: 228768 (progesterone), 1178343 (17α-hydroxyprogesterone), 1269495 (testosterone).

The method of Hirschfeld surfaces is implemented in the CrystalExplorer 21.5 software package with a very high resolution [22, 23]. The analysis is visualized by the normalized contact distance (d_{norm}), which is defined in terms of d_e (the nearest external distance), d_i (the nearest internal distance), and the van der Waals (vdW) radii of the two atoms on the surface, and is calculated by the following equation [17]:

$$d_{norm} = \frac{d_i - r_i^{vdW}}{r_i^{vdW}} + \frac{d_e - r_e^{vdW}}{r_e^{vdW}},$$

where r_i^{vdW} and r_e^{vdW} are the van der Waals radii of the corresponding atoms, internal and external to the surface, respectively.

For a geometric representation of intermolecular interactions, the Hirshfeld surface is colored in red-white-blue colors depending on the d_{norm} value. The contacts with distances equal to the sum of the vdW radii are shown in white (moderate magnitude of intermolecular interactions), and the contacts with distances shorter or longer than the vdW radii are shown in red and blue, respectively (strong and weak magnitude of intermolecular interactions).

The d_{norm} decorated HSs are mainly discussed concerning the corresponding fingerprint plots. The fingerprint plot is a 2D diagram derived from the HS and shows the frequency of occurrence of each d_e and d_i combination on the surface. Each unique d_e vs d_i combination in the fingerprint plot is interpreted as representing a specific type of intermolecular interaction.

Previously, we used Hirschfeld surface analysis to study intermolecular interactions in cathinone crystal drugs and proved it to be an effective and versatile approach in forensic researches [24–26].

Results and Discussion

Selected intermolecular distances O···H in the crystalline cells of progesterone, 17α-hydroxyprogesterone and testosterone compounds are listed in Table (Here ^{3}O means, for example, the oxygen atom in position 3 of the sterane cycle in Figure 1).

T a b l e

**Selected intermolecular O···H distances (d) in crystalline cells of progesterone,
17α-hydroxyprogesterone, and testosterone according to X-ray data**

Parameter	d, Å	Parameter	d, Å
Progesterone			
^{3}O···H (C6H$_2$) **B**	2.503	^{3}O···H (^{13}CH$_3$)	2.957
^{3}O···H ($^{17\beta}$COCH$_3$) **D**	2.532	O ($^{17\beta}$COCH$_3$)···H (C15H$_2$) **D**	2.978
O ($^{17\beta}$COCH$_3$)···H (C2H$_2$) **A**	2.695	^{3}O···H (C8H)	2.994
^{3}O···H (C16H$_2$) **D**	2.702	O ($^{17\beta}$COCH$_3$)···H (C16H$_2$) **D**	3.100
^{3}O···H (^{10}CH$_3$)	2.800	O ($^{17\beta}$COCH$_3$)···H (C6H$_2$) **B**	3.294
17α-Hydroxyprogesterone			
^{3}O···H ($^{17\alpha}$OH) **D**	1.937	O ($^{17\beta}$COCH$_3$)···H($^{17\beta}$COCH$_3$)	3.004
^{3}O···H ($^{17\beta}$COCH$_3$) **D**	2.519	O ($^{17\beta}$COCH$_3$)···H (C16H$_2$) **D**	3.116
$^{17\alpha}$O···H (C6H$_2$) **B**	2.816	^{3}O···H (^{10}CH$_3$)	3.419
$^{17\alpha}$O···H (^{10}CH$_3$)	2.959		
Testosterone			
^{3}O···H ($^{17\beta}$OH) **D**	1.805	^{3}O···H (C17H) **D**	2.617
O ($^{17\beta}$OH)···H (C2H$_2$) **A**	2.544	O ($^{17\beta}$OH)···H (C15H$_2$) **D**	3.057
O ($^{17\beta}$OH)···H (^{10}CH$_3$)	2.609	^{3}O···H (^{13}CH$_3$)	3.195

Progesterone. The structure of the progesterone cell and the Hirschfeld d_{norm} surface are shown in Figure 2a. The presence of three intense red spots on the Hirschfeld d_{norm} surface indicates the occurrence of strong O···H/H···O interactions. These interactions involve hydrogen bonding between the oxygen atom of C=O keto group of the ring A and the hydrogen atom at C6 atom of cyclohexane ring B of another molecule with a distance of 2.503 Å (Fig. 2b), hydrogen bonding between the oxygen atom of the keto group ring A and the hydrogen atom of the methoxy group at C17 atom of cyclopentane ring D with a distance of 2.532 Å (Fig. 2c), and hydrogen bonding between the O atom of the methoxy group at C17 atom and the hydrogen atom at C2 atom of the A ring neighbouring molecule with a distance of 2.695 Å (Fig. 2d). There are also weak O···H/H···O interactions associated with the contacts of the oxygen atom of C=O group with the hydrogen atom at C16 of cyclopentane ring D and the hydrogen atom of the methyl group at C10 atom with distances of 2.702 Å and 2.800 Å, respectively (Fig. 2b,d). Another intermolecular O···H/H···O contacts in the progesterone crystal with distances 2.957, 2.978, 2.994, 3.100, and 3.294 Å are far-reaching and are presented in Table, Figure 2e-i.

a

b

c

d

e

f

g

h

i

j

k
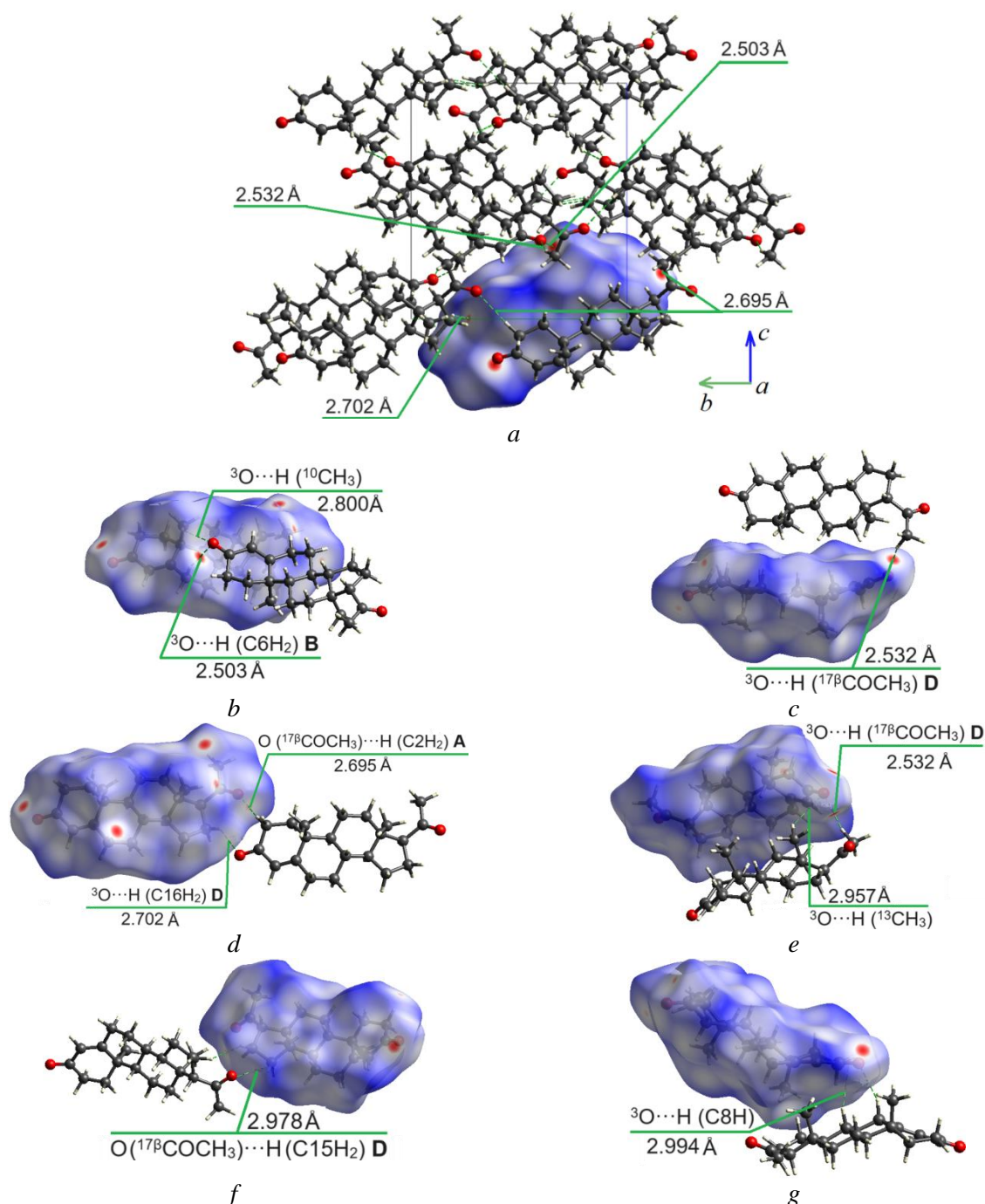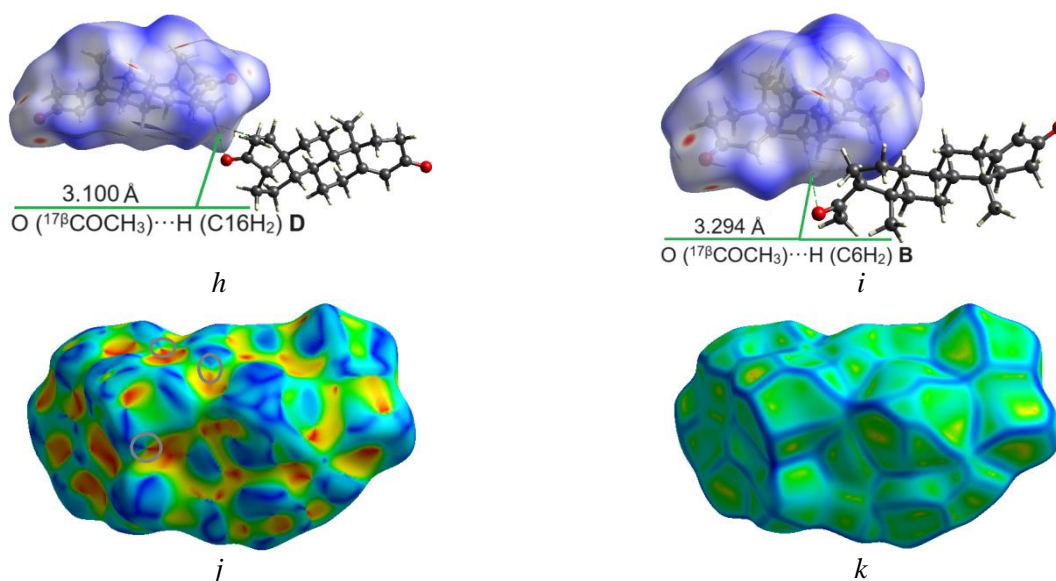
Figure 2. Progesterone crystal cell (*a*) and Hirschfeld surfaces mapped with d_{norm} (*b–i*), shape index (*j*) and curvedness (*k*). CH···O intermolecular interactions are shown by green dashed lines with indicated experimental values of intermolecular contact lengths

The shape index is a mathematical descriptor used to characterize the local shape of a surface. Red, blue, and green features on the shape-index map represent different structural characteristics or properties of the molecular packing. The shape-index surface of progesterone shows the presence of red and blue triangle pairs (grey circles in Figure 2*j*) on the surface, indicating weak C–H···π interactions. These interactions are mapped *via* green patches on the HS curvedness (Fig. 2*k*).
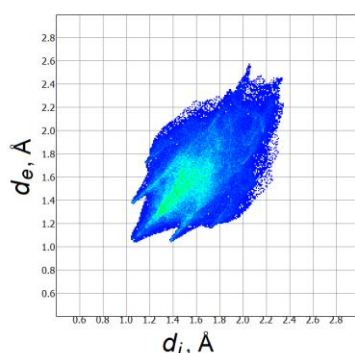
The total 2D Hirschfeld surface of all contacts in the progesterone crystal cell
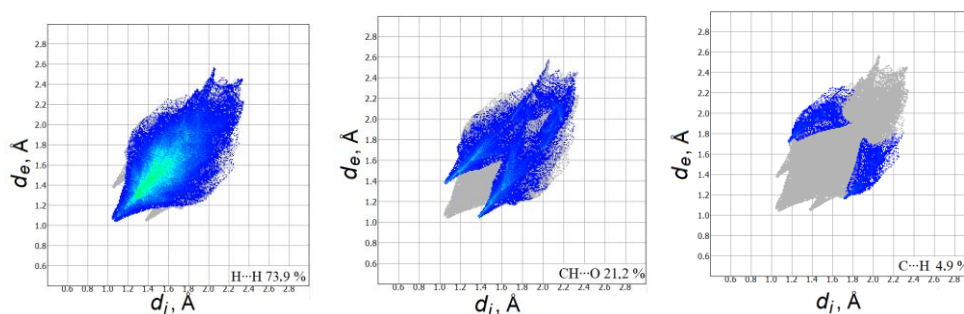
Figure 3. Two-dimensional (2D) fingerprint plots for progesterone crystal cell. The outline of the full fingerprint contribution is shown in grey

Figure 3 shows two-dimensional (2D) diagrams with detailed information about the contribution (in %) of each contact to the total Hirschfeld surface. The Hirschfeld 2D surface representation uses d_e and d_i pairs to characterize the distances from points on the surface to the nearest atoms inside and outside the molecule.

Contacts that are not on the Hirschfeld surface are not marked, and contacts with some contributions are shown in blue. Contacts that occupy the largest surface area are depicted in green.

The CH···O interactions on the fingerprint diagram are represented by two different spikes of equal length (Fig. 3). The contribution of these contacts to the total HS area is significant 21.2%. The H···H contacts contribute 73.9 % to the total HS with the $d_e = d_i \sim 1.1$ Å, indicating close packing. (Fig. 3). In addition, in the 2D diagram, we can see a small contribution of C···H contacts (4.9 %), which are responsible for the presence of C–H···π interactions between aromatic rings and adjacent hydrogen atoms. The contribution of C–H···π interactions is low due to the non-planarity of the progesterone molecular skeleton. Thus, the supramolecular arrangement of molecules in the progesterone crystal is primarily determined by CH···O hydrogen bonds and non-valent H···H contacts along with substantial van der Waals contacts. The contribution of C···H contacts (C–H···π interactions) provides further stability to the progesterone crystal packing.

17α-Hydroxyprogesterone. The presence of the –OH group at C17 atom of cyclopentane ring **D** in the 17α-hydroxyprogesterone molecule determines several intermolecular O···H/H···O hydrogen bonds with distances of 1.937 Å in the crystal packing, formed due to the oxygen atom of the keto group **A** ring of one molecule and the hydrogen atom of the –OH group in the 17α-position of another molecule. These intermolecular interactions are depicted by the two intense red spots on the Hirschfeld d_{norm} surface (Fig. 4 a, b). The existence of a strong hydrogen bond ^{3}O···HO${}^{17\alpha}$ in the crystal packing of 17α-hydroxyprogesterone was predicted in Ref. [27]. In addition, the structure of 17α-hydroxyprogesterone contains several weaker O···H interactions between the oxygen atom of C=O keto group ring **A** and the hydrogen atom of the methoxy group at C17 atom (^{3}O···H (${}^{17\beta}$COCH$_3$)) and between the oxygen atom of the methoxy group at C17 atom and the hydrogen atom at C6 atom of cyclohexane ring **B** of another molecule (${}^{17\alpha}$O···H (C6H$_2$)) with distances of 2.519 Å and 2.816 Å, respectively (Table 1, Figure 4 b, c), which are marked by pale white spots on the Hirschfeld surface. Intermolecular contacts of the O···H/H···O type in the 17α-progesterone crystal with distances 2.959, 3.004, and 3.116 Å are far-reaching (Table 1, Figure 4 d-f). The ^{3}O···H (${}^{17\beta}$COCH$_3$) **D**, O (${}^{17\beta}$COCH$_3$)···H (C16H$_2$) **D** and ^{3}O···H (^{10}CH$_3$) contacts are also present in the crystal cell of progesterone, and the first two O···H contacts in progesterone and 17α-hydroxyprogesterone have close distances (Table 1). The ^{3}O···H (^{10}CH$_3$) contact in the crystal cell of 17α-hydroxyprogesterone (3.419 Å, Figure 4g) is much weaker compared to that of progesterone (2.800 Å).

The main H···H intermolecular contacts are shown in the middle of the 2D fingerprint plots and contribute 74.2% to the total HS. The O···H/H···O interactions comprise 22.3 % to the total HS and are indicated by two large spikes (Fig. 5), they are also characteristic of symmetrical O···H hydrogen bond interaction, *i.e.* both the hydrogen and oxygen atoms are involved in similar interactions with neighbouring atoms, resulting in a balanced and symmetrical arrangement. The C···H interactions additionally stabilize the crystal structure of 17α-hydroxyprogesterone with contribution of 3.5% to the total HS (Fig. 5). These contacts correspond to the C–H···π interactions between hydrogen atom in a C–H bond and the π electron cloud of an adjacent aromatic ring and are visualized as red and blue triangle pairs on the shape-index surface (Fig. 4h) and by flat green regions on the curvedness (Fig. 4i).

Testosterone. The crystalline packing and the calculated HS of the testosterone mapped over d_{norm} is presented in Figure 6a. One can see two intense red spots on the HS, which belong to the interactions of the oxygen atom of the keto group at ring **A** of one molecule with the hydrogen atom of the hydroxy group in the 17β-position at C17 atom of cyclopentane ring **D** of another molecule with distances of 1.805 Å (Fig. 6b). We also identified weaker O···H contacts between the oxygen atom of C=O keto group ring **A** and the hydrogen atom at C17 atom with distances of 2.617 Å, and between the oxygen atom of hydroxy group at C17 atom with hydrogen atom at C2 atom of the A ring, and with hydrogen atom of the methyl group at C10 atom with distances of 2.544 Å and 2.609 Å, respectively, which are marked by faint light spots on the Hirschfeld surface (Fig. 6c). Another intermolecular contacts of the O···H/H···O type in testosterone crystal are long-range with distances of 3.057 Å and 3.195 Å (Table 1, Figures 6d, e)

The shape-index surface with marked red and blue triangles represents regions where C–H···π stacking interactions are prominent (Fig. 6f). The green regions on the curvedness indicate a relatively planar surface, where the C–H···π stacking interactions can occur (Fig. 6g).

Figure 7 shows 2D fingerprint plots with the contribution of each contact to the total Hirshfeld surface for testosterone.
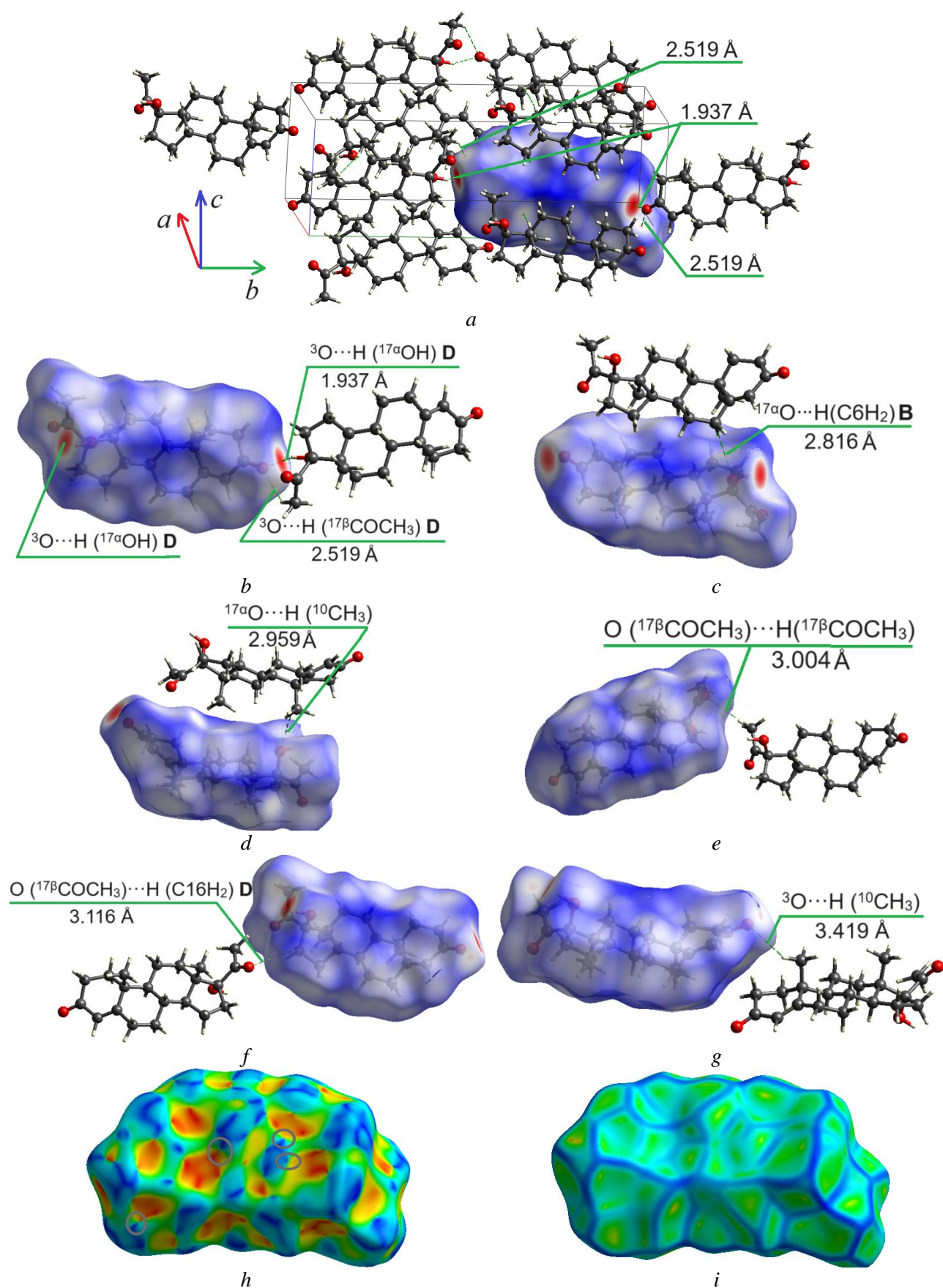
Figure 4. Crystal cell and Hirschfeld surface (d_{norm}) for 17α-hydroxyprogesterone (*a*), selected dimer configurations with indicated intermolecular distances (*b-g*), shape index (*h*), and curvedness (*i*)

The total 2D Hirschfeld surface of all contacts in the 17α-progesterone crystal cell
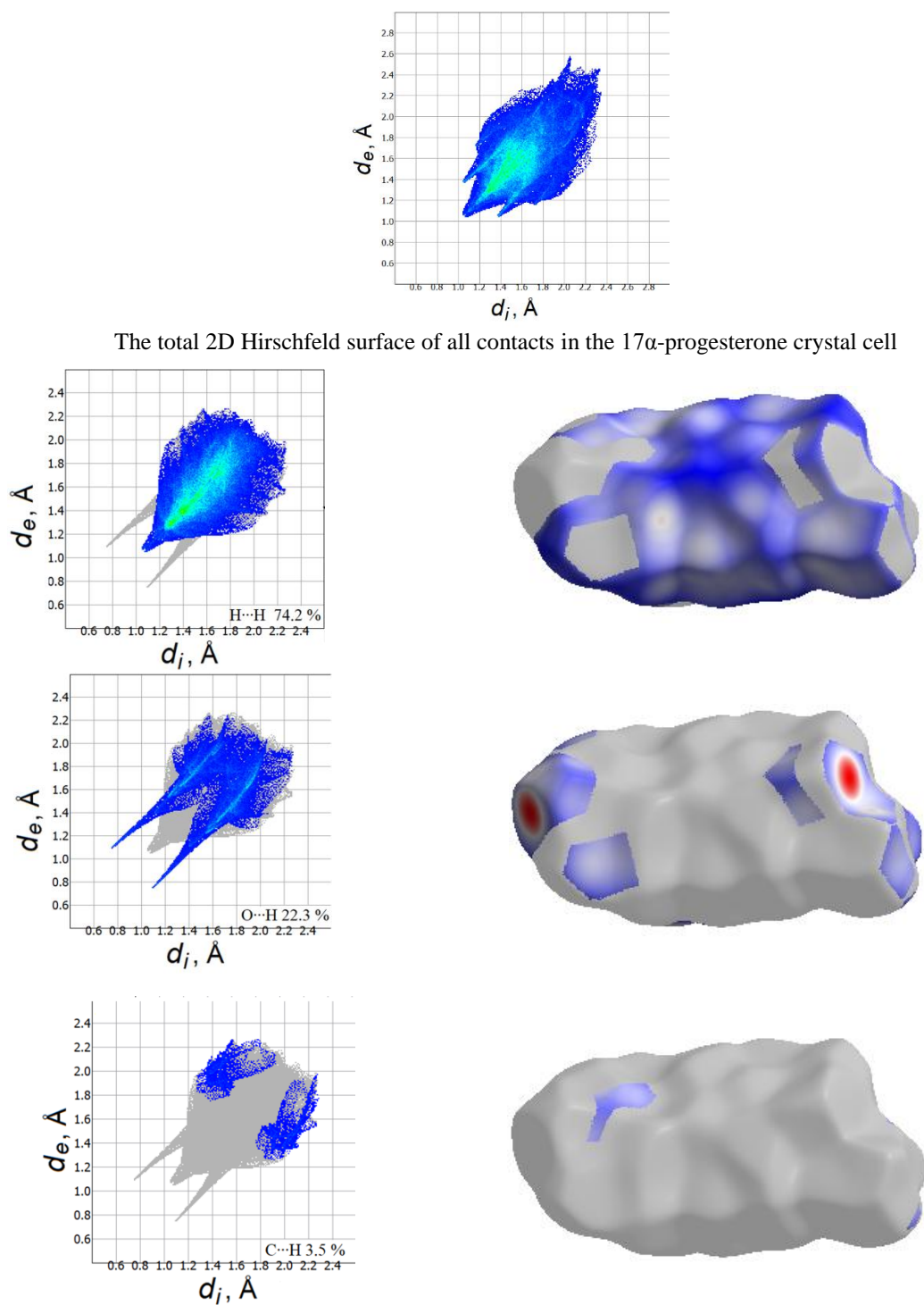
Figure 5. Two-dimensional fingerprint plots for 17α-progesterone crystal cell and their corresponding d_{norm} surface. The outline of the full fingerprint contribution is shown in grey
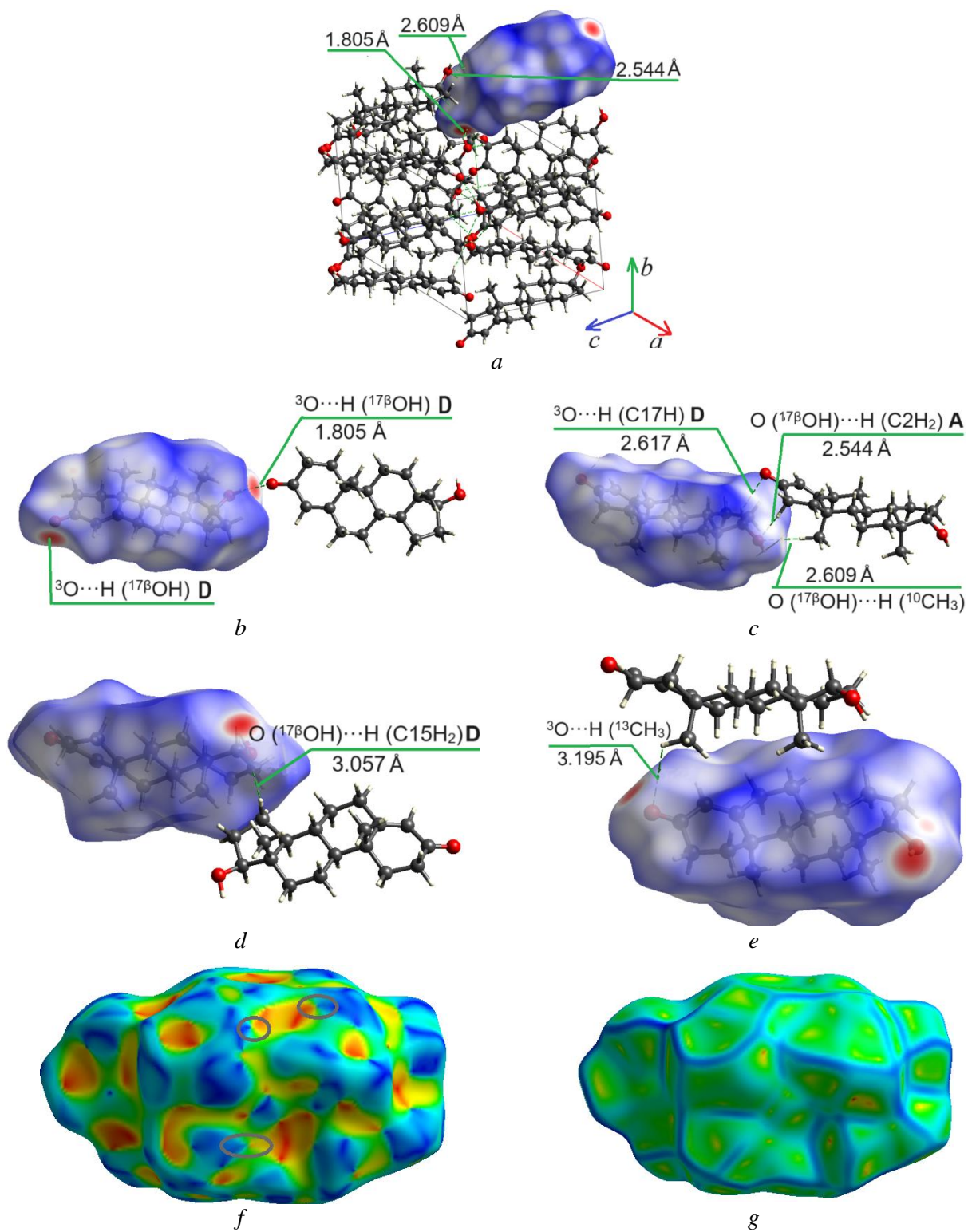
Figure 6. Crystal cell and Hirschfeld d_{norm} surface for testosterone (*a*), selected dimer configurations with indicated intermolecular distances (*b-e*), shape index (*f*), and curvedness (*g*)

The total 2D Hirschfeld surface of all contacts
in the testosterone crystal cell
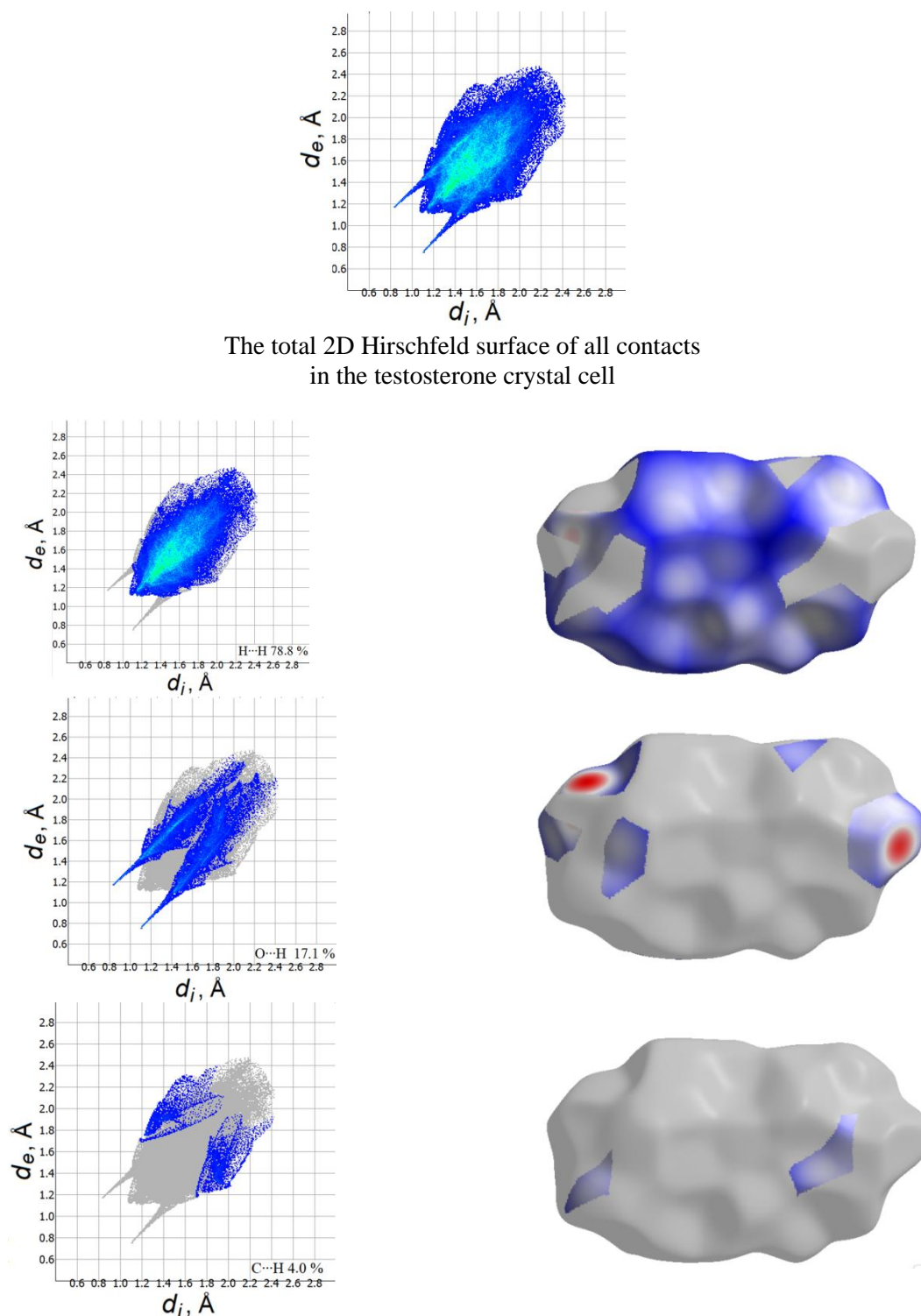
Figure 7. Two-dimensional fingerprint plots for testosterone crystal cell and their corresponding d_{norm} surface

According to the fingerprint plot for testosterone crystal cells, the O···H intermolecular interactions contribute 17.1 % to the total HS. Nonvalent H···H contacts have the largest contribution (78.8 %) to the total HS, and C···H contacts contribute only 4.0%.

Thus, the supramolecular arrangement of molecules in the progesterone, 17α-hydroxyprogesterone and testosterone crystals is primarily determined by intermolecular forces, including Van der Waals forces, hydrogen bonding and C–H···π interactions.

Conclusions

Hirschfeld surfaces analysis for each of the three crystal structures of the steroid hormones including progesterone, 17α-hydroxyprogesterone and testosterone, enabled the determination of various aspects related to the molecular arrangements and intermolecular interactions within these crystals. It was found that the ability to form intermolecular O···H/H···O hydrogen bonds is due to the presence in the hormone structure of the oxygen atom of the keto group in the third position of the ring **A**, the hydroxyl group in the 17α-position in the 17α-hydroxyprogesterone molecule and in the 17β-position in the testosterone molecule, and also due to the oxygen atom of the methoxy group –OCH$_3$ in the 17β position in progesterone and 17α-hydroxyprogesterone molecules. These structural details of crystallization are important for understanding the general biochemical properties of such hormones.

The H···H and C···H/H···C contacts in the crystal packages of all the studied hormones were also determined. Two-dimensional (2D) plots (d_e vs d_i) obtained from Hirschfeld surfaces made it possible to establish the relative contribution of each type of interaction to the overall Hirschfeld surface. It is shown that H···H interactions make the greatest contribution to the overall Hirschfeld surface, accounting for approximately 80% of the surface. These interactions involve hydrogen atoms from adjacent molecules, contributing to the cohesive forces between molecules in the crystal lattice. The O···H/H···O interactions contribute about 20 % to the HS and are important for maintaining the structural integrity and stability of the crystal. The C···H/H···C interactions give the smallest contribution, approximately 4% of the HS, and may play a role in the packing arrangement of hormone molecules within the crystal but are less prevalent compared to the typical hydrogen bonding. We believe that the Hirschfeld surface analysis of molecular crystal packing could be useful for understanding the mechanisms of the hormones docking in their interaction with various receptors.

Funding

Conflicts of Interest

The authors declare no conflict of interest.

Author Information*

_____

*The authors' names are presented in the following order: First Name, Middle Name and Last Name

Nataliya Mikolaevna Karaush-Karmazin (*corresponding author*) — Senior Researcher, Department of Chemistry and Nanomaterials Science, Bohdan Khmelnytsky National University, 18031, Cherkasy, Ukraine; e-mail: karaush22@ukr.net; https://orcid.org/0000-0001-9360-2593

Boris Filippovich Minaev (*corresponding author*) — Professor, Department of Chemistry and Nanomaterials Science, Bohdan Khmelnytsky National University, 18031, Cherkasy, Ukraine; Senior Researcher — Department of Physics and Astronomy, Uppsala University, SE-752 37, Uppsala, Sweden; e-mail: bfmin43@ukr.net; https://orcid.org/0000-0002-9165-9649

Valentina Alexandrovna Minaeva — Senior Researcher, Assistant Professor, Department of Chemistry and Nanomaterials Science, Bohdan Khmelnytsky National University, 18031, Cherkasy, Ukraine; e-mail: minaeva@cdu.edu.ua; https://orcid.org/0000-0001-9318-1661

Olexandr Olexandrovich Panchenko — Researcher, Department of Chemistry and Nanomaterials Science, Bohdan Khmelnytsky National University, 18031, Cherkasy, Ukraine; e-mail: panchenko9b@gmail.com; https://orcid.org/0000-0001-7669-1424

Hans Ågren — Professor, Department of Physics and Astronomy, Uppsala University, SE-752 37, Uppsala, Sweden; e-mail: hagren@kth.se; https://orcid.org/0000-0002-1763-9383

Author Contributions

The manuscript was written through contributions of all authors. All authors have given approval to the final version of the manuscript. CRediT: **Nataliya Mikolaevna Karaush-Karmazin** conceptualization, data curation, investigation, methodology, validation, visualization, resources, writing-original draft, writing-

review & editing; **Valentina Alexandrovna Minaeva** conceptualization, data curation, formal analysis, writing-original draft, writing-review & editing; **Olexandr Olexandrovich Panchenko** data curation, formal analysis, visualization; **Boris Filippovich Minaev** conceptualization, data curation, formal analysis, supervision, validation, writing-original draft, writing-review & editing; **Hans Ågren** conceptualization, supervision, validation, writing-review & editing

References

1   Taraborrelli, S. (2015). Physiology, production and action of progesterone. *Acta Obstetricia et Gynecologica Scandinavica, 94*, S8–16. https://doi.org/10.1111/aogs.12771

2   Bitzer, J. (2010). Progesterone, progestins and psychosomatic health of women. *Hormone Molecular Biology and Clinical Investigation, 3*, 477–480. https://doi.org/10.1515/HMBCI.2010.070

3   Nagy, B., Szekeres-Barthó, J., Kovács, G.L., Sulyok, E., Farkas, B., Várnagy, Á., Vértes, V., Kovács, K., & Bódis, J. (2021). Key to Life: Physiological Role and Clinical Implications of Progesterone. *Int. J. Mol. Sci., 22*, 11039; https://doi.org/.org/10.3390/ijms222011039

4   Minaeva, V.A., Minaev, B.F., & Hovorun, D.N. (2008). Vibrational spectra of the steroid hormones, estradiol and estriol, calculated by density functional theory. The role of low-frequency vibrations. *Ukr. Biokhim. Zh., 80* (4), 82–95.

5   Mooij, C.F., Parajes, S., Pijnenburg-Kleizen, K.J., Arlt, W., Krone, N., & van der Grinten, H.L.C. (2015). Influence of 17-Hydroxyprogesterone, Progesterone and Sex Steroids on Mineralocorticoid Receptor Transactivation in Congenital Adrenal Hyperplasia. *Hormone Research in Paediatrics, 83*, 414–421. https://doi.org/10.1159/000374112

6   Mooradian, A.D., Morley, J.E., & Korenman, S.G. (1987). Biological actions of androgens. *Endocrine Reviews, 8*, 1–28. https://doi.org/10.1210/edrv-8-1-1

7   Tyagi, V., Scordo, M., Yoon, R.S., Liporace, F.A., & Greene, L.W. (2017). Revisiting the role of testosterone: Are we missing something? *Reviews in urology, 19*(1), 16–24. https://doi.org/10.3909/riu0716

8   Huo, S., Scialli, A.R., McGarvey, S., Hill, E., Tügertimur, B., Hogenmiller, A., Hirsch, A.I., & Fugh-Berman, A. (2016) Treatment of Men for "Low Testosterone": A Systematic Review. *PLoS ONE 11*, e0162480. https://doi.org/10.1371/journal.pone.0162480

9   Cherkasova, O.P., Minaev, B.F., Baryshnikov, G.V., Tkachenko, L.I., Minaeva, V.A., Smirnova, I.N., Sapozhnikov, D.A., Kargovsky, A.V., & Shkurinov, A.P. Analysis of intermolecular interactions in progesterone and 17α-hydroxyprogesterone crystals. (2013) *38th International Conference on Infrared, Millimeter, and Terahertz Waves* (IRMMWTHz 2013). Mainz on the Rhine, We P2-08.

10   Gellman, S.H. (1997). Introduction: Molecular Recognition. *Chemical Reviews, 97*, 1231–1232. https://doi.org/10.1021/cr970328j

11   Bader, R.F.W. (1990). *Atoms in Molecules. A Quantum Theory*. Clarendon Press, Oxford, 438. ISBN: 0198551681, 9780198551683

12   Cherkasova, O.P., Nazarov, N.M., Sapozhnikov, D.A., Man'kova, A.A., Fedulova, E.V., Volodin, V.A., Minaeva, V.A., Minaev, B.F., Baryshnikov, G.V. Vibrational spectra of corticosteroid hormones in the terahertz range (2011). Proc. SPIE 7376, *Laser Applications in Life Sciences*, 73760P. https://doi.org/10.1117/12.871047

13   Hirshfeld, F.L. (1977). Bonded-Atom Fragments for Describing Molecular Charge Densities. *Theoretica Chimica Acta, 44*, 129–138. https://doi.org/10.1007/BF00549096

14   Suda, S., Tateno, A., Nakane, D., & Akitsu, T. (2023). Hirshfeld Surface Analysis for Investigation of Intermolecular Interaction of Molecular Crystals. *International Journal of Organic Chemistry, 13*, 57–85. https://doi.org/10.4236/ijoc.2023.132006

15   Spackman, M.A. & McKinnon, J.J. (2002). Finger printing intermolecular interactions in molecular crystals. *CrystEngComm, 4*, 378–392. https://doi.org/10.1039/B203191B

16   Psycharis, V., Dermitzaki, D., & Raptopoulou, C.P. (2021). The Use of Hirshfeld Surface Analysis Tools to Study the Intermolecular Interactions in Single Molecule Magnets. *Crystals, 11*, 1246. https://doi.org/10.3390/cryst11101246

17   Spackman, M.A. & Jayatilaka, D. (2009). Hirshfeld Surface Analysis. *CrystEngComm, 11*, 19–32. https://doi.org/10.1039/B818330A

18   Serantoni, E.F., Krajewski, A., Mongiorgi, R., Riva di Sanseverino, L., & Cameroni, R. (1975). Progesterone 4-Pregnen-3,20-dione (progesterone, form II). *Crystal structure communications, 4*, 189–192.

19   Roberts, P.J., Pettersen, R.C., Sheldrick, G.M., Isaacs, N.W., & Kennard, O. (1973). Crystal and molecular structure of 17β-hydroxyandrost-4-en-3-one (testosterone). *Journal of the Chemical Society Perkin Transactions, 2*, 1978–1984. https://doi.org/10.1039/p29730001978

20   Declercq, J.P., Germain, G., & van Meerssche, M. (1972). 17a-Hydroxy-4-pregnene-3,20-dione. *Crystal Structure Communications, 1*, 9–13. https://doi.org/10.1007/978-94-017-3115-7

21 Shikii, K., Sakamoto, S., Seki, H., Utsumi, H., & Yamaguchi, K. (2004). Narcissistic aggregation of steroid compounds in diluted solution elucidated by CSI-MS, PFG NMR and X-ray analysis. *Tetrahedron, 60*, 3487–3492. https://doi.org/10.1016/j.tet.2004.02.030

22 Turner, M.J., McKinnon, J.J., Wolff, S.K., Grimwood, D.J., Spackman, P.R., Jayatilaka, D., & Spackman, M.A. (2017). *Crystal Explorer, 17.5*. University of Western Australia. https://crystalexplorer.net/

23 Spackman, P.R., Turner, M.J., McKinnon, J.J., Wolff, S.K., Grimwood, D.J., Jayatilaka, D., & Spackman, M.A. (2021). CrystalExplorer: a program for Hirshfeld surface analysis, visualization and quantitative analysis of molecular crystals. *Journal of Applied Crystallography, 54*, 1006–1011 https://doi.org/10.1107/S1600576721002910

24 Minaeva, V., Panchenko, A., Karaush-Karmazin, N., Nycz, J., & Minaev, B. (2023). Manifestation of Intermolecular Interactions in the IR Spectra of 2-and 4-Methylmethcathinones Hydrochlorides: DFT Study and Hirshfeld Surfaces Analysis. *Biointerface Research in Applied Chemistry, 13*, 202 https://doi.org/10.33263/BRIAC133.202

25 Minaeva, V.A., Karaush-Karmazin, N.N., Panchenko, A.A., Heleveria, D.N., & Minaev, B.F. (2021). Hirshfeld surfaces analysis and DFT study of the structure and IR spectrum of N-ethyl-2-amino-1-(4-chlorophenyl)propan-1-one (4-CEC) hydrochloride. *Comput. Theor. Chem., 1205*, 113455. https://doi.org/10.1016/j.comptc.2021.113455

26 Minaeva, V., Karaush-Karmazin, N., Panchenko, O., Minaev, B., & Ågren, H. (2023). Hirshfeld and AIM Analysis of the Methylone Hydrochloride Crystal Structure and Its Impact on the IR Spectrum Combined with DFT Study. *Crystals, 13*, 383. https://doi.org/10.3390/cryst13030383

27 Duax, W.L. & Norton, D.A. (1975). *Atlas of steroid structure*. Plenum press, New York, 1, 473. ISBN: 0306661012

Article

Sejal P. Gandhi*[1] , Gresi D. Mate[2], Dheeraj H. Nagore[3] , Sohan S. Chitlange[1]

*[1]Department of Pharmaceutical Chemistry, Dr. D.Y. Patil Institute of Pharmaceutical Sciences
and Research, Pimpri, Pune, Maharashtra, India;*
*[2]Department of Pharmaceutical Quality Assurance, Dr. D.Y. Patil Institute of Pharmaceutical Sciences
and Research, Pimpri, Pune, Maharashtra, India;*
*[3]Department of Pharmacognosy, Dr. D.Y. Patil Institute of Pharmaceutical Sciences
and Research, Pimpri, Pune, Maharashtra, India*
(*Corresponding author′s e-mail: sejal.gandhi@dypvp.edu.in)

Quantifying Curcumin, Gallic Acid, and Resveratrol in a Polyherbal Mixture: a Robust HPTLC Method

The need for this study arises from the growing importance of polyherbal formulations in herbal medicine, particularly due to their potential health benefits and synergistic effects. In this research, development and validation of an HPTLC method for simultaneous quantification of curcumin, gallic acid, and resveratrol in a polyherbal mixture are primary focus. Additionally, study assesses the Total Phenolic Content (TPC), Total Flavonoid Content (TFC) and antioxidant potential using the 2,2-diphenyl-1-picrylhydrazyl (DPPH) assay. The results reveal that TPC is 212.1 mg gallic acid equivalent per gram of plant material, and the TFC is 133.06 mg rutin equivalent per gram of plant material. Notably, DPPH assay demonstrates mixture's robust antioxidant activity, with an IC_{50} value of 3.83 μg/ml. Furthermore, HPTLC method used a carefully optimized mobile phase, providing excellent resolution for gallic acid, resveratrol, and curcumin with corresponding R_f values of 0.18, 0.43, and 0.53. This method is highly linear over a concentration range of 200–1000 ng/band for all three compounds. Precision studies confirm method's reproducibility with low Relative Standard Deviation values below 2 %. Ultimately, this HPTLC method offers a simple, accurate, precise, and cost-effective solution for routine quality control analysis, shedding light on potential applications of the polyherbal mixture in various therapeutic contexts.

Keywords: HPTLC, curcumin, gallic acid, resveratrol, simultaneous estimation, standardization, anti-oxidant, validation, polyherbal mixture.

Introduction

Since ancient times, herbal drugs have been a blessing to human kind. Worldwide, both single plant extracts and mixtures of herbs are utilized to treat a variety of human disorders [1]. The World Health Organization (WHO) estimates that the usage of herbal remedies is two to three times more frequently than conventional drug globally. Natural compounds contain a variety of chemically active substances which are accountable for their vast pharmacological activity. In recent pharmacology and development of drug, a single chemical substance is accountable for the majority of the beneficial effects of the drug, while in Ayurvedic preparations either a single herb or multiple herb known as polyherbal formulation are responsible for the activity [2]. In polyherbal formulations, the synergistic effects of many medicinal plants contribute to increasing the drug efficacy [3]. These Ayurveda polyherbal formulations have a challenging task involving consistency in quality control, which will guarantee the finished herbal products' therapeutic effectiveness as promised by the accepted Ayurveda texts. The wide varieties of chemical compounds are difficult to analyze, authenticate, and separate fast with appropriate accuracy, precision, and reproducibility [4].

Polyherbal formulation refers to a medicinal or therapeutic preparation that contains a combination of multiple herbs or botanical extracts. These formulations are created by combining different plant-based ingredients known for their therapeutic properties to achieve synergistic effects and enhance the overall efficacy of the formulation [3]. These are typically developed with the intention of providing a synergistic effect by combining the therapeutic properties of various medicinal plants. An in-house polyherbal mixture was prepared which included *Vitis vinifera, Panax ginseng, Withania somnifera, Tinospora chordifolia, Curcuma longa, Zingiber officinale* and *Glycyrrhiza glabra.* The grapevine, or *Vitis vinifera*, contains a number of biologically active components, including anthocyanins, proanthocyanidins, polyphenols, flavonoids and

resveratrol derivative of the stilbene family [5]. *Vitis vinifera* is the most abundant source of resveratrol, a naturally-occurring phytoalexin and polyphenol compound. Resveratrol possesses biological properties that offer health advantages, including safeguarding against conditions like atherosclerosis, coronary heart disease, and cancer [6]. These substances have been proven to exhibit a variety of pharmacological effects, which include antiviral, anti-inflammatory, antimicrobial, and antioxidant properties. These properties have health benefits for human, including reducing lipoproteins of low-density, reducing the risk of heart related disease, cancer, respiratory and gastrointestinal issues, and boosting the immunity [7]. *Panax ginseng* holds a significant position among the tonic treatments used in oriental medicine. *Ginseng* is a high-grade plant with numerous pharmacological properties, including restorative, tonic, nootropic, antiaging, and others [8]. *Curcuma longa* or turmeric is significant aromatic and medicinal plant used as a spice, medicine, cosmetic, and dye [9]. The most significant component of turmeric is curcumin which is responsible for its biological effects. Curcumin offers a numerous beneficial therapeutic benefits, including antineoplastic, antiapoptotic, antiangiogenic, cytotoxic and immunomodulatory [10]. *Glycyrrhiza glabra* is a widely used herb in the ancient Ayurvedic medical tradition, as a medicine and also utilized as a flavouring agent. *Licorice* is used to treat inflammation, liver problems as well as peptic ulcers, arthritic ailments, and gastrointestinal infections. *Licorice* is also used as an antidote to the toxicity of chemotherapy [11].

Standardization of natural substances is a difficult task because of their varied contents. Herbal products must be controlled precisely to ensure reproducible quality. Therefore, standardizing crude drugs poses many challenges. On the other hand, standardization of herbal extract helps in maintaining the quality of the extract and thus its efficacy [12]. To properly identify natural drugs, one should possess an authentic reference standard. A marker is a compound that is unique to the plant being studied and is present in quantifiable level and can be easily separated [13].

HPTLC has been extensively used for the evaluation of herbal drugs and has evolved into standard analytical method owing to its beneficial aspects, including being economical, having a high sampling throughput, and requiring little sample preparation [14–16]. Gallic acid (3,4,5-trihydroxybenzoic acid), resveratrol (3,5,4′-Trihydroxystilbene) and curcumin (1,7-bis-(4-hydroxy-3-methoxyphenyl)-hepta-1,6-diene-3,5-dione) (Fig 1) have been analyzed by HPLC and HPTLC either singly or with one another but simultaneous estimation of all three is not reported till date [17–20].

The aim of the current study is to develop a simple, precise and reproducible HPTLC method for estimation of gallic acid, resveratrol and curcumin simultaneously in an in-house polyherbal mixture. Developed method is also validated as per ICH Validation Guidelines [21]. Quantitative phytochemical estimation of the mixture for total phenol and flavonoid was also performed along with its anti-oxidant potential.

a) gallic acid   b) resveratrol   c) curcumin
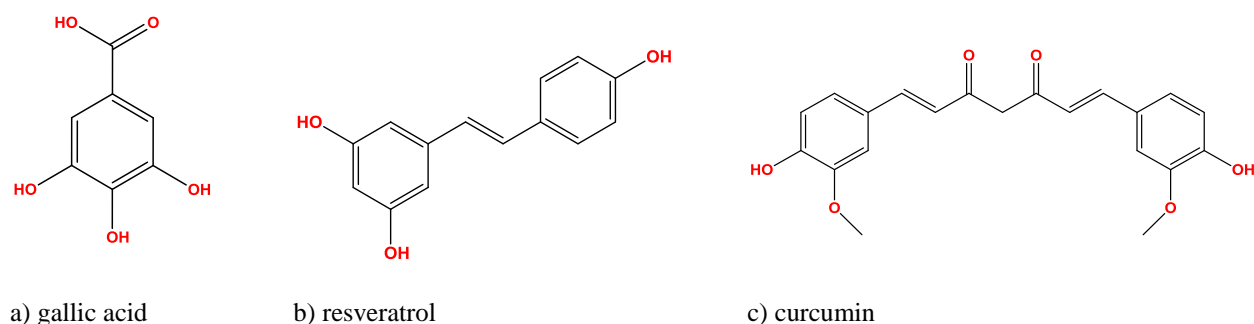
Figure 1. Objects of the study

Experimental

Materials

A CAMAG HPTLC system comprising semi-automatic sample applicator Linnomat-5, CAMAG TLC plate scanner, CAMAG WINCAT software (version 1.44 CAMAG) and Hamilton Syringe (100 μL) were used during analysis.

Standard resveratrol (Sigma Aldrich), gallic acid (Loba Chemical), 2,2-diphenylpicrylhydrazyl (DPPH) (Sigma Aldrich), rutin (Loba Chemical), ascorbic acid (Sigma Aldrich) and other Analytical Research (AR) Grade chemicals were used.

Methodology
Formulation of polyherbal mixture (PM)

The formulation of a polyherbal mixture involves combining multiple herbal ingredients to create a synergistic blend with desired therapeutic effects. The polyherbal mixture includes *Vitis vinifera, Panax ginseng, Withania somnifera, Tinospora chordifolia, Curcuma longa, Zingiber officinale* and *Glycyrrhiza glabra.* The prepared in-house polyherbal mixture consists of major phytoconstituents as resveratrol, gallic acid and curcumin.

Quantitative phytochemical analysis
Total Phenolic Content (TPC)

The TPC for polyherbal mixture were calculated via the approach of Singleton et al. (1999) with small changes [22]. 0.5 ml of 10 % Folin Ciocalteau Reagent (FCR) was added to 0.2 ml of a test sample, and left for 5 minutes. 2.0 ml of 10 % sodium carbonate was added after 5 minutes. Prepared solution was incubated in dark for 30 minutes. The absorbance was recorded at 765 nm by UV-Visible Spectrophotometer against blank. The TPC content was measured as gallic acid equivalents (GAE)/g of plant material as average of three readings using gallic acid linearity.

Total Flavonoid Content (TFC)

The TFC was evaluated according to the standard aluminum chloride procedure using rutin as the reference standard [23]. 2 ml of plant extract were combined with 0.3 ml of 5% $NaNO_2$. 0.3 ml of 10 % $AlCl_3$ was added after 5 minutes. Then 4 ml of 10% NaOH solution was added to the reaction mixture. Final volume of 10 ml was made using distilled water. Absorbance of the mixture was taken at 510 nm. Rutin standard curve measurements were used to calculate the TFC, which was then reported as rutin equivalent (RU) per g of plant material as average of three readings.

Antioxidant assay by DPPH method

The polyherbal mixture capacity for scavenging free radicals was measured using DPPH radical method as it has capability to donate hydrogen or scavenged radicals [24, 25]. 0.1 mM DPPH solution in methanol was prepared and 2 ml of this solution was added to 2 ml of extract (or standard) solution at varied concentrations (5–50 µg/ml). The absorbance was taken at 517 nm after 30 minutes. Lower absorbance f the reaction mixtures indicated greater free radical scavenging capacity. The following equation was used to determine the capacity to neutralize the DPPH radical:

$$Antioxidant\ Activity\,(\%AA) = \frac{absorbance\ of\ control - absorbance\ oftest}{absorbance\ of\ control} \times 100$$

The % AA was calculated and average readings were used to plot concentration versus anti-oxidant activity graph.

HPTLC analysis of Resveratrol, Curcumin and Gallic acid
Preparation of standards

All three compounds namely gallic acid, resveratrol and curcumin standard solution were prepared by weighing 1 mg separately and dissolving it in methanol. The volume was made up to 10 ml to obtain a working solution of 100 µg/ml.

Preparation of sample (polyherbal mixture solution)

The sample was prepared by weighing 100 mg of polyherbal mixture and the volume was made up to 10ml with methanol and was sonicated for 30 minutes. The filtrate was used for spotting on the TLC plate.

Chromatographic conditions

The samples were spotted as 6 mm wide band using a Hamilton microliter syringe of 100µL through a regulated nitrogen stream using a Camag Linomat V semi-automatic sample applicator on Merck precoated silica gel aluminium plate $60F_{254}$ (10×10 cm) with 250 µm thickness. Prior to applying the sample, the precoated TLC plate was prewashed with methanol and activated for 10 minutes at 110 °C. Development of method was done in a Camag twin trough chamber (10×10 cm) saturated previously with the mobile phase for 15 minutes. The optimized composition of mobile phase was Toluene: Ethyl acetate: Methanol: Formic acid (7:2:1:0.5 v/v/v/v). The process of densitometric scanning was carried out using the Camag TLC Scanner III, which was operated using the WinCATS software (version 1.44 CAMAG), at 269 nm wavelength.

Validation of HPTLC method
Linearity

Linearity was carried out by using working solution of gallic acid, resveratrol and curcumin separately. The working solution volume 2, 4, 6, 8, 10 μL were spotted on the HPTLC plate to get concentration in the range of 200–1000 ng/spot for gallic acid, resveratrol and curcumin respectively.

Accuracy

To evaluate the precision of the technique, the recovery of gallic acid, resveratrol, and curcumin in a mixture were determined using the standard addition method. In order to assess accuracy, predetermined amounts of gallic acid, resveratrol, and curcumin standard solutions were separately added at levels of 80 %, 100 %, and 120 % to the sample solution with a known quantity. The peak areas were measured, and the percent recovery and relative standard deviation were calculated.

Precision

Reproducibility of test application and determination of area of peak were performed using repetitions of similar concentration (600 ng/band of gallic acid, resveratrol and Curcumin) and were described using the relative standard deviation (%RSD). The intra- and inter-day variation for the determination of gallic acid, resveratrol and curcumin were carried out at concentration levels of 600 ng/band.

Limit of Detection (LOD) and Limit of Quantification (LOQ)

The LOD of a specific analytical method is the smallest quantity of analyte within a sample, which can be identified and not certainly quantified as an accurate value. LOD was determined as:

$$LOD = \frac{3.3 \times \text{standard deviation of } y \text{ intercept}}{\text{slope of calibration curve}}$$

The LOQ of as specific analytical method is the smallest quantity of analyte within a sample, which can be quantitatively assessed using adequate precision and accuracy. LOQ was determined as:

$$LOQ = \frac{10 \times \text{standard deviation of } y \text{ intercept}}{\text{slope of calibration curve}}$$

Robustness

By making small changes in the mobile phase volume and saturation time, the effect on R_f and area was studied. The robustness of the technique was examined at a concentration level of gallic acid, resveratrol and curcumin of 600 ng/spot.

Results and Discussion

Formulation of polyherbal mixture

In-house polyherbal mixture (PM) was prepared by mixing *Vitis vinifera, Panax ginseng, Withania somnifera, Tinospora chordifolia, Curcuma longa, Zingiber officinale* and *Glycyrrhiza glabra* extracts.

Quantitative phytochemical screening

The quantitative phytochemical analysis of polyherbal mixture was done by total phenolic content (TPC) and total flavonoid content (TFC). The total phenolic content in the PM was derived from a standard curve of gallic acid ranging from 50 to 500 μg/ml and using the equation $y = 0.009x + 0.0957$, 95 % CI [±0.00073] with correlation coefficient $r^2 = 0.9911$ (Fig. 2*a*). The average total phenolic content of the polyherbal mixture was found to be 212.1±7.407 mg of GAE/g of plant material. The total flavonoid content in the PM was calculated from a standard curve of rutin ranging from 100 to 500 μg/ml and using the equation $y = 0.0005x + 0.0038$, 95 % CI [±0.0067] with correlation coefficient $r^2 = 0.9904$ (Fig. 2*b*). The average total flavonoid content of the polyherbal mixture was found to be 133.06±1.333 mg of RU/g of plant material.

The activity to scavenge DPPH radical was evaluated by the reduction in the absorbance at 517 nm, which is dependent on the concentration ($n = 3$). Percent anti-oxidant activity for 50 μg/ml of polyherbal mixture was found to be 97.22 % which was higher than standard ascorbic acid of same concentration. The IC_{50} value of the polyherbal mixture was found to be 3.83 μg/ml which indicate that it has greater antioxidant properties than the standard ascorbic acid (Fig. 3).

$y = 0.000x + 0.095$
$R^2 = 0.991$
95 % CI [± 0.0021]

(a)

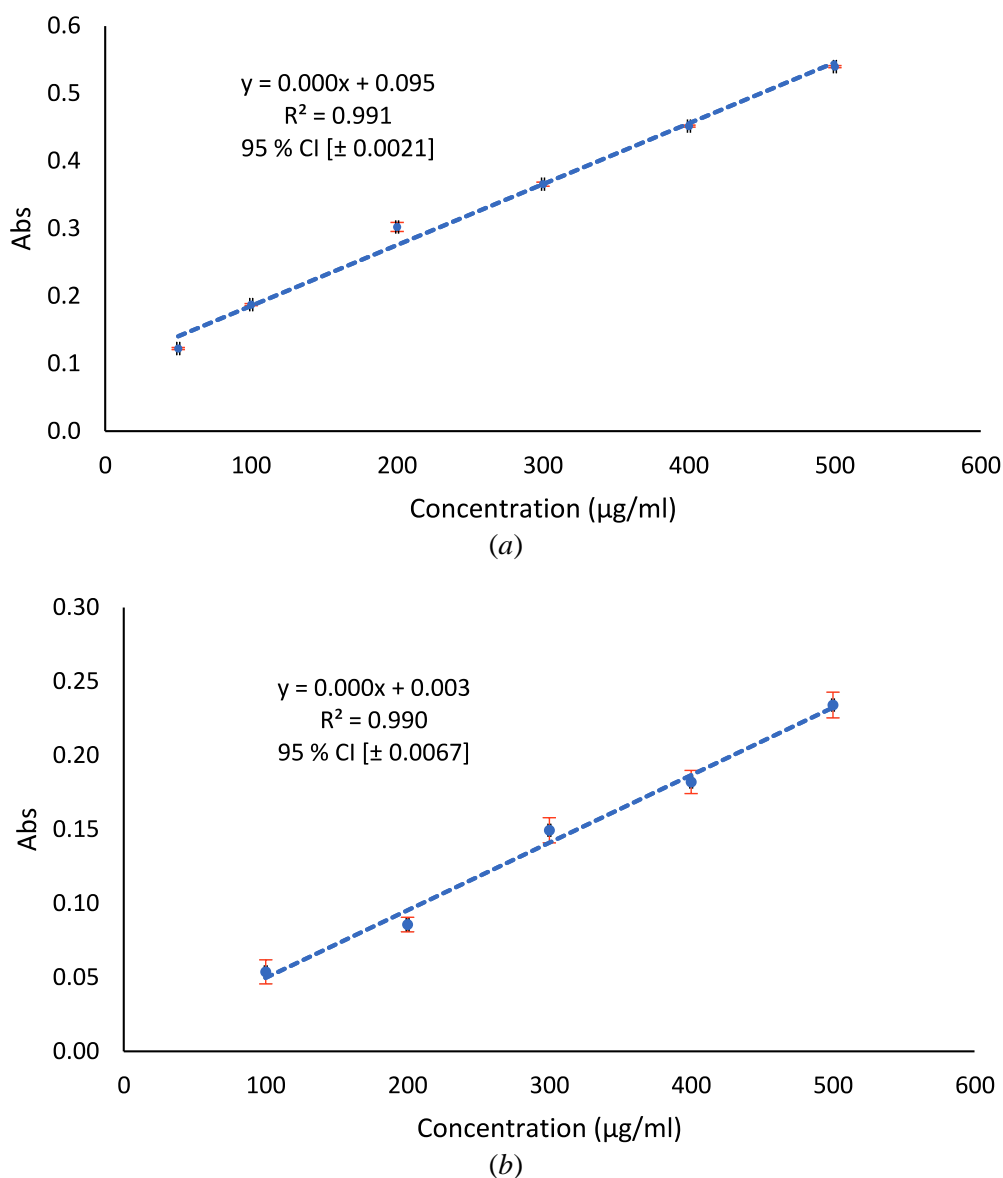$y = 0.000x + 0.003$
$R^2 = 0.990$
95 % CI [± 0.0067]

(b)

Figure 2. Determination of (a) Total Phenolic Content (TPC), (b) Total Flavonoid Content (TFC)
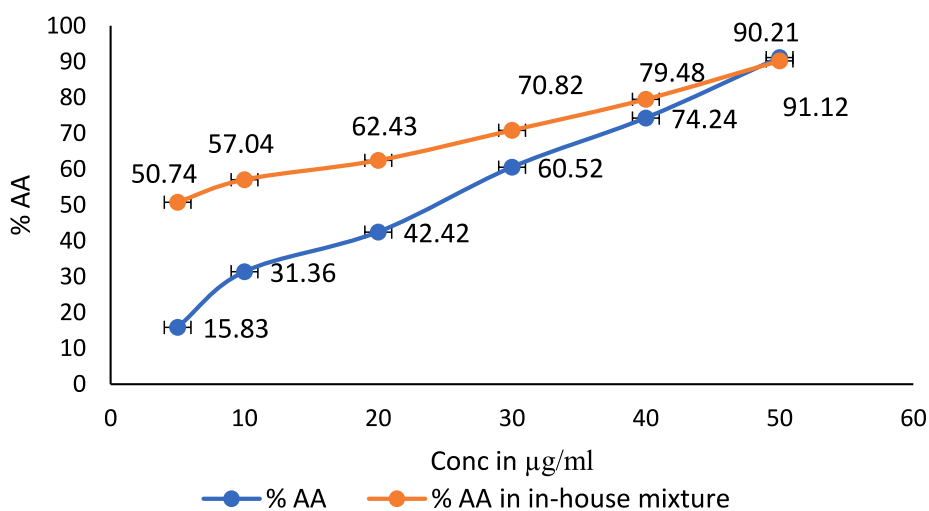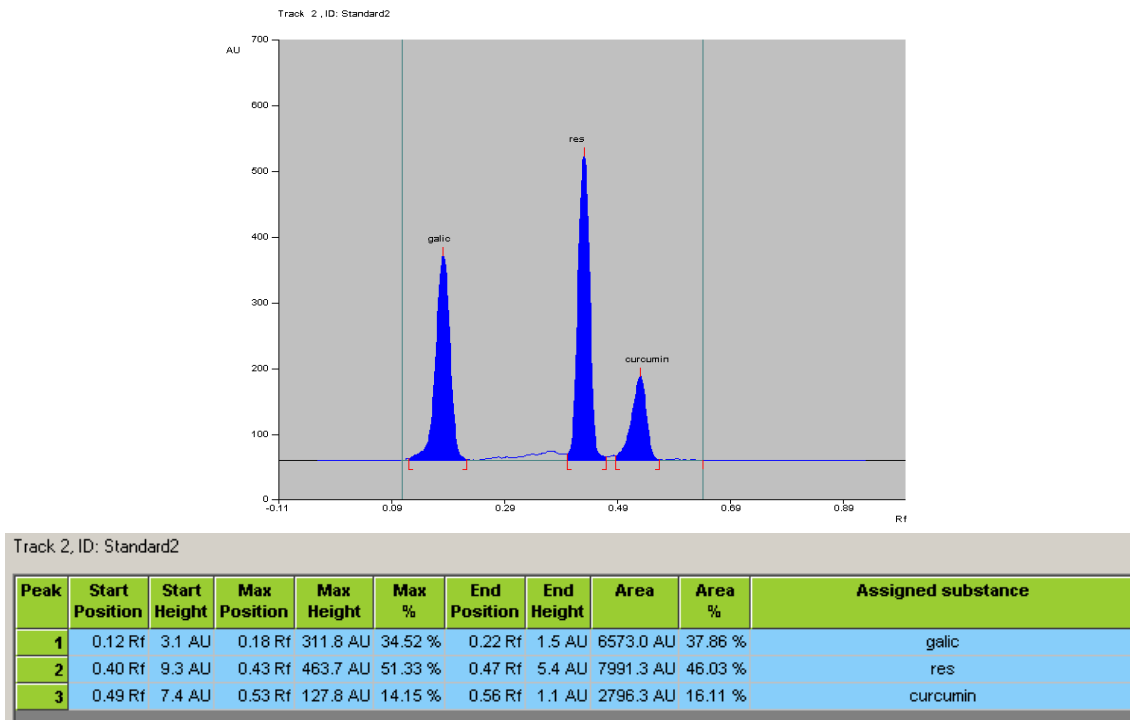

Figure 3 Determination of percentage anti-oxidant activity (% AA)

HPTLC analysis of resveratrol, curcumin and gallic acid

The HPTLC procedure was optimized to quantify curcumin, gallic acid and resveratrol in the polyherbal mixture. The mobile phase toluene: ethyl acetate: methanol: formic acid (7:2:1:0.5 v/v/v/v) gave good resolution with $R_f = 0.18$ for gallic acid, $R_f = 0.43$ for resveratrol and $R_f = 0.53$ for curcumin (Fig. 4*a*). Under the optimized chromatographic condition, the polyherbal mixture showed sharp peaks and good separation when scanned at 269 nm (Fig. 4*b*). Overlay UV spectra of matching R_f values of standard curcumin, gallic acid and resveratrol and peaks of polyherbal mixture confirmed their presence in polyherbal mixture (Fig. 5).

Track 2, ID: Standard2

Peak	Start Position	Start Height	Max Position	Max Height	Max %	End Position	End Height	Area	Area %	Assigned substance
1	0.12 Rf	3.1 AU	0.18 Rf	311.8 AU	34.52 %	0.22 Rf	1.5 AU	6573.0 AU	37.86 %	galic
2	0.40 Rf	9.3 AU	0.43 Rf	463.7 AU	51.33 %	0.47 Rf	5.4 AU	7991.3 AU	46.03 %	res
3	0.49 Rf	7.4 AU	0.53 Rf	127.8 AU	14.15 %	0.56 Rf	1.1 AU	2796.3 AU	16.11 %	curcumin

(*a*) Densitogram of standard curcumin, gallic acid and resveratrol

Track 4, ID: Standard3

Peak	Start Position	Start Height	Max Position	Max Height	Max %	End Position	End Height	Area	Area %
1	0.15 Rf	2.1 AU	0.22 Rf	566.5 AU	37.57 %	0.26 Rf	9.5 AU	15472.1 AU	42.82 %
2	0.37 Rf	6.7 AU	0.40 Rf	16.5 AU	1.10 %	0.40 Rf	15.3 AU	319.7 AU	0.88 %
3	0.40 Rf	15.4 AU	0.46 Rf	388.2 AU	25.74 %	0.48 Rf	38.7 AU	7529.3 AU	20.84 %
4	0.48 Rf	39.4 AU	0.54 Rf	536.5 AU	35.59 %	0.57 Rf	6.0 AU	12814.9 AU	35.46 %
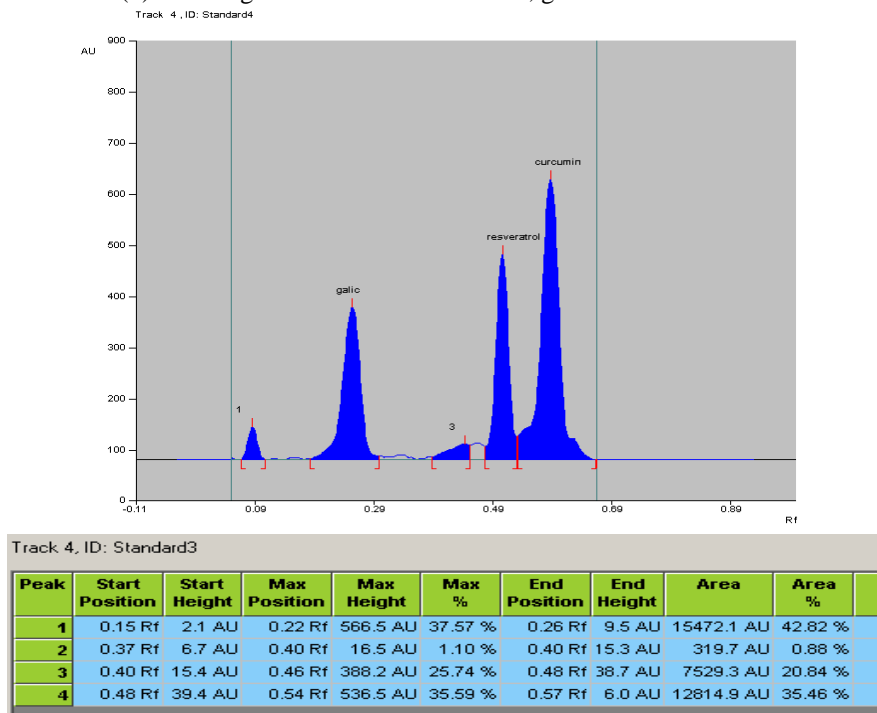
(*b*) Densitogram of polyherbal mixture indicating curcumin, gallic acid and resveratrol

Figure 4.
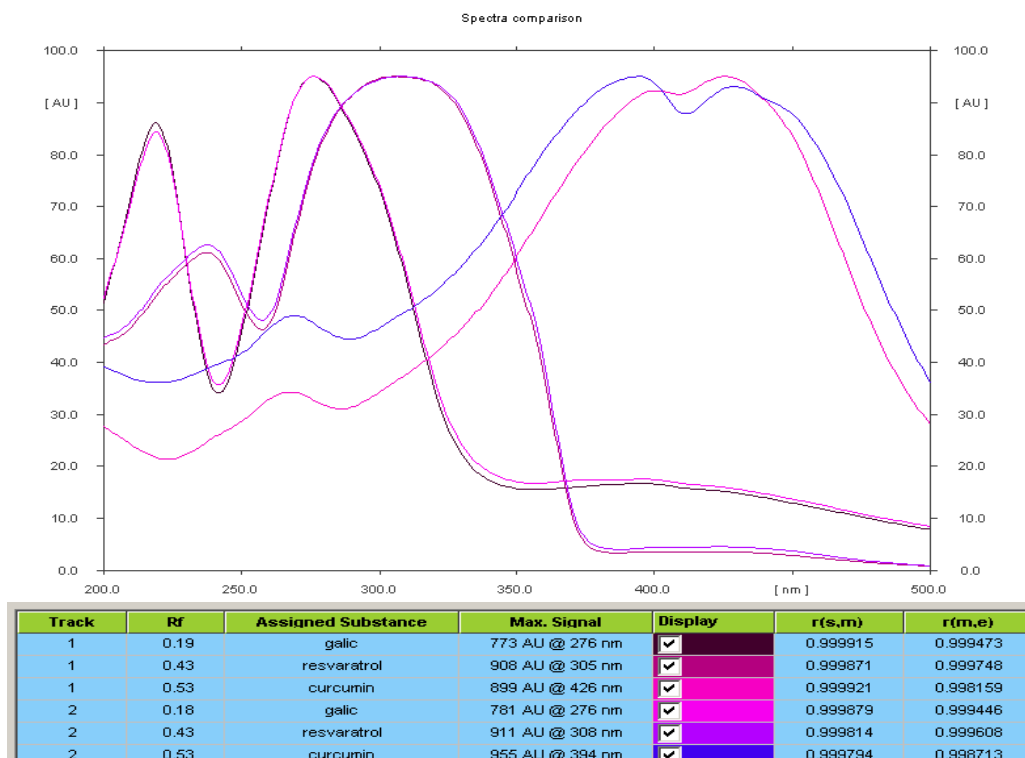
Figure 5. Overlay spectra of gallic acid, resveratrol and curcumin

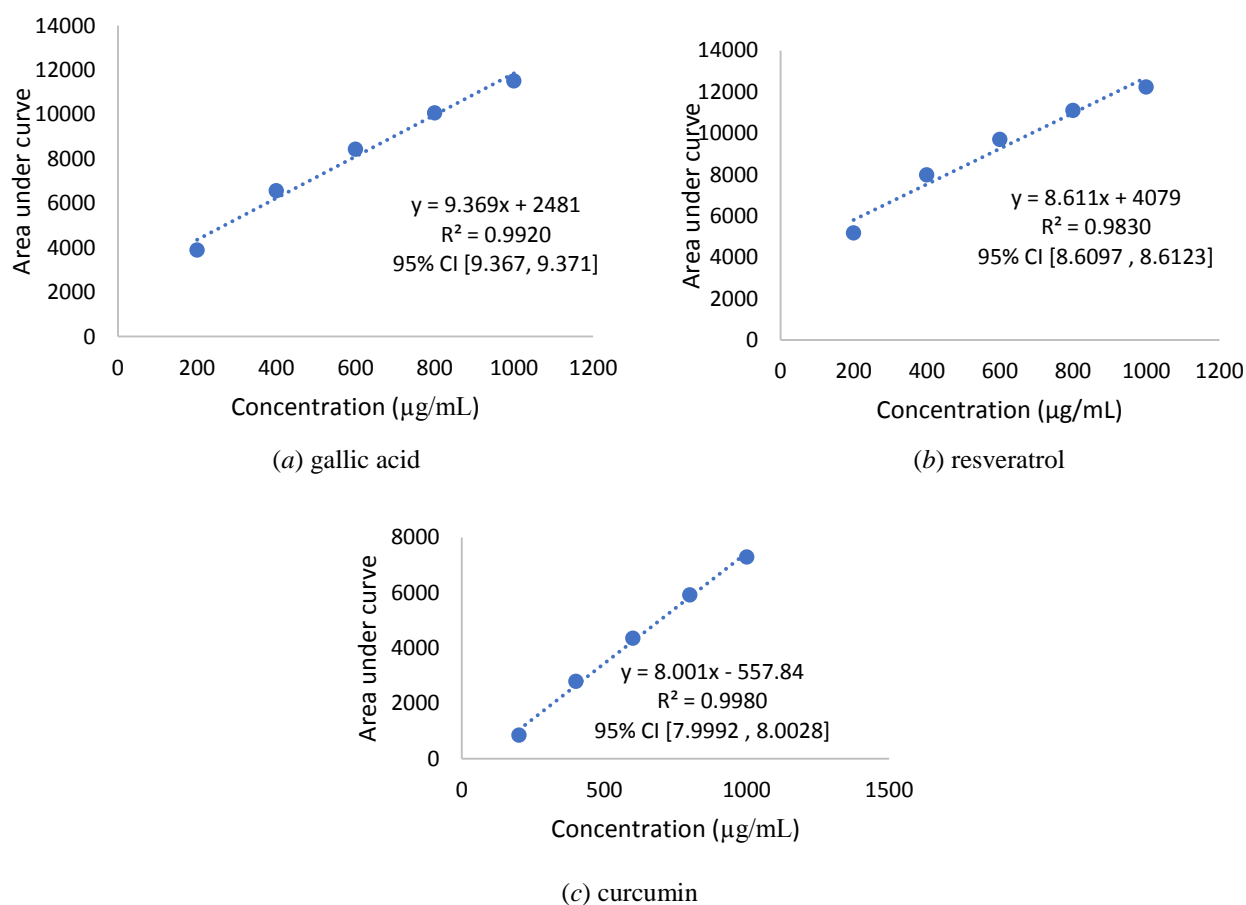(*a*) gallic acid

(*b*) resveratrol

(*c*) curcumin

Figure 6. Calibration curve of standards

Validation of developed HPTLC method

The linearity graph was plotted using different concentrations of gallic acid, resveratrol and curcumin. The regression coefficient value (r^2) was observed to be 0.99209 for gallic acid, 0.98300 for resveratrol and 0.99802 for curcumin from the graph (Table, Fig. 6).

The proposed HPTLC techniques have been verified for intra- and inter-day variations. The percent relative standard deviations (%RSDs) values were determined to be 0.0073, 0.0076, 0.0161 (for intra-day) and 0.0062, 0.0058, 0.0151 (for inter-day) for gallic acid, resveratrol and curcumin respectively. This indicates that the method was precise. Recovery tests were conducted at three distinct concentration levels 80, 100, and 120% to examine the method's accuracy. The lowest concentration at which the standards solution can be consistently identified was recorded as 0.30 µg/spot, 0.26 µg/spot, 0.24 µg/spot and the lowest analyte concentration at which it can be consistently measured was found to be 0.91 µg/band, 0.79 µg/band, 0.75 µg/band for gallic acid, resveratrol and curcumin respectively. By making minor adjustments to the mobile phase volume and saturation duration, the robustness of the new method was tested, where % RSD was found to be in the limit < 2 %.

T a b l e

Validation parameters of the developed HPTLC method

Parameters	Results		
	Gallic acid	**Resveratrol**	**Curcumin**
Linearity	Y = 9.369x +2481	Y = 8.611x + 4079	Y = 8.001x − 557.8
Slope	9.369	8.611	8.001
Y-intercept	2481	4079	-557.8
Correlation Coefficient	0.99209	0.98300	0.99802
R_f	0.18	0.43	0.53
Level of accuracy	**% Recovery**		
80 %	100.1604 ± 0.01	100.0249 ± 0.06	101.1639 ± 1.55
100 %	100.0004 ± 0.01	99.99715 ± 0.002	100.4646 ± 0.588
120 %	99.93298 ± 0.02	99.99556 ± 0.01	100.1058 ± 0.06
Precision	**%RSD**		
Intra day	0.0073 ± 0.61	0.0076 ± 0.74	0.0161 ± 0.69
Inter day	0.0062±0.51	0.0058 ± 0.56	0.0151 ± 0.65
LOD (ng/band)	0.30 ± 0.05	0.26 ± 0.04	0.24 ± 0.053
LOQ (ng/band)	0.91 ± 0.09	0.79 ± 0.05	0.75 ± 0.08
Robustness	**%RSD**		
Mobile phase volume (±1 ml)	0.0031 ± 0.26	0.0037 ± 0.36	0.0080 ± 0.34
Saturation time (±5 min)	0.0088 ± 0.74	0.0033 ± 0.32	0.0060 ± 0.26

Conclusions

This research focused on the development and validation of an HPTLC method for the simultaneous quantification of curcumin, gallic acid, and resveratrol in a polyherbal mixture, along with assessing its Total Phenolic Content (TPC), Total Flavonoid Content (TFC), and antioxidant potential using the DPPH assay. The findings indicate that the polyherbal mixture is rich in TPC, measuring 212.1 ± 7.407 mg gallic acid equivalent (GAE) per gram of plant material, and TFC, which was found to be 133.06 ± 1.333 rutin equivalent (RU) per gram of plant material. The DPPH assay demonstrated strong antioxidant activity with an IC_{50} value of 3.83 µg/ml.

Furthermore, the HPTLC method was meticulously optimized, providing excellent resolution for gallic acid, resveratrol, and curcumin, with corresponding R_f values of 0.18, 0.43, and 0.53. The method exhibited strong linearity ($r^2 > 0.99$) over a concentration range of 200–1000 ng/band for all three compounds. Precision studies confirmed the method's reproducibility with low Relative Standard Deviation (RSD) values below 2 % for both intra-day and inter-day analyses.

This HPTLC method stands out for its simplicity, accuracy, precision, and cost-effectiveness, making it suitable for routine quality control analysis. These results shed light on the potential applications of the polyherbal mixture in various therapeutic contexts, underscoring its robust phytochemical profile and potent

antioxidant properties, further supporting its use in herbal medicine and quality control assessments. This research contributes to the growing importance of polyherbal formulations in the field of herbal medicine.

Author Information*

*The authors' names are presented in the following order: First Name, Middle Name and Last Name

Sejal Prakash Gandhi — Assistant Professor, Department of Pharmaceutical Chemistry, Dr. D.Y. Patil Institute of Pharmaceutical Sciences and Research, Pimpri, Pune, Maharashtra, 411018, India; e-mail: sejal.gandhi@dypvp.edu.in; https://orcid.org/0000-0002-7079-1886

Gresi Devidas Mate — Student, Department of Pharmaceutical Quality Assurance, Dr. D.Y. Patil Institute of Pharmaceutical Sciences and Research, Pimpri, Pune, Maharashtra, 411018, India; e-mail: gresimate959@gmail.com

Dheeraj H. Nagore — Assistant Professor, Department of Pharmacognosy, Dr. D.Y. Patil Institute of Pharmaceutical Sciences and Research, Pimpri, Pune, Maharashtra, 411018, India; e-mail: nagoredheeraj@gmail.com; https://orcid.org/0000-0002-6804-6262

Sohan Satyanarayan Chitlange — Principal, Department of Pharmaceutical Chemistry, Dr. D.Y. Patil Institute of Pharmaceutical Sciences and Research, Pimpri, Pune, 411018, Maharashtra, India; e-mail: sohanchitlange@rediffmail.com; https://orcid.org/0000-0002-9355-3303

Author Contributions

The manuscript was written through contributions of all authors. All authors have given approval to the final version of the manuscript. CRediT: **Sejal Prakash Gandhi** conceptualization, data curation, validation, visualization, manuscript writing; **Gresi Devidas Mate** data curation, formal analysis, investigation, methodology, visualization; **Dheeraj Nagore** data curation, formal analysis, manuscript writing & editing; **Sohan Satyanarayan Chitlange** conceptualization, resources, supervision, validation, manuscript editing.

Conflicts of Interest

The authors declare no conflict of interest.

References

1   Ali, A., Qadir, A., Khan, M.A., Al-Otaibi, F.O., Khan, S., & Abdin, M.Z. (2017). A Simple Validated HPTLC Method for Simultaneous Analysis of Colchicine and Gallic Acid in Polyherbal Formulation: Habb-E-Irqun-Nisha. *Food Analytical Methods*, *10*(9), 2934–2942. https://doi.org/10.1007/s12161-017-0835-0

2   Parasuraman, S., Thing, G.S., & Dhanaraj, S.A. (2014). Polyherbal formulation: Concept of ayurveda. *Pharmacognosy reviews*, *8*(16), 73. https://doi.org/10.4103/0973-7847.134229

3   Pillai, D. & Pandita, N. (2016). Validated high performance thin layer chromatography method for the quantification of bioactive marker compounds in Draksharishta, an ayurvedic polyherbal formulation. *Revista Brasileira de Farmacognosia*, 26, 558–563. https://doi.org/10.1016/j.bjp.2016.03.015

4   Kharat, S., Namdeo, A., & Mehta, P. (2017). Development and validation of HPTLC method for simultaneous estimation of curcumin and galangin in polyherbal capsule dosage form. *Journal of Taibah University for Science*, *11*(5), 775–781. https://doi.org/10.1016/j.jtusci.2016.10.004

5   Zhang, H., Abid, S., Ahn, J.C., Mathiyalagan, R., Kim, Y.J., Yang, D.C., & Wang, Y. (2020). Characteristics of Panax ginseng cultivars in Korea and China. *Molecules*, *25*(11), 2635. https://doi.org/10.3390/molecules25112635

6   Pascual-Martı, M.C., Salvador, A., Chafer, A., & Berna, A. (2001). Supercritical fluid extraction of resveratrol from grape skin of Vitis vinifera and determination by HPLC. *Talanta*, *54*(4), 735–740. https://doi.org/10.1016/S0039-9140(01)00319-8

7   Meyer, A.S., Yi, O.S., Pearson, D.A., Waterhouse, A.L., & Frankel, E.N. (1997). Inhibition of human low-density lipoprotein oxidation in relation to composition of phenolic antioxidants in grapes (Vitis vinifera). *Journal of Agricultural and Food Chemistry*, *45*(5), 1638–1643. https://doi.org/10.1021/jf960721a

8   Choi, K.T. (2008). Botanical characteristics, pharmacological effects and medicinal components of Korean Panax ginseng CA Meyer. *Acta Pharmacologica Sinica*, *29*(9), 1109–1118. https://doi.org/10.1111/j.1745-7254.2008.00869.x

9   Omosa, L.K., Midiwo, J.O., & Kuete, V. (2017). Curcuma longa. Medicinal Spices and Vegetables from Africa, 425–435. https://doi.org/10.1016/b978-0-12-809286-6.00019-4

10   Akbar, M.U., Rehman, K., Zia, K.M., Qadir, M.I., Akash, M.S. H., & Ibrahim, M. (2018). Critical Review on Curcumin as a Therapeutic Agent: From Traditional Herbal Medicine to an Ideal Therapeutic Agent. *Critical Reviews in Eukaryotic Gene Expression*, *28*(1), 17–24. https://doi.org/10.1615/critreveukaryotgeneexpr.2018020088

11   Öztürk, M., Altay, V., Hakeem, K.R., & Akçiçek, E. (2017). Liquorice: from botany to phytochemistry. In *SpringerBriefs in Plant Science.* Springer International Publishing. https://doi.org/10.1007/978-3-319-74240-3

12   Sonawane, S.D., Nirmal, S.A., Patil, A.N., & Pattan, S.R. (2011). Development and validation of HPTLC method to detect curcumin and gallic acid in polyherbal formulation. *Journal of liquid chromatography & related technologies, 34*(20), 2664–2673. https://doi.org/10.1080/10826076.2011.593221

13   Vaykole, A.M., Nirmal, S.A., Jadhav, R.S., & Pattan, S.R. (2014). Development and validation of HPTLC method to detect curcumin, piperine, and boswellic acid in polyherbal transdermal patch. *Journal of Liquid Chromatography & Related Technologies, 37*(3), 367–378. https://doi.org/10.1080/10826076.2012.745141

14   Kaul, N., Agrawal, H., Patil, B., Kakad, A., & Dhaneshwar, S.R. (2005). Application of stability-indicating HPTLC method for quantitative determination of metadoxine in pharmaceutical dosage form. *Il Farmaco*, *60*(4), 351–360. https://doi.org/10.1016/j.farmac.2005.01.001

15   Balaton Symposium 2009. (2010). *Journal of Planar Chromatography – Modern TLC*, *23*(3), 171–172. https://doi.org/10.1556/jpc.23.2010.3.00

16   Amir, M., Mujeeb, M., Ahmad, S., Akhtar, M., & Ashraf, K. (2013). Design expert-supported development and validation of HPTLC method: an application in simultaneous estimation of quercetin and rutin in Punica granatum, Tamarindus indica and Prunus domestica. *Pharmaceutical Methods, 4*(2), 62–67. https://doi.org/10.1016/j.phme.2013.12.004

17   Nasr, M. & Abdel Rahman, M.H. (2019). Simultaneous determination of curcumin and resveratrol in lipidic nanoemulsion formulation and rat plasma using HPLC: Optimization and application to real samples. *Journal of AOAC International, 102*(4), 1095–1101. https://doi.org/10.5740/jaoacint.18-0269

18   Gupta, M. & Kaur, A. (2019). Method development and validation for simultaneous estimation of resveratrol and gallic acid by RP-HPLC. *International Journal of Pharmaceutical, Chemical & Biological Sciences*, *9*(1).

19   Bharskar, G., Mankar, S., & Siddheshwar, S. (2022). Analytical methods for estimation of curcumin in bulk, pharmaceutical formulation and in biological samples. *Asian Journal of Pharmaceutical Analysis, 12*(2). https://doi.org/10.52711/2231-5675.2022.00025

20   Shaikh, M., & Jadhav, A.P. (2020). Development and Validation of RP-HPLC Method for Simultaneous Estimation of Gallic Acid, Curcumin and Piperine in an Ayurvedic Formulation. *International Journal of Pharmacy and Pharmaceutical Sciences,* 81–86. https://doi.org/10.22159/ijpps.2020v12i6.33801

21   ICH Validation Guidelines (2005). Validation of analytical procedures: text and methodology. *Q2 (R1)*, *1*(20), 05. Retrieved from https://database.ich.org/sites/default/files/Q2%28R1%29%20Guideline.pdf

22   Vl, S. (1999). Analysis of total phenols and other oxidation substrates and antioxidants by means of Folin-Ciocalteu reagent. *Methods in Enzymology, 299*, 152–178. https://doi.org/10.1016/S0076-6879(99)99017-1

23   Zhishen, J., Mengcheng, T., & Jianming, W. (1999). The determination of flavonoid contents in mulberry and their scavenging effects on superoxide radicals. *Food chemistry, 64*(4), 555–559. https://doi.org/10.1016/S0308-8146(98)00102-2

24   Kizito, I.G., & Mohammed, K. (2022). Phytochemical analysis, antimicrobial and antioxidant activities of leaf extract of Vernonia tigna Klatt (Asteraceae). *World Journal of Advanced Pharmaceutical and Life Sciences*, *3*(2), 016–023. https://doi.org/10.53346/wjapls.2022.3.2.0045

25   Thaipong, K., Boonprakob, U., Crosby, K., Cisneros-Zevallos, L., & Byrne, D. H. (2006). Comparison of ABTS, DPPH, FRAP, and ORAC assays for estimating antioxidant activity from guava fruit extracts. *Journal of Food Composition and Analysis, 19*(6-7), 669–675. https://doi.org/10.1016/j.jfca.2006.01.003

CHEMICAL TECHNOLOGY

Sveta A. Dzhumadullaeva[1*] , Abduali B. Baeshov[2]

[1]Khoja Akhmet Yassawi International Kazakh-Turkish University, Kazakhstan;
[2]D.V. Sokolsky Institute of Fuel, Catalysis and Electrochemistry, Almaty, Kazakhstan
(*Corresponding autor 's e-mail: sveta.jumadullayeva@ayu.edu.kz)

An Efficient Ion-Exchange Resin Catalysts
for the Liquid-Phase Selective Hydrazinolysis of Succinic Acid

Dicarboxylic acid dihydrazides are widely used as pharmaceutical intermediates, plant growth regulators, water-based coating additives, epoxy crosslinking agents. Dihydrazides are prepared by adding hydrazine hydrate to an acid halides and diesters. In this work the hydrazinolysis of succinic acid was studied using various ion exchange resins as catalysts, and the optimum conditions and the reaction mechanism were identified. Analysis of the initial reagents and the target product were performed out using photocolorimetric and IR spectroscopic methods, the composition of the target product was determined by elemental analysis. Hydrazinolysis of succinic acid were performed in aqueous medium in the temperature 90 °C for 3 h. Succinic acid conversion was 82–95 %, and the succiniyldihydrazide yield 61–93 %. It has been shown the efficient catalysts for the hydrazinolysis of succinic acid are AV-17-8, AN-31 and AN-1 anion exchangers. The highest succinyldihydrazide yield (93 %) was obtained with anion exchanger AV-17-8. On the basis of IR spectroscopic studies, a plausible process mechanism was suggested. A probable mechanism of the process with the formation of supramolecular complexes with the participation of substrates and fixed polymer-bound quaternary ammonium and hydroxyl ions of the anion exchanger was proposed. Thus, the most efficient method of succinic acid dihydrazide preparation has been proposed in comparison with known methods.

Keywords: succinic acid dihydrazide, hydrazinolysis, heterogenious catalyst, ion exchange resins, supramolecular complexes.

Introduction

Hydrazide derivatives of dicarboxylic acids are widely used as drugs with antimicrobial, antifungal, antibacterial, and antitubercular activity [1–6]. Among the substituted hydrazides of succinic acid, compounds with hypoglycemic and hypertensive effects were found [7]. Metal dihydrazide complex compounds as ecologycally safe chemical compounds are applied in agriculture as efficient plant growth regulating chemicals [8]. For example, succinic acid 2,2-dimethylhydrazide (Daminoside) is a well known compound used as an active ingredient in plant growth regulating compositions [9, 10]. Dihydrazides are added to the composition of epoxy in varnishes and nickel corrosion inhibitors [11, 12]. Succinyldihydrazide is water-based coating additive, epoxy crosslinking agent, aldehyde remover, textile additive and biochemical reagent, which can be mainly used in laboratory organic synthesis process and chemical and pharmaceutical production research and development process [1–5, 11]. Many dihydrazides are used to recover metal ions from industrial waste water as reagents to form anti-corrosive metal coatings [13].

The preparation of dihydrazides from the corresponding dicarboxylic acids did not give the desired results, so they were synthesized by hydrazinolysis of various derivatives of dicarboxylic acids (acid halides and anhydrides, diesters) in medium of organic solvents [3, 14]. According to this method [15], the obtaining

succinyldihydrazide is carried out through the esterification of corresponding acid using concentrated sulfuric acid, followed hydrazinolysis of the resulting dimethyl succinate in methanol (Sheme 1):
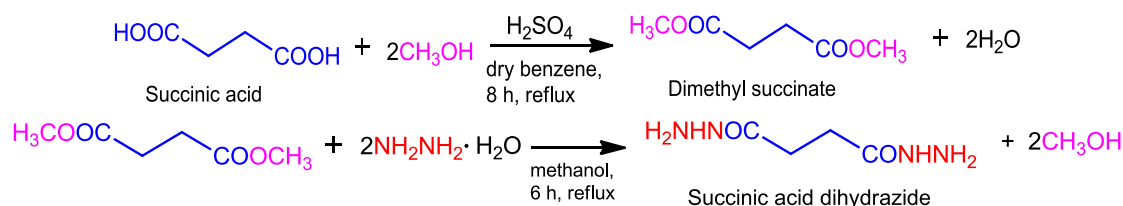
Scheme 1. Synthesis of dimethyl succinate under acid catalysis conditions and hydrazinolysis of dimethyl succinate

The synthesis of dimethyl succinate is demanding process. The reaction is carried out in large excess of absolute methanol (therefore, its absoluization is necessary, which requires the expenditure of electricity and reagents). The use of sulfuric acid as a catalyst experiences strong corrosivity, large environmental hazard, complex side reaction, low yield and the like. Second reaction step — hydrazinolysis of dimethyl succinate also has certain disadvantages: hydrazine hydrate concentration used in the method is 10 times of that of esters, the general reaction time is up to 14 hours, and the yield of succinicdihydrazide is only 89 %.

Therefore, the search for an efficient method for preparing of dihydrazides with low production cost, high conversion rate and few side reactions is an urgent problem.

We have previously shown the possibility of using some cation exchange resins as catalysts for the hydrazinolysis of oxalic and maleic acids with yields of the corresponding hydrazides of 63 and 90 % [16]. Using kinetic and IR spectroscopic studies, a probable mechanism of the process was proposed that involved hydrogen ions of the polymer catalyst. However, there is no information in the literature about the use and catalytic properties of ion exchangers in the synthesis of other dihydrazides and about the reaction mechanism. Compared with inorganic catalysts, ion exchange resins exhibit excellent catalytic performance and are easily regenerated. The use of a solid ion exchange resin as catalyst has a number of advantages: the catalyst is easily separated from the reaction products, does not require neutralization and concentration, has high selectivity with respect to the target product, can be used many times after appropriate processing, and does not corrode the industrial equipment.

As a continuation of work on the exploration of novel heterogenious catalysts for the preparation of acid dihydrazides, in the present paper was studied the reaction between succinic acid and aqueous hydrazine in the presence of ion exchanger catalysts, and also identified the optimum conditions and the probable reaction mechanism using the IR spectroscopic method.

Experimental

Materials and Methods

For preparation of succinic acid dihydrazide, commercial hydrazine hydrate and succinic acid used were reagent grade without further purification. Hydrazine hydrate (purity 99.9 %) was provided by Ural Industrial Chemical Plant, Russia. Succinic acid (chemically pure) was provided by ChemBio Service, Russia. The solvents were purified and absolutized according to standard methods. The following commercial ion exchange resin were used as catalysts: hyghly basic anion exchanger AV-17-8 (grain size 0.4–0.6 mm), weakly basic anion exchangers AN-31 (0.4–2.0 mm) and AN-1 (0.4–2.0 mm), strongly acidic sulfonic acid cation exchanger KU-2-8 (0.40–0.55 mm), and phosphoric acid cation exchanger KRF-10 P (0.5–1.0 mm), produced by Olaine Chemical Plant Biolar, Latvia. They were conditioned and converted into the H^+/OH^- form by a standard method [17]. The exchange capacity of ion exchangers was measured under static conditions by a standard method [18]. Exchange capacity of the ion exchanger, mg-equiv/g: AV-17-8 — 4.2; AN-31 — 3.8; AN-1 — 3.6; KU-2-8 — 3.0; KRF-10P — 3.2.

C, H and N elemental analyses were performed with a X-Calibur elemental analyzer (Xenemetrix Ltd, Israel). The photocolorimetric analyses of succinic acid and corresponding dihydrazide were carried out on a Fluorat-02-5M device (Lumex, Russia) [19]. The course of reactions and the purity of the target product were monitored by TLC on Merck Silica gel 60G F254 plates. IR spectroscopic studies of initial reagents and the reaction product have been carried out on an Impact-410 FT-IR spectrometer (Nicolet, USA) as KBr pellets in the 4000–400 cm^{-1} region.

*General Procedure for the Preparation of Succinic acid Dihydrazide*

Succinic acid (0.85 mmol), hydrazine hydrate (1.5–2.6 mmol) and 1.0–2.5 g an air-dry polymer catalyst were mixed and heated in 8–20 ml of water for 1.5–4.0 h at 90 °C. Then, the final mixture was cooled and the catalyst was separated by filtration. The aqueous solution was evaporated, and the dry residue was recristallized from absolute ethanol.

Yield: 93 % , m.p. 169–173 °C. IR (KBr, ν, cm^{-1}): 3180, 3205, 3298, 3318, 1575, 1537 (N–H), 1632 (C=O), 1185, 1124, 1089 (C–N), 2880, 2928, 2966, 2651, 1461, 1423, 1396 (C–H),1295, 1273, 1240, 664 (CH$_2$), 953, 925 (N–N), cm^{-1}. Elemental analysis: Found, %: C, 32.85; H, 6.82; N, 38.33. C$_4$H$_{10}$N$_4$O$_2$. Calculated, %: C, 32.84; H, 6.84; N, 38.32.

Results and Discussion

Chemistry. Investigation of Catalytic Activity

We found that succinic acid (SA) readily reacted with hydrazine hydrate (HH) on the catalyst, to yield succinyldihydrazide (SADH) (Scheme 2):
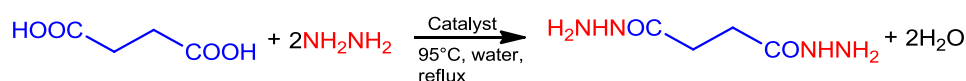
Scheme 2 Synthesis of succinic acid dihydrazide

In addition to succinyldihydrazide, monohydrazide succinic acid (HOOCCH$_2$CH$_2$CONHNH$_2$) was obtained in small quantities. All tested catalysts are active in this process: the conversion of SA is 82–95 %, and the SADH yield is 61–93 % (Fig. 1). The highest SADH yield (72–93 %) with a SA-to-dihydrazide conversion selectivity of 96–97.4 % is obtained with AV-17-8, AN-31 and AN-1. However, the polymer catalysts KU-2-8 and KRF-10P, which have the properties of solid acids, did not show sufficient activity in the process under study.
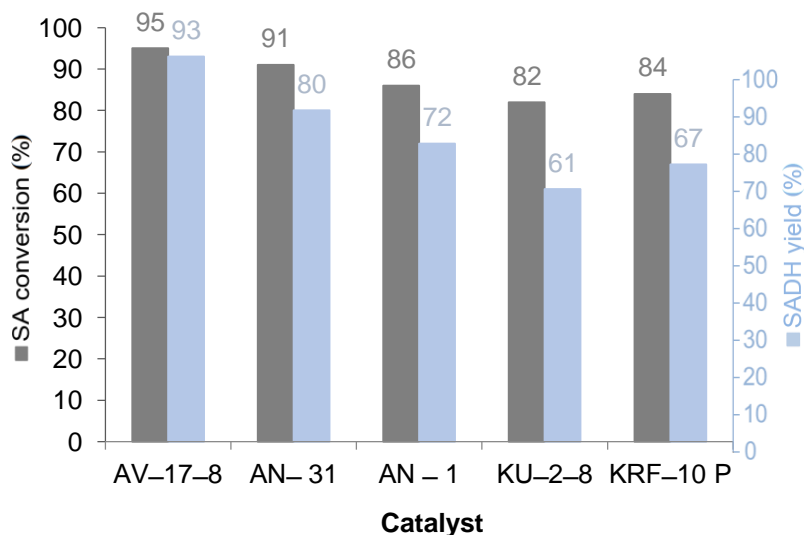
Reaction conditions: SA:HH:Catalyst:H$_2$O mass ratio of 1:0.82:2:8, 90 °C, 3 h

Figure 1. Comparison of the catalytic activity of ion exchangers in the reaction succinic acid with hydrazine*

In addition to being composition and structure dependend, the catalytic properties of the ion exangers are strongly influenced by the operating conditions. When studying the influence of various factors (duration of the experiment, concentration of substrates and catalyst) on the process, it was found that in the case of using AV-17-8 (OH), the yield of SADH reaches 93 % (Table). The optimal conditions for preparation SADH from SA at 90 °C were identified: contact time 3 h, SA:HH:Catalyst:H$_2$O mass ratios of 1:0.82:2:8.

SADH synthesis over the catalyst AV-17-8 (OH) at 90 °C

SA:HH:Cat:H_2O	Time, h	SADH yield,%	SA:HH:Cat:H_2O	Time, h	SADH yield, %
1:0.84:2:8	1.5	59	1:0.76:2:8	3.0	73
1:0.84:2:8	2.5	82	1:1.05:2:8	3.0	90
1:0.84:2:8	3.0	93	1:1.34:2:8	3.0	89
1:0.84:2:8	4.0	89	1:0.84:2:8	2.0	68
1:0.84:1.0:8	3.0	64	1:0.84:2:10	3.0	91
1:0.84:1.5:8	3.0	80	1:0.84:2:12	3.0	85
1:0.84:2.5:8	3.0	83	1:0.84:2:20	3.0	82

IR Spectroscopy. Proposed Reaction Mechanism

Basing on the reference information it could be suggested that hydrazinolysis of SA on the catalyst AV-17-8 (OH) ion-exchange resin occurred via a heterogeneous catalytic mechanism in which the polymerbound quaternary ammonium ions and OH ions are responsible for the process [20] (Sheme 3):
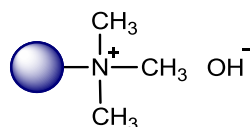
Sheme 3. The active site of catalyst AV-17-8 (OH)

Depending on the nature of the active center of the ion exchanger, non-covalent interaction (electrostatic, hydrogen bonding, Van der Waals forces) can occur, resulting in the formation of supramolecules – complex associates consisting of two or more molecules held together by intermolecular forces. Based on the data on the IR spectra of the AV-17-8 anion exchanger after interaction with succinic acid and hydrazine, various aggregate supramolecular complexes of adsorbed molecules with active centers of the ion-exchange resin were found [21].

In the spectrum characterizing the interactions of succinic acid with AV-17-8 (OH), there is no very intence absorbtion bands at 1739 cm^{-1} that is due to the stretching vibrations of the C=O group and an absorbtion band at 907 cm^{-1} assigned to the out-of-plane deformation vibration of the OH group of succinic acid (Fig. 2).
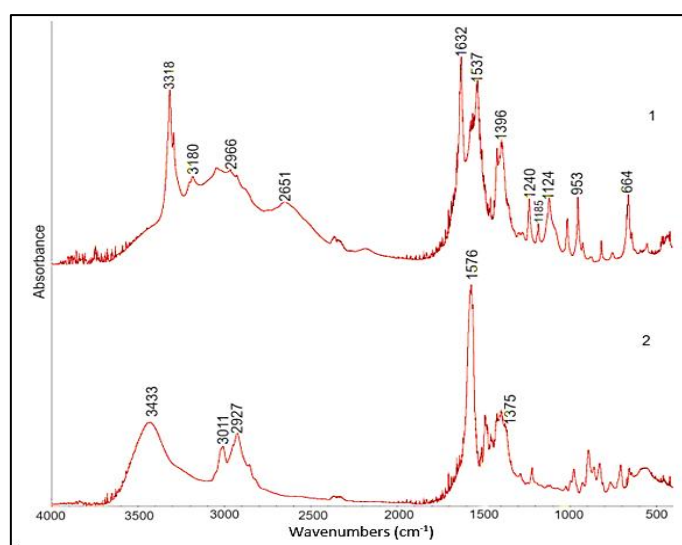

Figure 2. IR absorbtion spectra of (1) succinic dihydrazide
and (2) the interaction product of succinic acid with the catalyst

In the range of 3800–2500 cm^{-1}, a broad, intense band with maxima at 3433, 3011 and 2927 cm^{-1} is observed, the bands with frequencies of 2927, 2880, 1421 and 1398 cm^{-1} refer to the stretching and bending vibrations of the C–H groups. It was found that the adsorbtion of succinic acid is carried out due to yield a hydrogen bond with hydroxyl groups located on the surface of the catalyst [22]. Along with the characteristic anion exchanger bands, intense absorbtion bands at 1375 and 1576 cm^{-1} appear, which can be assigned to symmetric and antisymmetric vibrations of the carboxylat group — COO$^-$ which became the counterions of the fixed cations of the resin (intermediate **I**). Consequently, the carboxylate anion-catalyst complex decomposes under the action of hydrazine to yield the intermediate **II**, wich is converted to the desired dihydrazide with subsequent regeneration of the active site (Sheme 4):
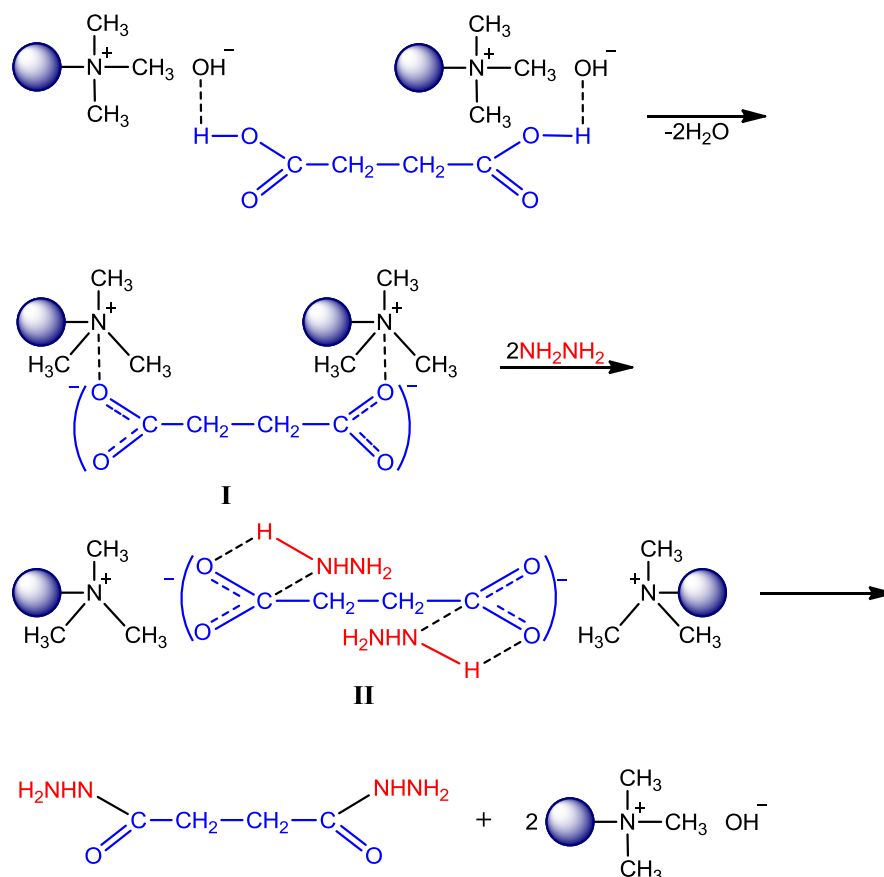
Scheme 4. Proposed mechanism for the synthesis of SADH on the AV-17-8 (OH) as catalyst

Similar IR spectroscopic and kinetic evidences supporting the formation of adsorbtion complexes under the conditions of interfacial catalysis established during alkylation of different benzyl amines, ketones in an aqueous medium, catalyzed by quaternary ammonium salts, and reaction of oleic acid with hydrazine on the polymer catalyst [20, 23, 24].

Reusability of the Catalyst

After the reaction completion, the polymer catalyst AV-17-8 is treated with an aqueous-alcoholic solution, which washes out the dihydrazide adsorbed on the ion exchanger surface, then it is regenerated with a 10 % of NaOH solution. As a result, the ion exchanger operation life considerably increases, and the catalyst preserves the initial activity and selectivity for a long time.

Conclusions

In summary, we have proposed a one-step method for obtaining of succinic acid dihydrazide using a novel heterogeneous, efficient and reusable ion-exchange catalysts. It established that the most efficient catalysts for the selective hydrazinolysis of succinic acid are basic anion exchangers AV-17-8 and AN-31. The conversion of succinic acid was 91–95 %, and yield of SADH was 80–93 %. Conditions were determined for the catalytic synthesis of SADH on anion exchanger AV-17-8 (OH) in aqueous medium, which provided

yields of SADH as high as 93 %. A probable mechanism of the reaction with the participation of fixed ammonium ions and counterions of the anion exchanger was proposed on the basis of results from IR spectroscopic studies. The polymer catalyst AV-17-8 used can be easily recovered and reused without a significant decrease in the yield of the product. The proposed one-step method offers several advantages: high selectivity of the process with respect to the target product, repeated use of a catalyst, no need for anticorrosion equipment and organic solvents, environmental safety compared to known methods for synthesis of dihydrazides, therefore the method can be useful and attractive for preparation of succinyldihydrazide.

Author Information*

———————————————————————————————————

*The authors' names are presented in the following order: First Name, Middle Name and Last Name

Sveta Absadykovna Dzhumadullaeva (*corresponding author*) — Candidate of Chemical Sciences, Professor of the Khoja Akhmet Yassawi International Kazakh-Turkish University, B. Sattarchanov avenue, 29, 160200, Turkestan, Kazakhstan; e-mail: sveta.jumadullayeva@ayu.edu.kz; https://orcid.org/0000-0003-2673-2915

Abduali Baeshovich Baeshov — Doctor of Chemical Sciences, Academician of the National Academy of Sciences of the Republic Kazakhstan, D.V. Sokolsky Institute of Fuel,Catalysis and Electrochemistry, Kunaev street, 142, 050010, Almaty, Kazakhstan; e-mail: bayeshov@mail.ru; https://orcid.org/0000-0003-0745-039X

Author Contributions

The manuscript was written through contributions of all authors. All authors have given approval to the final version of the manuscript. CRediT: **Sveta Absadykovna Dzhumadullaeva** conceptualization, data curation, investigation, methodology, validation, visualization, writing-review & editing; **Abduali Baeshovich Baeshov** conceptualization, formal analysis, visualization, resources, supervision, validation, writing-review & editing.

Conflicts of Interest

The authors declare no conflict of interest.

References

1   Abo-Bakr, A.M. (2013). Synthesis and evaluation of antimicrobial activity of some new heterocyclic compounds using succinic acid dihydrazide as a precursor. *International Journal of Scientific and Engineering Research, 4*(10), 1438–1445.

2   Satyanarayana, A., Kenie, D.N., & Shyamala, P. (2013). Speciation Stady on the Interaction of Some Divalent Transition Metal Ions with Succinic acid Dihydrazide in Aqueous Medium. *Acta Chimica Slovenica, 60*, 807–812.

3   Dhasarathan, S., Shunmugaperumal, S., & Selvaraj, P.K. (2022). Synthesis of Ferrocene Based Schiff Possessing Different Metal Ion Sensing Aptitude and Partaking Antimicrobial Activity. *Journal of the Mexican Chemical Society, 66*(3), 343–361. https://doi.org/10.29356/jmcs.v66i3.1677

4   Bonacorso, H.G., Cechinel, C.A., Pittaluga, E.P., Ferla A. et al. (2010). Succinic Acid Dihydrazide: a Convenient *N,N*-Double Block for the Synthesis of Symmetrical and non- Symmetrical Succinil-bis[5-trifluoro(chloro)methyl-1*H*-pyrazoles]. *Journal of the Brazilian Chemical Society, 21*(9), 1656–1663. https://doi.org/10.1590/S0103-505320100 00900009

5   Topić, E., Damjanović, V., Pičuljan, K., Vrdoljak, V., & Rubčić, M. (2022). Succinyl and Adipoyl Dihydrazones: A Solid-State, Solution and Antibacterial Study. *Crystals, 12,* 1175–1187. https://doi.org/10.3390/cryst12081175

6   Ali, S., Singh, V., Jain, P., & Tripathi, V. (2019). Synthesis, antibacterial and molecular of docking studies of macrocyclic metal complexes of dihydrazide and diketone. *Journal of Saudi Chemical Society, 23,* 52–60. https://doi.org/10.1016/j.jscs.2018.04.005

7   Dolzhenko, A.V., Kolotova, N.V., Koz'minykh, V.O., Syropyatov, B.Ya., Kotegov, V.P., & Godina, A.T. (2002). Sintez i farmakologicheskaia aktivnost zameshchennykh amidov i gidrazidov yantarnoi kisloty [Synthesis and pharmacological activity of substituted amides and hydrazides of succinic acid]. *Khimiko-farmatsevticheskiy zhurnal — Pharmaceutical Chemistry Journal*, *36*, 174–176 [in Russian]. https://doi.org/10.1023/A:1019824419554

8   Freeman, J.A. & Carne, I.C. (1970). Use of succinic acid 2,2-dimethyl hydrazide (ALAR) to reduce winter injury in strawberries. *Canadian Journal of Plant Science, 50,* 189–190. https://doi.org/10.4141/cjps70-069

9   Székács, A. (2021). In: R. Mesnage, J. Zaller (Ed) *Herbicides: Chemistry, Efficacy, Toxicology, and Environmental Impacts*, Elsevier Science, 41–86. https://doi.org/10.1016/B978-0-12-823674-1.00008-0

10 Huang, C.H. & Stone, A.T. (2003). Transformation of the plant Growth regulator daminozide (Alar) and structurally related compounds with Cu II ions: oxidation versus hydrolysis. *Environmental Science and Technology, 37*(9), 1829–1837. https://doi.org/10.1021/es026244w

11 Kenie, D.N., Satyanarayana, A., & Shyamala, P. (2015). Chemical Speciation Stady of Ternary Complexes of Cu (II) with Succinic acid Dihydrazide and Some Amino Acids in Aqueous Solution. *Chemistry and Materials Research, 7*(4), 93–102.

12 Amin, M.A., Shokry, H., & Mabrouk, E.M. (2012). Nickel corrosion inhibition in sulfuric acid — electrochemical studies, morphologies, and theoretical approach. *Corrosion, 68*(8), 699–712. https://doi.org/10.5006/0508

13 Miminoshvili, E.B. (2009). Metal hydrazidocomplexes. *Journal of Structural Chemistry, 50*, 174–181. https://doi.org/10.1134/S0036023609010252

14 Farouk, K., Mohamad, K.Ch., & Wail, A. (2012). Synthesis of Macrocyclic Bis-Hydrazone and their use in Metal Cations Extraction. *International Scholarly Research Network. Organic Chemistry,* 1–8. https://doi.org/10.5402/2012/208284

15 Tomuta, A.M., Ramis, X., Ferrando, F., & Serra, A. (2012). The use of dihydrazides as latent curing agents in diglycidyl ether of bisphenol A coatings. *Progress in Organic Coatings. 74*, 59–66. https://doi.org/10.1016/j.porgcoat.2011.10.004

16 Dzhumadullaeva, S.A. & Bayeshov, A.B. (2021). Liquid Phase Synthesis of 1,2-Dihydropyridazine-3,6-dione in the Presence of Ionite Catalysts. *Russian Journal of Physical Chemistry A, 95*(5), 954–957. https://doi.org/ 10.1134/S0036024421050101

17 GOST 10896-7 Ionity. Podgotovka k ispytaniiu [Ion-exchange resins. Preparation of specimens for test] (1998). Moscow: Izdatelstvo standartov, 7 [in Russian]. https://docs.cntd.ru/document/1200018359

18 GOST 20255.1-89. Ionity. Metod opredeleniia staticheskoi obmennoi yemkosti [Ion-exchange resins. Method of determining static ion-exchange capacity] (2002). Moscow: Izdatelstvo standartov, 6 [in Russian]. https://docs.cntd.ru/document/1200018372

19 Korenman I.M. (1975). *Fotometricheskii analiz. Metody opredeleniia organicheskikh soedinenii* [Photometric Analysis. Methods for the determination of organic compounds]. Moscow: *Khimiia — Chemistry*. Publishing [in Russian].

20 Dzhumadullaeva, S.A. & Baeshov, A.B. (2019). Study of kinetics and mechanism of heterogenous catalytic hydrazinolysis of oleic acid. *Russian Journal of General Chemistry, 89*(2), 190–193. https://doi.org/10.1134/S1070363219020038

21 Dzhumadullaeva, S.A., Bayeshov, A.B., Altynbekova, M.O., & Abzhalov, B.S. (2018). Supramolecular complexes of ionites with organic substrates. *News of National Academy of Sciences of the Republic of Kazakhstan. Series Chemistry and Technology, 2* (428), 26–30. https://doi.org/10.32014/2018.2518-1491

22 Rabo, J.A. (1981). Unifying principles in zeolite chemistry and catalysis. *Catalysis Reviews. Science and Engineering, 23*(1-2), 293–313. https://doi.org/10.1080/03602458108068080

23 Schönbauer, D., Spettel, M., Police, R., Pittenauer, E., & Schnürch, M. (2019). Investigations of the generality of quaternary ammonium salts as alkylating agents in direct C-H alkylation reactions: solid alternatives for gaseous olefins. *Organic and Biomolecular Chemistry, 17*, 4024–4030 https://doi.org/10.1039/C90B00243J

24 Dermeik, S. & Sasson, Y. (1985). Effect of water on the extraction and reactions of fluoride anion by quaternary ammonium phase transfer catalysts. *Journal of Organic Chemistry, 50*(6), 879−882. https://doi.org/10.1021/jo00206a031

Darzhan E. Aitbekova[1]* (iD), Murzabek I. Baikenov[1] (iD), Aigul A. Muratbekova[1] (iD),
Abylaikhan N. Bolatbay[2] (iD), Nazerke Zh. Balpanova[1] (iD), Sairagul Tyanakh[1] (iD),
Fengyun Ma[3] (iD), Tolkyn O. Khamitova[4] (iD)

[1]*Department of Chemical Technology and Petrochemistry, Karaganda Buketov University, Karaganda, Kazakhstan;*
[2]*Department of Physical and Analytical Chemistry, Karaganda Buketov University, Karaganda, Kazakhstan;*
[3]*Xinjiang University, Urumqi, China;*
[4]*Department of Soil Science and Agrochemistry, Saken Seifullin Kazakh Agrotechnical University, Astana, Kazakhstan*
(*Corresponding author's e-mail: darzhan91@mail.ru)

The Use of the Catalysts Based on Coal Ash Microsphere and Chrysotile in the Thermal Destruction of Primary Coal Tar

In order to evaluate the possibility of using different catalysts prepared for the hydrogenation process of primary coal tar, the method of differential thermal analysis was used, which allows to determine the kinetic parameters of thermal destruction, such as the rate constant, activation energy, and pre-exponential multiplier. The effect of catalysts on characteristics of mass loss during heating of "Shubarkol Komir" JSC primary coal tar at a constant speed (20 K/min) in a nitrogen medium has been considered. Microsphere, NiO/microsphere, CoO/microsphere, chrysotile and NiCo/chrysotile have been taken as catalytic additives. In the presence of the catalysts, the rate of thermal destruction of primary coal tar increases in the following order: CoO/microsphere < NiO/microsphere < NiCo/chrysotile. While microsphere catalysts extend the range of thermal destruction, chrysotile catalysts lead to the rapid completion of the destruction process. This fact is characterized by the formation of bonds between catalytic additives and primary coal tar. It is important to determine such parameters that affect on the activation energy and macrokinetics of the thermal decomposition process for prediction of catalyst activity during hydrogenation of heavy hydrocarbon raw materials.

Keywords: primary coal tar, differential thermal analysis, catalyst, hydrogenation, microsphere, chrysotile, nickel, cobalt.

Introduction

The exploration of catalyst-assisted thermal processes for hydrocarbon raw materials has garnered significant attention due to its relevance in industrial applications, including pyrolysis and hydrogenation. Thermogravimetric analysis (TGA), complemented by advanced analytical tools, has become a cornerstone in unraveling the complex interactions between hydrocarbons and catalysts. The thermal decomposition approach proves advantageous for forecasting the efficacy of catalysts in the catalytic processing of dense hydrocarbon feedstock, including high-viscosity oil, residual heavy oil, and coal tars [1].

Ibrahim and co-authors asserted that a key metric for assessing the hydrogenation of dense hydrocarbon feedstock lies in the thermal decomposition of their organic mass within an inert medium, specifically, the peak rate of mass loss [2].

The thermal degradation of dense hydrocarbon feedstock involves the cleavage of donor-acceptor and valence bonds, accompanied by the liberation of moisture. This process results in the generation and segregation of gaseous and volatile liquid compounds, as well as non-volatile liquid and solid substances. Furthermore, it entails the polycondensation of decomposition by-products, leading to the formation of semi-coke and coke, along with the emission of additional gaseous compounds. When subjecting heavy hydrocarbon raw materials to heating in an inert environment, a biphasic mechanism, comprising primary and secondary decomposition stages, becomes evident. Primary decomposition conventionally occurs approximately at 770 K, while secondary decomposition takes place at elevated temperatures [3].

Various techniques employed for investigating the kinetics of thermal degradation of dense hydrocarbon feedstock reveal different faces of this complex process. Literature sources [4–6] indicate the application of non-isothermal kinetics and dynamic thermogravimetry methods for determination of the kinetic parame-

ters of destruction of heavy hydrocarbon raw materials during the processing of the thermogravimetric curve. These methods enable the calculation of activation energy, enthalpy, and entropy of activation.

TGA studies have highlighted the temperature-dependent hydrogenation processes of heavy hydrocarbon raw materials in the presence of catalysts [7–9]. The results of the studies of the hydrogen formation kinetics and mechanisms have showed the catalyst efficiency. As reported in the literature [10], thermogravimetric analysis, concurrently linked to a Fourier transform infrared spectrometer (FTIR) and a gas chromatography (GC), during coal pyrolysis with a nickel catalyst exhibited an augmentation in hydrogen formation within the temperature range of 400–500 °C. Given that this temperature corresponds to the hydrogenation processes of heavy hydrocarbon raw materials, the observed increase in mass loss serves as a predictive indicator for the hydrogenation activity of the catalyst.

The purpose of this study is to evaluate the catalytic activity of NiO/microsphere, CoO/microsphere, and NiCo/chrysotile catalysts by applying differential thermal analysis to primary coal tar (PCT).

Experimental

Technical description of primary coal tar. The coal tar derived from Shubarkol deposit (Karaganda region, Kazakhstan) is classified as a primary tar, indicating that it has not undergone secondary thermal treatments. In contrast to high-temperature coking resin, this tar includes a higher proportion of oxygen-containing compounds, in particular, phenols and unsaturated compounds. The technical details of the coal tar are provided in the paper, referencing the information from the technical description [11].

Procedure for the nanocatalysts preparation. To ensure the formation of an active center with a consistent chemical composition in the catalyst, an important requirement involves depositing active compounds from the solution onto the surface of hard-to-dissolve oxides and ensuring their uniform distribution. The use of catalysts on carriers with a homogeneous distribution of active phase throughout the sorbent volume contributes to a reduction in the consumption of the active component and increases the catalyst's activity [12, 13].

Microspheres [14–16] and chrysotile [17, 18] were chosen as catalysts carriers due to their developed surface area, high thermal stability, and low cost. Microspheres have been obtained from the coal ash originating from Karaganda CHP-3 (Republic of Kazakhstan) by flotation method. The chrysotile mineral used as a substrate for the active centers of nickel and cobalt is sourced as a byproduct from asbestos production at Kostanay Minerals JSC in the Republic of Kazakhstan. This chrysotile mineral is classified as a serpentine raw material with the chemical composition $3MgO \cdot 2SiO_2 \cdot H_2O$.

NiO/microsphere and CoO/microsphere catalysts have been prepared using the "wet mixing" method. 20% aqueous solutions of nickel (II) nitrate $Ni(NO_3)_2 \cdot 6H_2O$ and cobalt (II) nitrate $Co(NO_3)_2 \cdot 6H_2O$ crystallohydrates (analytically pure, Kupavnareaktiv, Russian Federation) were separately taken. The microspheres were added so that the amount of nickel and cobalt in the resulting solution was 5 % of the total mass of catalyst obtained after completion of the process. The mixture underwent thorough stirring while being heated. Following the formation of a dense mass, it was dried in a drying oven at a temperature of 105 ºC. Subsequently, the obtained samples subjected to heat treatment in a muffle furnace at a temperature of 500 ºC for 2 hours.

According to the studies [19–22] Ni-Co bimetallic catalysts' activity and stability to coke deposition are superior to the properties of Ni and Co metals taken separately. This is due to the synergy effect between Ni and Co.

In order to remove magnesium and calcium salts contained in the original chrysotile, pre-rinsing was carried out with a 20 % solution of hydrochloric acid. The preparation of the binary catalyst has been realized by dissolving nickel (II) nitrate crystal hydrate (20 %) in water while heating, and then adding alkalized chrysotile to the resulting solution. The resulting mixture was heated and thoroughly stirred until a thick mass was formed. The mass was further dried in a drying oven at a temperature of 105 °C to a constant mass. Then the crystallohydrate of cobalt (II) nitrate was dissolved in water (20 %), and the process was repeated with the dry mass of chrysotile obtained with nickel salt. Further, chrysotile with nickel and cobalt salts was thermally treated in a muffle furnace at a temperature of 500 °C for 2 hours. The mass fraction of nickel and cobalt to the total mass of the resulting catalytic mixture was 5 %.

Differential thermal analysis of PCT. Thermogravimetric studies to determine the effect of catalysts on the kinetic parameters of thermal degradation of primary coal tar LABSYS™ EVO TG, DTA, DSC 1600 °C with thermogravimetric scales connected to DTA and DSC converters, metal-resistive furnace and multitasking software structure controlling various modules (Setaram, France) was carried out in the number

of equipments. In order to avoid the diffusion effect and to ensure process homogeneity during sample preparation, 3 g of Al_2O_3 was placed in a crucible and fired in a muffle furnace at a temperature of 600 °C for 2 hours. Then it was placed in a desiccator for drying. During the study of thermal destruction of primary hard coal tar, 1 % catalyst and dried Al_2O_3 have been added to its 0.2 g mass. Microsphere, NiO/microsphere, CoO/microsphere, chrysotile and NiCo/chrysotile have been taken as the catalytic additives. As per the literature source [23], the optimum quantity of nanocatalyst introduced to the mass of raw materials for the catalytic processing of dense hydrocarbon feedstock during thermal degradation is reported to be 1 %

Two identical Al_2O_3 crucibles with a volume of 100 ml were used for thermal analysis. Their design provides direct measurement of temperature in the substance mass. Samples of the mixture with and without a catalyst were prepared by analytical grinding (~17 mg; measurement accuracy ±0.01 %). Then they were loaded into one of the corundum crucibles with a volume of 2 ml, the another one was left empty. Both crucibles were placed into the electric furnace of the device and heated linearly from 33 °C to 600 °C at a constant heating rate of 20 °C/min, while the mass change was recorded. At a certain temperature various reactions begin and at this temperature the mass loss of the sample is observed. Thus, the rate of mass loss increases and decreases again after the reaction is completed. Thermal analysis is performed in an oxygen-free environment to avoid oxidation reactions. Nitrogen was taken as a gas medium, the flow rate was 30 ml/min. Processes are carried out in comparative conditions, because the size and granulometric composition of the sample affect the results of the analysis. The type of derivativograms also depends on the gas emission conditions. If the rate of formation of gaseous substances is higher than the rate of their removal, then gaseous products that affect the process of thermal destruction are accumulated inside the sample. In order to prevent accumulation of gases in the derivatograph, their suction is provided.

Results and Discussion

Technical characteristics of coal tar are given in Table 1.

Table 1

Technical characteristics of primary coal tar [11]

Description	Value
Tar density at 20 °C, g/cm^3	1.061
Anhydrous tar density at 20 °C, g/cm^3	1.062
Water content, %	2.2
Mass fraction of the substances insoluble in toluene, %	1.4
Mass fraction of the substances insoluble in quinoline, %	–
Ash content, %	0.12
Phenol content, %	20.6
Naphthalene content, %	1.6
Mass fraction of fractional composition, %	
till 180 °C	5.1
180–210 °C	4.4
210–230 °C	4.8
230–270 °C	15.8
270–390 °C	19.7

The studied coal tar is characterized by a low density, a small amount of water, the absence of crystallizing fractions, a low yield of substances insoluble in toluene, a high content of phenols, a small proportion of naphthalene.

The information about particle's size and distribution, chemical composition and surface morphology of the microsphere, NiO/microsphere, CoO/microsphere catalysts used in thermal degradation of primary coal tar is given in [24], NiCo/chrysotile catalyst's particle's size and distribution, X-ray phase analysis, surface morphology information is given in [25]. The scanning electron microscope (SEM) image of the microspheres (Fig. 1) and the transmission electron microscope (TEM) image of the chrysotile (Fig. 2) are illustrated in the pictures below.
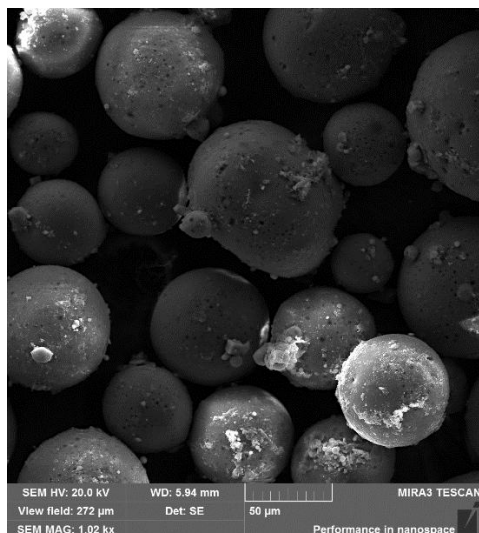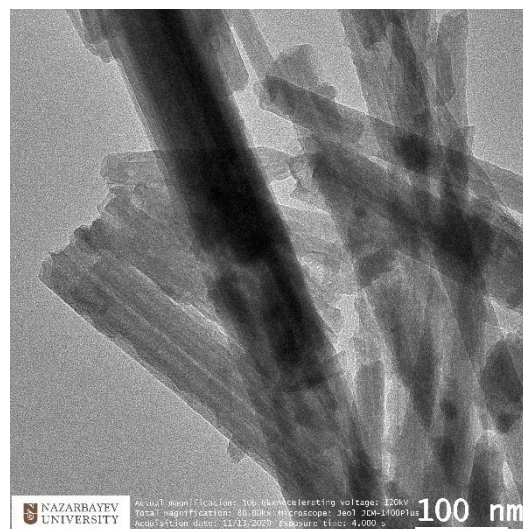
Figure 1. SEM image of the microspheres

Figure 2. TEM image of the chrysotile

The surface of the microspheres exhibited micropores with sizes ranging from 200 to 400 nm, along with irregularities [24]. The micrographs (Fig. 2) reveal a tightly packed arrangement of chrysotile tubes. However, on a larger scale, the long-range order of chrysotile can be characterized as "amorphously" packed. The mineral contains nanotubes with an inner diameter of approximately 10 nm and an outer diameter of about 60 nm [25].

The method of determining the kinetic parameters of thermal destruction of carbon-containing substances describing the entire part of the one-stage thermogravimetry curve was explained by T.V. Bukharkina [26] and S.Yu. Lyrschikov [27].

The "gross-stage" method of thermogravimetric analysis, as well as Professor Gulmaliev's [28] kinetic parameters (rate constant k, pre-exponential multiplier) for the thermal degradation (heating rate 20 K/min) of heavy hydrocarbon raw material, specifically high-viscosity oil, and its blend with catalysts (including microsphere and NiO/microsphere catalyst) and polymers, has been detailed in the referenced paper [1]. The calculated activation energy (E_a) and pre-exponential multiplier (k_0) were determined according to the method presented in [28].

Notably, elevated values of activation energy and pre-exponential multiplier are observed during the decomposition of high-viscosity oil within the temperature range of 534–759 K, particularly when microspheres and polyethylene glycol are introduced. On the contrary, lower activation energy is noted during the decomposition of a mixture comprising high-viscosity oil, polyethylene glycol, and NiO/microsphere in the temperature range of 520–745 K.

Figure 3 shows thermogravimetric curves of primary decomposition of primary coal tar and its mixture with catalysts.
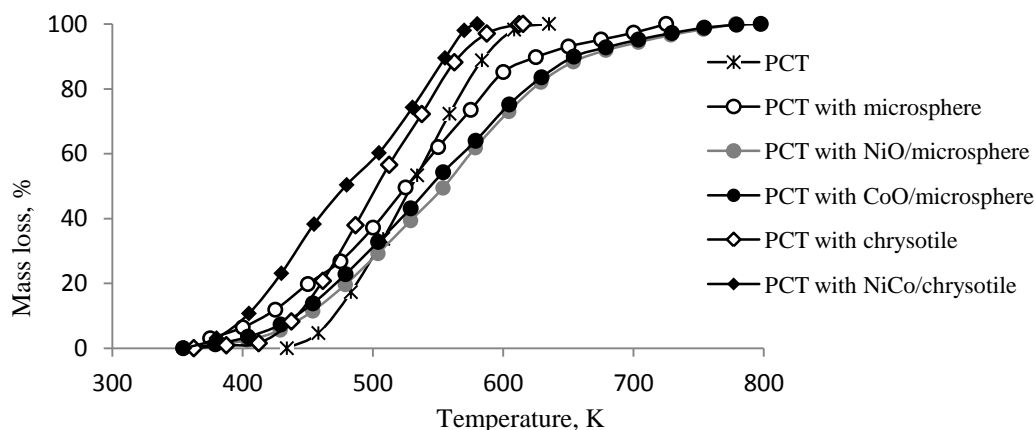

Figure 3. Thermogravimetric curves of destruction of primary coal tar and its mixture with catalysts

As can be seen in Figure 3, during the thermal destruction of unmixed primary coal tar, mass loss begins at 434 K, and when CoO/microsphere and NiO/microsphere are added, mass loss starts at 354 K, when microsphere is added, at 350 K, in case of chrysotile is added — at 407. The onset temperature of mass loss when adding NiCo/chrysotile is 355 K. In the main stage of destruction of primary coal tar, the mass loss process ends quickly in the mixture of NiCo/chrysotile at 577 K, in the mixture of PCT with chrysotile at 623 K, in the destruction of unmixed primary coal tar at 635 K, in the presence of microspheres at 748 K, in the presence of NiO/microsphere at 778 K , in the presence of CoO/microsphere at 798 K.

Figure 4 shows the temperature dependence of the rate of mass loss on temperature during thermal destruction of primary coal tar and its mixture with catalysts.
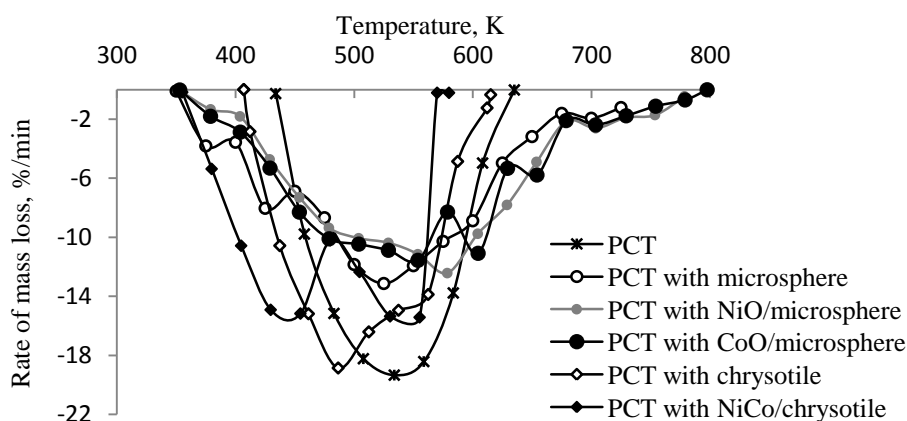

Figure 4. DTG curves of destruction of primary coal tar and its mixture with catalysts

The analysis of the derivative thermogravimetry curves for heavy hydrocarbon raw materials in Figure 4 reveals a staged and variable-speed progression of processes. The introduction of NiCo/chrysotile catalyst and microsphere-based catalysts induces an early onset of thermal decomposition in primary coal tar at approximately 80 K. The inclusion of chrysotile does not alter the maximum rate of thermal decomposition (19 %/min). Notably, the mass loss rates during the thermal decomposition of PCT with the incorporation of microsphere-based catalysts and NiCo/chrysotile are diminished. The maximum rate of mass loss is observed at temperatures of 534 K for unalloyed PCT, 525 K with the addition of microspheres, 579 K with the addition of NiO/microspheres, 554 K with the addition of CoO/microspheres, 487 K with the addition of chrysotile, 455 K, and 555 K with the addition of NiCo/chrysotile.

Microsphere catalysts (CoO/microsphere and NiO/microsphere) affect the duration of the main stage of the thermal decomposition process of primary coal tar. This situation leads to a more decomposition of the resin mass in the main stage. And in PCT and NiCo/chrysotile mixture, thermal destruction takes place in a short time, but at a high speed.

The thermokinetic parameters, namely the pre-exponential factor (k_0) and activation energy (E_a), for primary coal tar and its blend with catalysts, have been determined using the "gross-stage" method [26], and the results are presented in Table 2.

T a b l e 2

**Kinetic parameters of thermal destruction of PCT and its mixture
with catalysts according to the "gross-stage" method**

Composition	Temperature range, K	k_0, min^{-1}	E_a, kJ/mol
Primary coal tar	434–635	$2.2 \cdot 10^3$	38.4
Mixture of PCT and microspheres	350–748	$1.1 \cdot 10^2$	28.3
Mixture of PCT and NiO/microsphere	354–778	$6.6 \cdot 10$	26.7
Mixture of PCT and CoO/microsphere	354–798	$2.3 \cdot 10$	22.0
Mixture of PCT and chrysotile	407–623	$6.1 \cdot 10^4$	50.0
Mixture of PCT and NiCo/chrysotile	355–577	$2.3 \cdot 10^2$	26.6

According to the Table 2, the activation energy and pre-exponential multiplier of the thermal decomposition of unmixed coal tar is higher than when microsphere catalysts and NiCo/chrysotile are added, that is, these catalysts facilitate the initiation of thermal destruction of PCT. And when chrysotile is added, the activation energy of thermal destruction increases, and the process is slowed down.

The kinetic parameters of the thermal decomposition of primary coal tar and its combinations with catalysts, including the rate constant (k), pre-exponential factor (k_0), and activation energy (E_a), were determined using the method of thermogravimetric analysis as outlined in Professor Gulmaliev's work [28]. The calculated values are presented in Table 3.

T a b l e   3

Kinetic parameters of thermal destruction of PCT and its mixture with catalysts according to the "inflection point" method

Composition	Temperature range, K	k, min^{-1}	k_0, min^{-1}	E_a, kJ/mol
Primary coal tar	434–635	$2.3 \cdot 10^{-1}$	$1.18 \cdot 10^2$	27.9
Mixture of PCT and microspheres	350–748	$9.5 \cdot 10^{-2}$	1.06	10.3
Mixture of PCT and NiO/microsphere	354–778	$1.2 \cdot 10^{-1}$	2.52	13.6
Mixture of PCT and CoO/microsphere	354–798	$9.8 \cdot 10^{-2}$	1.13	10.0
Mixture of PCT and chrysotile	407–623	$3.3 \cdot 10^{-1}$	$4.5 \cdot 10^3$	45.7
Mixture of PCT and NiCo/chrysotile	355–577	$1.5 \cdot 10^{-1}$	6.43	15.6

When comparing the thermokinetic parameters determined through the "gross-stage" method and the "inflection point" method for the thermal degradation of pure primary coal tar and its decomposition with a blend of microsphere catalysts, the disparities observed between the methods are consistent. For instance, the activation energies of the thermal decomposition for the mixture of PCT and microsphere, as well as PCT and CoO/microsphere, determined by both methods, exhibit similar values. In both cases, where NiCo/chrysotile is introduced to PCT, the activation energy values closely align with the corresponding thermokinetic parameters of the PCT and NiO/microsphere mixture. Hence, both methods can be equally applyed for comparing the kinetic parameters of the thermal degradation of primary coal tar.

The values of the rate constants of the thermal decomposition of primary coal tar, determined by the "inflection point" method are close to each other and relatively low when adding CoO/microsphere and microsphere. The highest rate constant is observed in the mixture of PCT and chrysotile ($3.3 \cdot 10^{-1}$ min^{-1}). Values of rate constants when NiCo/chrysotile and NiO/microspheres are added to PCTs are close to each other.

The thermal decomposition of primary coal tar of JSC "Shubarkol coal" in the presence of hydrogen donors and catalysts (magnetic part of microspheres and nickel-enriched chrysotile) in the "gross stage" method [3], magnetic microsphere leads to a decrease in activation energy and pre-exponential multiplier compared to chrysotile-based catalyst. And in the "inflection point" method, the addition of two catalysts to the PCT leads to 2–2.5 times increase in the activation energy and rate constants compared to the corresponding parameters of the thermal destruction of the resin without the initial additive.

Conclusions

Comparing the results obtained by two different methods, it can be seen that the microsphere-based catalysts and nickel-cobalt-enriched chrysotile-based binary catalyst decrease the activation energy and rate constant of primary coal tar thermodestruction, and the addition of chrysotile mineral to the system increases both the activation energy and the rate constant of this process.

It shows that the effect of catalytic additives on the thermal destruction of coal tar is directly related to the nature of carriers. While microsphere catalysts extend the range of thermal destruction, chrysotile and the catalyst based on it lead to the rapid completion of the destruction process. This fact as observed in previous works [4, 5] is characterized by the formation of bonds between catalytic additives and heavy hydrocarbon raw materials.

In the presence of the studied catalysts, the rate of thermal destruction of primary coal tar increases in the following order: CoO/microsphere < NiO/microsphere < NiCo/chrysotile.

Author Information*

_____

*The authors' names are presented in the following order: First Name, Middle Name and Last Name

Darzhan Ergalievna Aitbekova (*corresponding author*) — PhD, Associate Professor, Department of Chemical Technology and Petrochemistry, Karaganda Buketov University, Universitetskaya street, 28, 100024, Karaganda, Kazakhstan; e-mail: darzhan91@mail.ru; https://orcid.org/0000-0002-6839-9711

Murzabek Ispolovich Baikenov — Doctor of Chemical Sciences, Research Professor, Department of Chemical Technology and Petrochemistry, Karaganda Buketov University, Universitetskaya street, 28, 100024, Karaganda, Kazakhstan; e-mail: murzabek_b@mail.ru; https://orcid.org/0000-0002-8703-0397

Aigul Akizhanovna Muratbekova — Candidate of Chemical Sciences, Associate Professor, Department of Chemical Technology and Petrochemistry, Karaganda Buketov University, Universitetskaya street, 28, 100024, Karaganda, Kazakhstan; e-mail: aigulmuratbekova@mail.ru; https://orcid.org/0000-0002-2156-9306

Abylaikhan Nurlanuly Bolatbay — Master of Technical Sciences, Lecturer, Department of Physical and Analytical Chemistry, Karaganda Buketov University, Universitetskaya street, 28, 100024, Karaganda, Kazakhstan; e-mail: abylai_bolatbai@mail.ru; https://orcid.org/0000-0001-5047-3066

Nazerke Zhumagalievna Balpanova — PhD, Postdoctoral Researcher, Department of Chemical Technology and Petrochemistry, Karaganda Buketov University, Universitetskaya street, 28, 100024, Karaganda, Kazakhstan; e-mail: nazerke_90@mail.ru; https://orcid.org/0000-0003-3089-1871

Sairagul Tyanakh — Master of Technical Sciences, Lecturer, Department of Chemical Technology and Petrochemistry, Karaganda Buketov University, Universitetskaya street, 28, 100024, Karaganda, Kazakhstan; e-mail: saika_8989@mail.ru; https://orcid.org/0000-0001-5343-4695

Fengyun Ma — PhD, Professor, Xinjiang University, Urumqi, China; e-mail: ma_fy@126.com; https://orcid.org/0000-0002-6902-0769

Tolkyn Ondirisovna Khamitova — PhD, Associate Professor, Department of Soil Science and Agrochemistry, Saken Seifullin Kazakh Agrotechnical University, Astana, Zhenis street, 62, 010000, Kazakhstan; e-mail: khamitova.t@inbox.ru; https://orcid.org/0000-0002-4691-3732

Author Contributions

The manuscript was written through contributions of all authors. All authors have given approval to the final version of the manuscript. CRediT: **Darzhan Ergalievna Aitbekova** conceptualization, formal analysis, investigation, visualization, writing-original draft, writing-review & editing; **Murzabek Ispolovich Baikenov** conceptualization, resources, supervision; **Aigul Akizhanovna Muratbekova** writing-original draft, formal analysis; **Abylaikhan Nurlanuly Bolatbay** investigation, formal analysis, validation; **Nazerke Zhumagalievna Balpanova** investigation; **Sairagul Tyanakh** investigation; **Fengyun Ma** conceptualization; **Tolkyn Ondirisovna Khamitova** investigation.

Acknowledgments

Conflicts of Interest

The authors declare no conflict of interest.

References

1 Yedrissov, A.T., Aitbekova, D.E., Tusipkhan, A., Tateyeva, A.B., Baikenova, G.G., Baikenov, M.I., & Kaikenov, D.A. (2021). TGA-Based Thermokinetics of High-Viscosity Oil Decomposition in the Presence of Nanocatalysts, Catalytic Additives, and Polymers [Article]. *Petroleum Chemistry*, *61*(4), 431–437. https://doi.org/10.1134/s0965544121050157

2 Ibrahim, M.M., Seehra, M.S., & Keogh, R.A. (1990). Comparison of the Liquefaction Yields of Coals with their Composition, Free-Radical Density and Thermal Parameters. *Fuel Processing Technology, 25*(3), 215–226. https://doi.org/10.1016/0378-3820(90)90028-q

3 Balpanova, N.Z., Baikenov, M.I., Gyulmaliev, A.M., Absat, Z.B., Batkhan, Z., Ma, F., ... Tusipkhan, A. (2021). Thermokinetic parameters of the primary coal tars destruction in the presence of catalysts and polymeric materials. *Bulletin of the University of Karaganda-Chemistry*, (102), 86–95. https://doi.org/10.31489/2021Ch2/86-95

4 Strizhakov, D.A., Yusevich, A.I., Yurachka, V.V., Kadiev, K.M., Agabekov, V.E., & Khadzhiev, S.N. (2016). Kinetics of thermolysis of vacuum tower bottoms mixed with pine sawdust. *Petroleum Chemistry*, *56*(8), 703–710. https://doi.org/10.1134/s0965544116080168

5 Berdinazarov, Q.N., Khakberdiev, E.O., Normurodov, N.F., & Ashurov, N.R. (2022). Mechanical and thermal degradation properties of Isotactic Polypropylene Composites with Cloisite15A and Cloisite20A. *Bulletin of the Karaganda University. "Physics" Series, 107*(3), 52–60. https://doi.org/10.31489/2022ph3/52-60

6 Zhang, P., Chen, Z.Y., Zhang, Q.L., Zhang, S., Ning, X.G., & Zhou, J. (2022). Co-pyrolysis characteristics and kinetics of low metamorphic coal and pine sawdust. *Rsc Advances*, *12*(34), 21725–21735. https://doi.org/10.1039/d2ra02461f

7 Hosseini, M.S. & Chartrand, P. (2021). Critical assessment of thermodynamic properties of important polycyclic aromatic hydrocarbon compounds (PAHs) in coal tar pitch at typical temperature ranges of the carbonization process. *Calphad-Computer Coupling of Phase Diagrams and Thermochemistry*, *74*, Article 102278. https://doi.org/10.1016/j.calphad.2021.102278

8 Yang, Q.L., Yao, Q.X., Ma, D., Liu, Y.Q., He, L., Zhou, R.S., ... Ma, X.X. (2022). Investigation of the (catalytic) co-pyrolysis of Shendong coal and coal tar based on rapid pyrolysis and ANN modelling. *Journal of Analytical and Applied Pyrolysis*, *163*, Article 105486. https://doi.org/10.1016/j.jaap.2022.105486

9 Chen, Z.H., Wang, D.L., Yang, H., Zhang, Y.S., Li, Y.J., Li, C.M., ... Gao, S.Q. (2021). Novel application of red mud as disposal catalyst for pyrolysis and gasification of coal. *Carbon Resources Conversion*, *4*, 10–18. https://doi.org/10.1016/j.crcon.2021.01.001

10 Scaccia, S. (2023). Analysis and distribution of volatile gases from catalytic pyrolysis of Sulcis low-rank coal. *Journal of Analytical and Applied Pyrolysis*, *169*, Article 105820. https://doi.org/10.1016/j.jaap.2022.105820

11 Aitbekova, D.E., Makenov, D.K., Andreikov, E.I., Tsaur, A.G., Ma, F.Y., Baikenova, G.G., ... Baikenov, M.I. (2021). Hydrogen distribution in primary coke oven tar and its fractions. *Bulletin of the University of Karaganda-Chemistry*, (101), 82–90. https://doi.org/10.31489/2021Ch1/82-90

12 Dong, Y.N., Bai, H.Y., Li, S.S., Tang, J., & Niu, W. (2021). Preparation and characterization NiO/HY catalyst. *Materials Express*, *11*(6), 966–973. https://doi.org/10.1166/mex.2021.1987

13 Meiramov, M.G. (2017). Angular-Linear Isomerization on the Hydrogenation of Phenanthrene in the Presence of Iron-Containing Catalysts. *Solid Fuel Chemistry*, *51*(2), 107–110. https://doi.org/10.3103/s0361521917020070

14 Danish, A. & Mosaberpanah, M.A. (2020). Formation mechanism and applications of cenospheres: a review. *Journal of Materials Science*, *55*(11), 4539–4557. https://doi.org/10.1007/s10853-019-04341-7

15 Yang, J.L., Zhao, L., Zhou, T.R., Ma, S.H., & Wang, X.H. (2023). Catalytic Oxidation Activity of NO over Mullite-Supported Amorphous Manganese Oxide Catalyst. *Materials*, *16*(10), Article 3821. https://doi.org/10.3390/ma16103821

16 Kunecki, P., Panek, R., Koteja, A., & Franus, W. (2018). Influence of the reaction time on the crystal structure of Na-P1 zeolite obtained from coal fly ash microspheres. *Microporous and Mesoporous Materials*, *266*, 102–108. https://doi.org/10.1016/j.micromeso.2018.02.043

17 Dai, Y., Peng, Q., Liu, K., Tang, X.K., Zhou, M.Y., Jiang, K., & Zhu, B.N. (2021). Activation of Peroxymonosulfate by Chrysotile to Degrade Dyes in Water: Performance Enhancement and Activation Mechanism. *Minerals*, *11*(4), Article 400. https://doi.org/10.3390/min11040400

18 Peng, Q., Dai, Y., Liu, K., Tang, X.K., Zhou, M.Y., Zhang, Y.J., & Xing, J.J. (2022). Outstanding catalytic performance of metal-free peroxymonosulfate activator: Important role of chrysotile. *Separation and Purification Technology*, *287*, Article 120526. https://doi.org/10.1016/j.seppur.2022.120526

19 Saelee, T., Lerdpongsiripaisarn, M., Rittiruam, M., Somdee, S., Liu, A., Praserthdam, S., & Praserthdam, P. (2021). Experimental and computational investigation on underlying factors promoting high coke resistance in NiCo bimetallic catalysts during dry reforming of methane. *Scientific Reports*, *11*(1), Article 519. https://doi.org/10.1038/s41598-020-80287-0

20 Wu, J., Yan, X.Y., Wang, W.R., Jin, M., Xie, Y.H., & Wang, C.B. (2021). Highly Dispersed CoNi Alloy Embedded in N-doped Graphitic Carbon for Catalytic Transfer Hydrogenation of Biomass-derived Furfural. *Chemistry-an Asian Journal*, *16*(20), 3194–3201. https://doi.org/10.1002/asia.202100727

21 Zhang, J.G., Wang, H., & Dalai, A.K. (2007). Development of stable bimetallic catalysts for carbon dioxide reforming of methane. *Journal of Catalysis*, *249*(2), 300–310. https://doi.org/10.1016/j.jcat.2007.05.004

22 Turap, Y., Wang, I., Fu, T.T., Wu, Y.M., Wang, Y.D., & Wang, W. (2020). Co-Ni alloy supported on CeO2 as a bimetallic catalyst for dry reforming of methane. *International Journal of Hydrogen Energy*, *45*(11), 6538–6548. https://doi.org/10.1016/j.ijhydene.2019.12.223

23 Maloletnev, A.S., Krichko, A.A., & Garkusha, A.A. (1992). Poluchenie sinteticheskogo zhidkogo topliva gidrogenizatsiei uglia [Obtaining synthetic liquid fuel by hydrogenation of coal]. Moscow: Nedra [in Russian].

24 Aitbekova, D., Bakytkyzy, A., Baikenova, G., & Baikenov, M. (2020). The use of catalytic additives for hydrogenation of polyaromatic hydrocarbons. *Materials Today-Proceedings*, *31*, 611–614. https://doi.org/10.1016/j.matpr.2020.07.671

25 Baikenov, M.I., Aitbekova, D.E., Balpanova, N.Z., Tusipkhan, A., Baikenova, G.G., Aubakirov, Y.A., ... Makenov, D.K. (2021). Hydrogenation of polyaromatic compounds over NiCo/chrysotile catalyst. *Bulletin of the University of Karaganda-Chemistry*, (103), 74–82. https://doi.org/10.31489/2021Ch3/74-82

26 Bukvareva, O.F. & Bukharkina, T.V. (2001). Kinetika i termokhimiia protsessov termodestruktsii uglerodsoderzhashchikh veshchestv [Kinetics and thermochemistry of thermal degradation of carbonaceous substances]. Moscow: Mendeleev University of Chemical Technology of Russia [in Russian].

27 Lyrshchikov, S.Y., Strizhak, P.A., & Shevyrev, S.A. (2016). Thermal decomposition of coal and coal-enrichment wastes. *Coke and chemistry*, *59*, 264–270.

28 Gulmaliev, A.M., Golovin, G.S., & Gladun, T.G. (2003). Teoreticheskie osnovy khimii uglia [Theoretical foundations of coal chemistry]. Moscow: Moscow State Mining University [in Russian].

RETRACTION NOTE

Retraction Note to: Green Synthesis, Characterization and Environmental Application of Copper Oxide Nanoparticle obtained Using Aqueous Extract of *Schrebera Swietenioides Roxb.*

Lakshmi S. Tulasi[*1] , P. Sumalatha[2] , N. Usha Rani[1], Pavani Peddi[1]

[1]PVP Siddhartha Institute of Technology, Kanuru, Vijayawada, Andhra Pradesh, India;
[2]Seshadri Rao Gudlavalleru Engineering college, Gudlavalleru, Andhra Pradesh, India
(*Corresponding author's e-mail: tulasi13111986@gmail.com)

The Editor-in-Chief of *Eurasian Journal of Chemistry* has decided to retract this article [1] because it has previously been published by Tulasi *et al.* (2022) [2]. Investigation by the Editorial Board revealed the article [1] contains the same research material as in the previously published article [2] without a proper citation. The Editorial Board considers this article to be redundant.

Corresponding author Lakshmi S. Tulashi partially confirmed the presence of the same material in both articles and was unable to provide a strong argument against retraction.

References

1   Tulasi, S.L., Sumalatha, P., Rani, N.U., & Peddi, P. (2023) Green Synthesis, Characterization and Environmental Application of Copper Oxide Nanoparticle obtained Using Aqueous Extract of Schrebera Swietenioides Roxb. *Eurasian Journal of Chemistry*, *109*(1), 78–89. https://doi.org/10.31489/2959-0663/1-23-2

2   Tulasi, S.L., Swamy, AVVS, Peddi, P., & Rani, N.U. (2022). Green adeptness in the synthesis and stabilization of copper nanoparticles using aqueous root extract of Schrebera swietenioides Roxb, and its catalytic application. *Journal of Medical Pharmaceutical and Allied Sciences*, *11*(1), 4233–4240. https://doi.org/10.55522/jmpas.v11i1.2416

Author Information*

_____

*The authors' names are presented in the following order: First Name, Middle Name and Last Name

Lakshmi S. Tulasi (*corresponding author*) — Assistant Professor, Department of Freshman Engineering, PVP Siddhartha Institute of Technology, Kanuru-52007, Vijayawada, Andhra Pradesh, India; e-mail: tulasi13111986@gmail.com; https://orcid.org/0000-0001-6130-7215

P. Sumalatha — Assistant Professor, BS&H Department, Seshadri Rao Gudlavalleru Engineering college, Gudlavalleru. Andhra Pradesh, India; e-mail: sumasobhan@gmail.com; https://orcid.org/0000-0001-7230-4976

Nannapaneni Usha Rani — Assistant Professor, Department of Freshman Engineering, PVP Siddhartha Institute of Technology, Kanuru, 52007 Vijayawada, Andhra Pradesh, India; e-mail: nannapaneniusharani73@gmail.com

Pavani Peddi — Assistant Professor, Department of Freshman Engineering, PVP Siddhartha Institute of Technology, Kanuru-520007 Vijayawada, Andhra Pradesh, India; e-mail: pavanipeddi7@gmail.com; https://orcid.org/0000-0003-0712-8907